Title

Theoretical and Experimental Investigation of Interstitial Ultrasound for Ablation of Tumors in and Near the Vertebrae and Other Bones

Author

Scott, Serena J.

Publication Date

2014

Peer reviewed|Thesis/dissertation

Theoretical and Experimental Investigation of Interstitial Ultrasound for Ablation of Tumors in and Near the Vertebrae and Other Bones

by

Serena J Scott

DISSERTATION

Submitted in partial satisfaction of the requirements for the degree of

DOCTOR OF PHILOSOPHY

in

Bioengineering

in the

GRADUATE DIVISION

of the

UNIVERSITY OF CALIFORNIA, SAN FRANCISCO

AND

UNIVERSITY OF CALIFORNIA, BERKELEY

[redacted]

To my family,

who raised me up to where I am

Acknowledgements

There are many people who I need to thank for the time, effort, and support they've provided, especially the Thermal Therapy Research Group, my family, and God. Firstly, I would like to thank my graduate research advisor Chris Diederich, who has been an excellent advisor and a great person to work for these past several years. I am so grateful to have had him as a mentor. I also extend my gratitude to the whole Thermal Therapy Research Group: Punit Prakash, Vasant Salgaonkar, Peter Jones, Jeff Wootton, Matt Adams, and Richard Cam; I've felt blessed to have such great coworkers throughout the time I've been here. I thank all of my family and friends, especially my parents, for the advice, love, guidance, and support they've given me my whole life. I thank the rest of my dissertation committee, Tracy McKnight and I-Chow Joe Hsu, and my professors for their guidance and for the knowledge they've imparted. I also thank Misung Han, Viola Reike, the rest of the MR thermometry groups at UCSF, Clif Burdette and Acoustic MedSystems, Emily Perttu, Frank Szoka, and the rest of the Szoka group. I am grateful for the NIH grant R44CA134169 and the Chancellor's Fellowship that supported this work.

Abstract

Theoretical and Experimental Investigation of Interstitial Ultrasound for Ablation of Tumors in and Near the Vertebrae and Other Bones

by

Serena J Scott

Doctor of Philosophy in Bioengineering

University of California, San Francisco and University of California, Berkeley

Chris Diederich, Ph.D., Dissertation Research Director and Chair

The goals of this work are to investigate the feasibility of interstitial ultrasound ablation of tumors in and near the spine and to develop treatment guidelines. Interstitial ultrasound ablation, which allows for directional control of heat deposition, could potentially take advantage of the preferential acoustic absorption and heating that occurs along sonicated bone surfaces in order to ablate targets adjacent to vertebrae without damaging nearby critical anatomy such as the spinal cord.

A platform for modeling patient-specific temperature and thermal dose distributions during catheter-cooled interstitial ultrasound ablation involving bone was developed in Comsol. The 3D, transient, finite element models developed herein considered various approximations of the complex interactions between ultrasound and bone. Experiments in phantoms, *ex vivo* tissues, and *in vivo* tissues were used to validate the numerical models and to characterize the impact of bone on ablation performance. Temperature distributions were measured using both invasive thermometry and MR-based techniques. Comprehensive parametric and patient-

specific simulation studies were performed to investigate the feasibility of interstitial ultrasound ablation of paraspinal tumors and osteolytic vertebral tumors and to develop treatment guidelines.

High ultrasound absorption at bone/soft tissue interfaces increased the volumes of target tissue that could be ablated and/or reduced the necessary treatment times. Models using simplified approximations produced temperature and thermal dose profiles closely matching both experimental measurements and more comprehensive models. Patient-specific and parametric simulations indicated that tumors up to 44 mm in diameter and insulated from the spinal canal by at least 4-5 mm of bone could be completely ablated within 15 min. Critical anatomy closer to the tumor could be preserved by reducing the acoustic energy aimed towards these structures and/or through gaseous insulation. Preferential bone heating and the insulating quality of bone resulted in thermal lesions closely conforming to the shapes of osteolytic targets and fast treatment times.

This work demonstrates that interstitial ultrasound ablation appears feasible for treatment of paraspinal and vertebral tumors. Models and experiments indicate that preferential bone heating may provide improved localization, faster treatment times, and larger treatment zones in unossified tumors bordering bone as compared to other heating modalities.

Contents

List of Tables

List of Figures

Chapter 1

Introduction

1.1 Thermal therapy

Thermal ablation, hyperthermia, and cryotherapy are forms of thermal therapy, which is the treatment of medical conditions through the application of heat or cold. Thermal therapy has been widely applied to treat cancer. Hyperthermia at 39-43°C sensitizes tissues to chemotherapy and radiation through mild heating, while thermal ablation (over 50°C) directly kills tissues with heat, and cryoablation (under -40°C) kills tissues through freezing [1-6]. Thermal ablation and cryoablation have been successfully applied clinically for the treatment of unresectable liver tumors, metastatic bone cancer, osteoid osteoma, uterine fibroids, cardiac arrhythmia, various neurological disorders, benign prostate hyperplasia, mennorhagia, varicose veins, and other disorders [6-14].

Some thermal therapy modalities are applied invasively, while others are minimally invasive or noninvasive. A variety of external electromagnetic and ultrasound-based devices are available for noninvasively applying hyperthermia [15, 16]. Thermal ablation can also be

performed noninvasively using external high intensity focused ultrasound (HIFU) transducers and some microwave devices [14]. Endocavity ultrasound devices are also available for ablating tissues from within body cavities [17]. However, thermal ablation and cryotherapy are often performed minimally invasively using radiofrequency (RF) ablation, microwave ablation, laser ablation, or cryoablation, with a small applicator inserted directly into the tissues to be ablated [17-21]. Multiple probes can be used to ablate large lesions [3, 6, 17, 22, 23].

1.1.1 Thermal ablation

Thermal ablation employs heat to kill targeted tissue. Tumor volumes can be locally heated to ablate the tumor with minimal damage to healthy tissue. Upon heating, protein denaturation and cell membrane rupture cause rapid cell death, generally followed by coagulative necrosis [5, 24-26]. Water vaporization and carbonization kill cells in tissues that surpass 100°C, which is generally avoided in most forms of thermal ablation [26-28]. 4-6 minutes at 50-52°C is generally sufficient to kill cells [26], while cell death can be achieved within seconds over 60°C [26, 28].

Thermal ablation has advantages as compared to other cancer treatment modalities in that it is applied non-invasively or minimally invasively, there is no intrinsic limit to the number of times it can be performed, it does not employ ionizing radiation, it is a localized therapy, and it has few systemic side effects [6, 28-30]. The minimal or noninvasiveness of thermal ablation often results in reduced mortality, reduced morbidity, and lower costs than surgery [6]. Treatment can be performed multiple times if necessary, as it is not limited by a maximum lifetime dose, unlike radiation therapy [6, 19, 20]. Unlike chemotherapy, thermal ablation is applied locally with limited side effects to surrounding tissues. Thermal ablation is sometimes used to treat patients who are not candidates for surgery and for whom radiation and

chemotherapy are not applicable [6, 31]. Thermal ablation can also be applied in combination with other therapies such as radiation or chemotherapy [23].

1.1.2 Thermal dosimetry

The amount of time necessary to obtain a biological effect through heating decreases exponentially as temperature increases [32]. Thermal damage can be described using an Arrhenius relationship considering the temperature, time, and activation energy necessary to produce a physiological effect such as protein denaturation or the percentage of cells killed [24, 32, 33]. Alternatively, thermal damage can be expressed in thermal dose, which is based on the Arrhenius relationship [24, 33].

There is generally a breakpoint temperature above which the base of the exponential relationship between time, temperature, and physiological effect changes, due to a lack of development of resistance to thermal cytotoxicity during heating above the breakpoint [32]. Sapareto and Dewey assumed a breakpoint at 43°C based on previous studies, and defined thermal dose to describe heating at different temperatures and time periods in terms of the number of equivalent minutes at 43°C (EM43°C) [34]. While thermal doses of 120-240 EM43°C are lethal to some cells, this is highly dependent on tissue type [14]. Arrhenius and thermal dose parameters vary among different tissues, which have varying sensitivities to heat [32, 33]. 240-540 EM43°C is generally considered a lethal thermal dose threshold [14].

1.1.3 Hyperthermia

Local hyperthermia is generally applied as an adjuvant therapy to chemotherapy and/or radiation [1, 2]. It acts both by directly killing cells and by enhancing the effects of radiation and chemotherapy. During hyperthermia, tissues are warmed to 40-45°C and maintained at that

temperature for about 30-60 minutes [1, 2, 6, 28, 35]. Hyperthermia at 40-43°C results in increased blood flow to tumor tissue, and thus increased oxygenation, improving the efficacy of radiation and chemotherapy [2, 36, 37]. Hypoxic cells heated to 40-43°C and cells in the S-phase of mitosis, which are both relatively radioresistant, are more sensitive to lethal effects of hyperthermia [5, 36, 38]. Hyperthermia thus enhances the effects of radiation by killing radioresistent cells and by impairing the cells' ability to repair DNA damage caused by radiation [37, 38]. Hyperthermia also enhances the cytotoxicity of many chemotherapeutic drugs [36]. Furthermore, local hyperthermia has been used to trigger drug release from nanocarriers, such as liposomes, for targeted drug delivery to tumors [39, 40].

1.1.4 Cryoablation

Cryoablation kills tissue by lowering the temperature to -20 to -40°C, which is lethal to cells [6, 18]. Multiple freeze-thaw cycles are often used to ensure cell death [18]. Cryoablation is generally performed using cryoprobes with diameters of 2-8 mm [3]. A cryogen, generally liquid nitrogen or argon gas, is circulated to the tip of the cryoprobe, cooling it to about -190 to -100°C [3, 6]. An ice ball forms around the tip of the cryoprobe [18], resulting in ablation through freezing. Each freeze cycle may take around 8-15 minutes, and each thaw cycle may take around 15-20 minutes [18].

Cell death due to cryoablation occurs via several mechanisms. Ice crystals form upon cooling, and then fuse to form larger crystals upon thawing, causing cell death by disrupting organelles and cellular membranes [4, 18]. Ice crystals also damage blood vessels, resulting in vascular thrombosis, ischemia, reperfusion injury, and tissue necrosis [3, 41]. During slow freezing rates, which occur further from the cryoprobe, ice crystals form first in extracellular spaces, creating a hyperosmolar extracellular environment that draws water from inside the cells,

causing dehydration [18]. Changes in pH, protein denaturation, and disruption of cell membranes also occur in slowly cooled regions [18, 41]. In regions cooled to temperatures insufficient for quick cell death, cells may be destroyed over longer time spans through apoptosis or immunological responses [3].

1.2 Electromagnetic ablative modalities

Radiofrequency ablation produces heating via an electric current [20, 42]. An AC radiofrequency current (~375-1000 kHz) flows through the tissues between two electrodes, causing agitation of the ions in the tissues [6, 20, 42, 43]. This agitation results in joule heating [20, 42]. Most of the energy is deposited in the tissue within a few millimeters of the electrode, with wider tissue volumes heated through conduction [44]. Radiofrequency ablation is generally applied at ~90°C [43] and can sometimes be completed within 10 minutes, with longer treatment times necessary for large tumors [6, 20, 23].

Microwave ablation, like radiofrequency ablation, is an electromagnetic heating modality. It differs from RF ablation in that it uses microwaves (900-2500 MHz), and in that, although it also employs an electromagnetic field in the tissue, an electric current does not flow through the tissues [19, 44, 45]. Microwave ablation generates heat through dielectric hysteresis, in which polar water molecules in the tissues continually realign themselves with the rapidly changing electromagnetic field [19, 22, 44, 45].

In laser interstitial thermotherapy, a third electromagnetic ablative modality, heat is generated through the absorption of light produced by a laser at 800-1064 nm [21, 46]. Thermal lesions produced by a single laser fiber tend to be relatively small (1-2 cm diameter) [21, 23].

However, unlike RF ablation, laser ablation can be performed under MR guidance and monitoring [23, 47, 48].

1.3 Ultrasound ablation

Ultrasound-based ablation modalities utilize the absorption of acoustic energy and/or acoustic cavitation to ablate tissue [49-52]. Thermal ablation occurs due to absorption of the acoustic (pressure) wave, a process caused by friction and relaxation [53]. In non-viscous mediums, particles move back and forth in an acoustic field roughly in phase with a pressure wave [54, 55]. In viscous mediums, viscous forces between the particles prevent them from reversing their direction quickly, resulting in the velocity lagging behind the changing pressure field [54, 55]. The energy loss over each cycle, which is greater at higher frequencies, results in viscous heating caused by friction [54, 55].

During the rarefaction portion of the pressure wave, local pressures can be low enough to create gas bubbles, a mechanical process known as cavitation that results in further destruction of tissue [49, 51, 52, 56]. Tissues are more susceptible to cavitation at lower frequencies, as the peak negative pressure thresholds necessary to induce cavitation are lower at lower frequencies [57, 58].

Therapeutic ultrasound waves are emitted from piezoelectric materials. Lead zirconante titanate (PZT) is a common piezoelectric material used in medical applications. Piezoelectric materials have an asymmetric lattice structure that, when placed in an electric field, expands or contracts. As the electromagnetic field alternates direction, the material expands and contracts, emitting a pressure wave. Alternatively, a pressure wave flowing through the piezoelectric material, causing displacements of positively and negatively charged portions of the lattice, will

result in the generation of an electric field. Thus, piezoelectric materials can sense acoustic (pressure) waves and convert them into an electrical signal, or take in an electric signal and convert it into a pressure wave.

Ultrasound transducers can be designed for spatial control of the acoustic output. Transducers can be sectored, with separate power control for each segment, and/or focused. When sectoring is employed on tubular transducers, more power can be applied to one side of the transducer than another, providing directional control of the acoustic output (Figure 1.1A). Another technique is to use phased arrays, in which the phases of the waves emitted by an array of many small transducers are varied, or curved transducers to aim or focus the beam (Figure 1.1B). The focus can then be scanned though the tissue to heat the full volume.

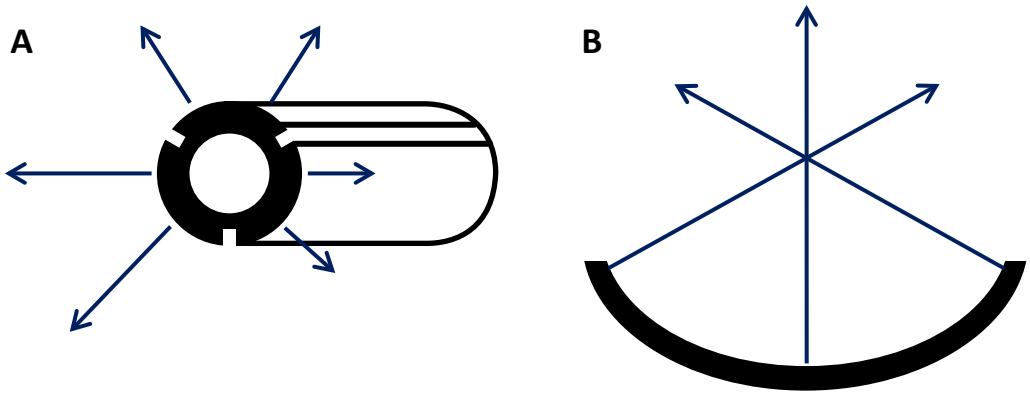

Figure 1.1 Tubular transducers emit acoustic waves radiating radially outward. When sectored, variable power control allows for more, less, or equal energy (arrows) to be emitted from one side than another. (B) Curved bowl-shaped transducers can be used to produce heating at a focal point.

Ultrasound-based ablation technologies have advantages over other ablation modalities in that energy deposition patterns can be shaped to conform to a target volume, the transducer does not need to be placed directly within the tissue to be treated, and ultrasound devices can be designed to be MR-compatible. Ultrasound can be applied noninvasively by an external applicator with a focus within the target. Alternatively, ultrasound can be emitted from a

directional applicator either inside or next to the target, allowing for greater flexibility in ultrasound applicator placement than with other ablation modalities. Wavelengths, which are dependent on frequency (generally 1-15 MHz), are relatively small, in the range of ~0.1-1.7 mm in soft tissue [17, 59]. To create an energy deposition pattern matching the shape of the target, an acoustic focal point can be scanned through a target, or ultrasound waves can be emitted from directional transducers. This property provides ultrasound with better spatial precision than other ablative modalities, allowing for carful control of the shape and size of the thermal lesion and for preservation of untargeted anatomy. Lastly, ultrasound devices can be designed to be nonmagnetic and to create little or no interference with MR signals. Thus, ultrasound ablation can be monitored in 3D with MR temperature imaging, for assurance that the whole target has been ablated and that critical anatomy is spared.

Clinically relevant depths of acoustic penetration, which are dependent on frequency and tissue type, generally range from 1-20 cm in soft tissue [59]. Low frequency waves with high penetration are emitted by external focused applicators, while high frequency waves that are locally absorbed are emitted by applicators inserted directly into the tissue to be treated.

1.3.1 HIFU

High intensity focused ultrasound (HIFU) utilizes focused ultrasound waves in the ~0.6-7 MHz range to ablate tissue [49-52, 56]. This transducer is often external to the body, but can also be positioned in body cavities for applications such as prostate cancer treatment [52]. The wave traverses surface tissues with low intensities and focuses to a small point at which the intensity is high enough for ablation [49, 50].

The zone ablated by a single sonication is isolated to the focal region and is generally roughly 10-20 mm long and 1-2 mm wide, so the focus must be scanned through the entire target

volume for full ablation [49]. This process is slow and can take hours for large treatment volumes [52, 60]. MR temperature imaging is often used to guide treatment, although ultrasound guidance can be performed as well [49, 50, 56, 60, 61].

HIFU transducers require an acoustic window from the transducer to the target tissue unimpeded by bone or gas [52]. Ultrasound waves are reflected by gas in the lungs and bowel and are rapidly absorbed by bone tissue [52, 60]. Thus, targets obscured by the lungs or by bone cannot be treated with HIFU [52, 62, 63], nor can treatment be performed if sensitive anatomy, such as nerves, are in close proximity to bones that would be overheated.

1.3.2 Endocavity and intraluminal ultrasound ablation

A variety of ultrasound-based ablation devices have been developed for deployment within body cavities or lumen. Endocavity and intraluminal ablation techniques have been applied towards treatment of tumors near accessible body cavities, such as prostate and esophageal cancers [17]. Applicators in larger cavities may use focused HIFU transducers, while applicators designed to fit within smaller diameters often use cylindrical, rotating planar, or rotating curvilinear transducers [17, 64]. While HIFU transducers have a small focus that is often centimeters away from the transducer, cylindrical, rotating planar, and rotating curvilinear transducers radiate diffusely outward, ablating a volume adjacent to the transducer [64-66].

1.3.3 Interstitial ultrasound ablation

Interstitial ultrasound applicators provide an energy delivery platform that utilizes acoustic radiators designed for percutaneous placement inside or adjacent to a target and, unlike HIFU, do not require an acoustic window between the target and the skin [67, 68]. Interstitial ultrasound applicators can employ an array of multiple planar or tubular ultrasound transducers (1.2-4 mm x

5-17 mm) [17, 67, 69]. The applicators can be deployed within a water-cooled plastic catheter, or can be directly coupled to tissue [70]. Tubular transducers operated at ~7 MHz are considered in the majority of this work. Interstitial ultrasound ablation with these devices is generally completed within ~4-20 minutes of heating using applied electrical powers of ~5-20 W [68].

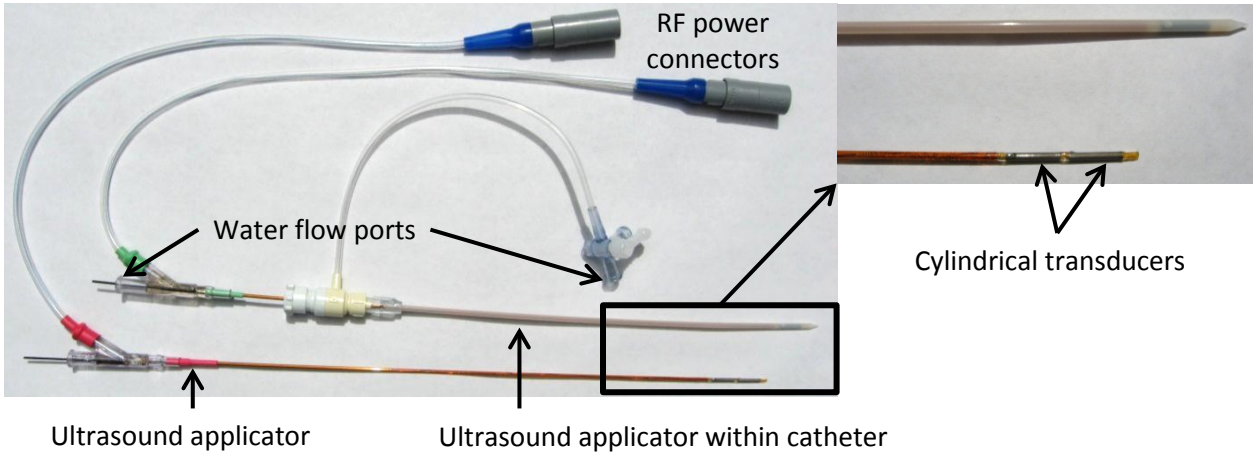

Figure 1.2 Interstitial ultrasound applicators with tubular transducers.

Air-backed tubular transducers are typically mounted on a polyimide tube. Deionized, degassed cooling water flows through the center of the applicator, out the tip, and back through the catheter over the transducers. The cooling water also serves to acoustically couple the transducers to the catheter and tissue. Multiple independently powered tubular transducers can be positioned along the length of an applicator and sectored longitudinally to allow for directional heating control along the length and angular expanse of the applicator. The applied power can be dynamically changed during treatment and can be tailored in length and angle to conform the ablated region to a predefined target volume.

In vivo studies in the brain, prostate, liver, and other soft tissues have demonstrated compatibility of these interstitial applicators with real-time MR temperature monitoring and have shown their capacity to produce thermal lesions within 5-10 min with spatial control and radial

depths of 15–21 mm [70-74]. In general, image-guided interstitial ultrasound can generate well-localized thermal lesions with shapes tailored to the target volume, producing excellent spatial control compared to RF ablation, microwave ablation, laser ablation, and cryotherapy [72, 75].

1.4 Thermal ablation of bone tumors

Primary and metastatic bone tumors remain a significant clinical problem for local control and pain palliation. Bone metastases are highly prevalent; they have been observed upon autopsy in 65-75% of breast and prostate cancer patients [76, 77]. Primary bone tumors are far less common, making up only 0.2% of primary neoplasms [78]. Soft tissue tumors in the paraspinal spaces are also rare [79]. Bone tumors can be osteolytic (inducing resorption of calcified bone tissue), osteoblastic (inducing increased calcification of bone), or a mixture of both osteolytic and osteoblastic [80]. While survival rates for some forms of primary bone cancer are relatively high (60% for localized osteosarcoma and Ewing's sarcoma) [81, 82], the prognosis for patients with bone metastases is often very poor, so treatment goals for metastatic bone disease are generally directed toward local control or palliation [83-87]. The aims of palliative bone cancer treatment are to relieve pain and to maintain or restore mechanical stability and neurological function [85-88]. Treatment options for primary and metastatic bone tumors include radiation, surgery, drugs, and thermal ablation [86-90]. Surgery and radiation, particularly intensity modulated radiotherapy, are two means of treating paraspinal tumors [79, 91, 92]. External beam radiation is the standard of care for treatment of painful bone metastases [8, 84, 86], while radiofrequency ablation is now the standard of care for treatment of osteoid osteoma of the appendicular skeleton [7, 8]. Cement can be injected into eroded bones after ablation for greater mechanical stability [83, 84, 93, 94].

Thermal ablation has previously been investigated both for the treatment of primary bone tumors and for the palliative care of bone metastases [11, 12, 19, 84, 95-101]. Bone tumors have been treated externally using focused ultrasound ablation [11, 12, 99] and percutaneously with radiofrequency ablation [96-98], microwave ablation [19], laser ablation [100], and cryoablation [101]. RF ablation is the most widely used, followed by laser ablation. Externally applied focused ultrasound ablation has gained attention in recent years, but it requires an acoustic window to access the bone, and it ablates the pain-sensing nerve endings in the periosteum around bone with limited penetration through intact cortical shell [11, 12, 99]. The volumes treated with thermal ablation vary widely in size, from 5 mm osteoid osteomas to 10 cm regions of necrosis in chordomas [102, 103].

Thermal ablation has been considered in the spine [89, 93, 103-110], which is the most common location of bone metastases, with tumors observed upon autopsy in up to 40% of cancer patients [111]. To prevent heat-induced neurological damage, the spinal cord and spinal nerves must be kept below 45°C [104] and 10-30 EM43°C [112]. Tumor locations in close proximity (within 1 cm) to the spinal cord, as well as blastic lesions, have sometimes been considered exclusion criteria for RF ablation [105]. The spinal cord can be thermally insulated by cortical and cancellous bone surrounding vertebral tumors, allowing for ablation of some lesions in the vertebrae [104]. Despite the absence of insulating bone, relief of pain caused by vertebral tumors immediately adjacent to the spinal canal has been attained following thermal ablation [93, 104]. The lack of neurological complications following these procedures has been attributed to the cooling flows of cerebrospinal fluid (CSF) and of blood within epidural vessels [106], as well as to the feedback of patients under conscious sedation [93]. In some cases with posterior wall

destruction, injected gases applied to displace and insulate the spinal canal has successfully prevented neurological complications during laser, RF, and cryoablation [103, 113].

As discussed in subsequent sections, I am investigating the use of interstitial ultrasound as an alternative percutaneous ablation modality for the treatment of tumors within and near bone, and the vertebrae in particular. Because the ultrasound attenuation coefficient of bone is very high, significant heating occurs at the bone surface when ultrasound is applied, but very little energy penetrates deep into the bone [114, 115]. This property, along with reflection at bone/soft tissue interfaces due to an impedance mismatch [59], may potentially allow for thorough heating at the borders of tumors adjacent to or within bone, while preserving any sensitive tissues on the other side of the bone.

1.5 Techniques for monitoring thermal ablation

Thermal ablation near sensitive anatomy should be closely monitored to ensure thorough ablation of the target volume while avoiding overheating of untargeted tissue. This is of particular importance in the spine, in which tumors may be within close proximity to critical anatomy, such as the spinal cord, spinal nerves, aorta, vena cava, esophagus, trachea, and lungs.

Invasive temperature sensors can be inserted into tissue to provide thermometry at a few distinct points. Alternatively, image-based techniques can provide thermometry at all voxels in a 2D or 3D volume. MR temperature imaging (MRTI) has been widely used to monitor ablation performed by MR-compatible heating modalities, such as ultrasound and laser ablation [47, 48, 50, 116]. RF ablation, which cannot be performed in conjunction with MR imaging, can be monitored using ultrasound-based techniques [47, 117-119].

1.5.1 Invasive temperature measurements

There are a variety of minimally invasive needle-based devices to measure temperature, including thermocouples, thermistors, and fiber-optic temperature sensors. Fiber-optic temperature sensors can be used in lieu of thermocouples in cases in which MR-compatibility is required [118].

Invasive temperature measurements in bone can be more complicated than in soft tissue, because a needle may need to be inserted though hard bone. Invasiveness is an inherent downside to minimally invasive temperature measurements, as is the limited number of measurement points. However, invasive temperature measurements have an advantage in that they are not dependent on tissue type, as is the case in many image-based techniques. Some ablation devices contain thermocouples or thermistors mounted along their length [70, 120], but this is less applicable with catheter-cooled devices, as the device temperature may be significantly lower than the tissue temperature.

Thermocouples are subject to thermal smearing artifacts due to conduction along the wires inside the probe and along needles within which the probe may be operated [121]. Viscous forces between tissue and a thermocouple vibrating in an acoustic field result in heating that produces further artifacts [122].

1.5.2 MR-based temperature monitoring

There are a variety of temperature-dependent properties that can be used to measure temperature in tissue using MRI, including proton resonance frequency (PRF), T1 relaxation times, T2 relaxation times, and diffusion coefficients [123]. PRF-based phase mapping is the most common technique [123]. In contrast to most other temperature-dependent tissue properties, the

temperature-dependence of the PRF shift does not vary significantly among aqueous soft tissues [123].

MRTI has advantages over minimally invasive temperature-sensing modalities in that it is completely non-invasive, and in that it provides temperature data in all the voxels in a volume, as opposed to at a few discrete points. However, the use of MRI greatly adds to the cost of the procedure, all equipment used must be non-magnetic, and treatment must be performed within the confines of a MR scanner.

Unlike HIFU, in which the acoustic focus is scanned through the tissue and each focal point is ablated within a few seconds, for a total treatment time of up to a few hours, interstitial ultrasound ablation is often performed with a single, larger region heated for minutes at a time. Thus, in cases when sensitive anatomy is not in danger and real-time power feedback control is not performed, interstitial ultrasound ablation can tolerate slower temperature update times than HIFU.

Conventional MRTI techniques can be difficult to apply within bone. Cortical bone has a very low MR signal, due to a very short T2 relaxation time (0.42-0.50 ms) [124], and cancellous bone is highly inhomogeneous, with the interstitial spaces between osseous trabeculae filled with fatty bone marrow. Bone marrow is approximately 15-40% water, 40-80% fat, and 5-20% protein, with more fat filling the trabecular spaces of older adults than those of young children, particularly in the appendicular skeleton [125]. The presence of fat in a voxel can produce distortions in the phase changes observed, causing errors in PRF-based thermometry [126]. A high fat signal and susceptibility artifacts from osseous trabeculae make the standard PRF technique inapplicable to cancellous bone. Other techniques, such as T1 mapping, possibly

using ultrashort TE pulse sequences, and T2 mapping may be more suitable for monitoring temperature in bone [127, 128].

1.5.3 CT-based temperature monitoring

CT has been considered as a means of 3D image-based temperature monitoring [47, 117]. The CT number of some tissues and biological fluids changes linearly with temperature [117, 129]. However, this relationship varies between tissue types, and even among samples of the same tissue type, resulting in inaccuracies in temperature measurements [117]. Temperature measurements can be also distorted by metal artifacts, beam hardening, and vaporization [117]. CT-based temperature monitoring, developed for applications in relatively homogenous liver tissue [117], may be less applicable in heterogeneous spinal tissues, which contain cortical bone, trabecular bone, bone marrow, intervertebral disks, nerves, and other tissues.

1.5.4 Ultrasound-based temperature monitoring

Ultrasound-based temperature monitoring has advantages over other image-based techniques in that it does not use ionizing radiation and in that it is far less expensive than both MR and CT. B-mode ultrasound provides little to no temperature contrast in tissues below the boiling point of water. However, there are several temperature-dependent tissue properties that allow for the use of ultrasound in monitoring thermal therapy. These include the speed of sound, density, backscattering properties, and the acoustic attenuation coefficient [119]. Acoustic properties vary between different tissue types, making techniques based on these properties less applicable to monitoring thermal therapy in heterogeneous tissues in which the acoustic properties vary or may not be known [130, 131].

Heating-induced thermal expansion and changes in the speed of sound can be applied to monitoring thermal therapy using ultrasound. These effects result in a change in the time echoes are received, which appears as a spatial shift in ultrasound images [131]. Tissue motion can introduce artifacts in the apparent echo time, but this can be compensated for in post-processing [118, 131].

Ultrasound elastography can be applied to identify coagulated tissue, which is stiffer than viable tissue [132]. With this technique, the tissue is externally compressed, vibrated, or displaced, and the relative motions of soft and stiff tissues are quantified under ultrasound imaging to identify stiff thermal lesions [132, 133]. Ultrasound elastography and strain imaging methods have been applied *in vivo* to monitor RF ablation in the liver, and are under investigation for other applications, such as monitoring minimally invasive ultrasound ablation of the prostate and HIFU ablation [133-135]. MR-based elastography has also been applied to evaluate changes in the mechanical properties of tissue caused by thermal ablation [136-138], though the introduction of MRI significantly adds to the cost and complexity of the procedure.

Ultrasound contrast agents have also been applied to monitor thermal therapy. Ultrasound contrast agents generally consist of gaseous microbubbles surrounded by stabilizing shells, and flow through the vasculature. The disappearance of contrast from a tissue volume can indicate coagulation of the vasculature [139], however, tissue can be lethally ablated without immediate loss of blood perfusion [25].

Like MR, although ultrasound-based temperature monitoring has been successfully applied in soft tissue [131], it is not easily applied to bone. Due to the high acoustic attenuation coefficient of bone and the large difference between the acoustic impedances of bone and soft

tissue, ultrasound at most standard imaging frequencies cannot penetrate deep into bone, limiting its use.

1.6 Simulations and treatment planning

Numerical models provide an important tool for predicting tissue damage caused by thermal ablation, and are applied in device design and treatment planning. These computational models can calculate power deposition and estimate the temperature elevations in tissue, which can be correlated to thermal damage, based upon the applied powers and material properties of the tissue. Models can consequently determine the appropriate applicator placements and treatment parameters for full ablation of a target while avoiding damage to sensitive anatomy [140].

Simulations of temperature distributions during thermal therapy are often based on Pennes bioheat equation, which describes heat transfer in biological tissues as a function of material tissue properties and heat deposition. These properties include the effects of blood perfusion, thermal conduction, and heat capacity. Because this differential equation is nonlinear, temperatures are generally calculated using numerical techniques, such as the finite element method or the finite difference method, rather than analytical techniques [141]. Thermal damage can be calculated as a function of temperature, time, and tissue properties using Arrhenius models or thermal dose [141].

For greater accuracy, models may include transient changes in temperature-dependent tissue properties, such as dielectric conductivity, the ultrasound attenuation coefficient, and blood perfusion rates [141, 142]. Tissue desiccation and water vaporization have significant effects on energy propagation, including as reduction of thermal conductivity, reflection of

ultrasound, and reduction of RF current flow [44, 75, 141]. Thermal simulations that do not consider water vaporization may be invalid above the boiling point of water [143].

The effects of blood flow in capillaries and larger vessels should be considered during simulations of thermal therapy for accurate modeling [144]. Blood flow causes tissue temperatures to veer towards physiological temperatures, cooling heated tissues and warming cooled tissues [145-147]. This can result in insufficient treatment, especially in the vicinity of large blood vessels, if not taken into account during treatment planning [145, 146]. Blood perfusion in capillaries can be approximated as a heat source or sink that scales linearly with temperature, while large blood vessels generally need to be considered individually [148-150]. Blood in capillaries tends to be in thermal equilibrium with surrounding tissues, while the temperatures of fast-flowing blood in large (diameter > ~3 mm) blood vessels tend to not be significantly affected by thermal therapy [151, 152]. Convective cooling caused by large blood vessels can produce inhomogeneities in temperature distributions; adjacent tissues are often closer to physiological temperatures than tissues further away from large blood vessels [146, 152].

In large homogenous tissues, such as the liver, tissue may be modeled as an homogenous block, but in heterogeneous tissues with disparate material properties, and in cases in which blood flow though large vessels is modeled, simulated geometries may be based on individual patient anatomies [141, 153, 154]. Patient-specific models provide detailed morphological information, such as the geometry of the vasculature and the shapes and structures of tissues with disparate material properties. Patient-specific models can be created based on segmented 3D image sets, such as CT or MR scans. Simulated temperature or thermal dose distributions from

one or more ablations can be overlaid on 3D image sets for better visualization during treatment planning and as a tool for determining optimal device placements and insertion paths [140, 144].

Models applied in treatment planning should compute quickly, on the order of real-time, after each adjustment to the considered treatment parameters is made [141]. Comprehensive, highly complex models may compute on the order of hours, but fast treatment planning algorithms are also available [141].

In the field of acoustics and bone, simulations have been employed in the past to correlate the acoustic properties of bone to structural properties and disease states [155, 156], and to study intended and unintended bone heating during ultrasound imaging and thermal therapy [157-161]. Simulations have been used to determine how to minimize painful heating of nontargeted bone [157-160] and to determine how bone affects acoustic and heating distributions near target tissue [162-165]. In the field of bone tumor treatment, Lu *et al*. and Staruch *et al*. have simulated heating by external focused ultrasound transducers [166, 167]. To gain a more thorough understanding of the electric field and thermal distributions in the spine and as a step towards treatment planning, Ryan *et al.* [168] and Bien *et al.* [169] have developed generalized models and a patient-specific model, respectively, of RF ablation in the spine.

1.7 Research goals

Interstitial ultrasound ablation may potentially be able to take advantage of preferential bone heating and the thermally and acoustically insulating nature of bone to enhance and speed up treatment of osteolytic bone tumors and tumors adjacent to bones. The directional control inherent to interstitial ultrasound could be of particular use in and near the spine. The effects of bone on heating must be well understood before ultrasound ablation can be performed in the

vicinity of the spine. Great care must be taken to not damage the spinal cord or other critical anatomy near the vertebrae. Numerical models can provide a useful tool for the evaluation of temperature and thermal dose distributions produced by interstitial ultrasound ablation of heterogeneous tissues. The goals of this study are to investigate the applicability of interstitial ultrasound ablation of tumors in and near the spine and other bones, and are summarized as follows:

1. Develop numerical models of interstitial ultrasound ablation involving bone, incorporating approximations that reduce model complexity and computation times, and create a platform for the production of patient-specific numerical models.
2. Experimentally validate the numerical models and approximations through comparison to invasive temperature measurements, MR temperature imaging, and measurements of visibly coagulated volumes in phantom, *in vivo,* and *ex vivo* tissue models, with the applicator placed both directly into bone and in soft tissue at several distances from bone.
3. Using both experimental temperature measurements and simulations, characterize the effect of bone on the heat distributions in bone and soft tissue produced by interstitial ultrasound transducers.
4. Through comprehensive patient-specific models and parametric studies, assess the feasibility of interstitial ultrasound ablation of paraspinal targets and of osteolytic vertebral tumors. Determine the benefits and limitations of interstitial ultrasound ablation in and near the spine.
5. Develop potential treatment delivery strategies and guidelines for interstitial ultrasound ablation of vertebral tumors, soft tissue tumors near the spine, and appendicular bone tumors.

6. Investigate non-invasive MR and ultrasound-based techniques for monitoring interstitial ultrasound ablation both within bone and in soft tissue adjacent to bone.

1.7.1 Dissertation content

This dissertation investigates interstitial ultrasound ablation of osteolytic tumors and tumors adjacent to bone, with a focus on the spine.

Chapter 1 provides an introduction to thermal therapy and bone tumors.

In Chapter 2, a series of four approximations for numerically modeling interstitial ultrasound ablation involving bone are developed. To determine which approximations could be applied to reduce computation times and the complexity of the models without any significant losses in accuracy, they are evaluated through comparison to one another and through parametric studies.

In Chapter 3, the four sets of approximations are further evaluated and validated through comparison to experiments. Temperature measurements and evaluation of thermal lesion sizes are performed in phantoms, *ex vivo* tissues, and *in vivo* tissues using invasive thermometry, MRTI, and measurement of visible tissue coagulation. Experiments are performed with the applicator inserted both directly into bone and with it inserted into soft tissue at several distances from the bone surface. These experimental studies are also applied to investigate the effect of bone on the temperature and thermal dose distributions produced during interstitial ultrasound ablation. The majority of the work in Chapters 2 and 3 is presented in a recently published article by Scott et al. in the *International Journal of Hyperthermia* [170].

In Chapter 4, a series of treatment parameters and guidelines for ablation of tumors within and near the spine and other bones are developed using parametric studies. Necessary

safety margins for the preservation of nerves and other sensitive tissues are determined. Limitations of the technology are identified.

In Chapter 5, a series of patient-specific models selected to bracket the range of clinical use are created to evaluate the feasibility of interstitial ultrasound ablation of osteolytic vertebral tumors and tumors near the spine, and to identify potential treatment delivery strategies. Benefits of interstitial ultrasound ablation in the vicinity of the spine, as compared to other ablative modalities, are identified. A portion of the work done in this chapter and the techniques described herein for the creation of patient-specific models are published in a SPIE proceedings article by Scott et al. [171]. The majority of the work in Chapters 4 and 5 is presented in an journal article by Scott et al. currently in review [172].In Chapter 6, a summary of this work in interstitial ultrasound ablation involving bone and a discussion of future directions are presented.

Appendix A contains a technical description of the calculation of acoustic heat deposition in patient-specific models containing irregularly shaped tissue volumes.

In Appendix B, phase-shift ultrasound contrast agents for monitoring interstitial ultrasound ablation of tissues adjacent to bone are investigated.

Chapter 2

Development of approaches for modeling interstitial ultrasound ablation of tumors within or adjacent to bone

2.1 Abstract

Purpose: The goal of this study was to develop numerical biothermal and acoustic models of interstitial ultrasound ablation involving bone.

Methods: 3D transient biothermal and acoustic finite element models were developed, employing four approximations of 7 MHz ultrasound propagation at bone/soft tissue interfaces. The various approximations considered or excluded reflection, refraction, angle-dependence of transmission coefficients, shear mode conversion, and volumetric heat deposition. Parametric and comparative simulations were performed to investigate the impact of bone on ablation and to evaluate the four approximations.

Results: Models using simplified approximations produced temperature profiles closely matching more comprehensive models. There was a discrepancy of less than 2.6% between the calculations made by the four models of the maximum tumor radius that could be ablated in the presence of bone. Simulations indicated that the presence of nearby bone can increase the volume of soft tissue that can be ablated, with a greater impact when the ultrasound attenuation coefficient of the soft tissue is low.

Conclusions: Models of 7 MHz interstitial ultrasound ablation of bone can be simplified to exclude reflection, refraction, and shear mode conversion, and can assume that all heat is deposited at the surface of the bone with minimal losses in accuracy as compared to more comprehensive models.

The majority of the work in this chapter is published in a research paper by Scott et al. ("Approaches for modeling interstitial ultrasound ablation of tumors within or adjacent to bone: Theoretical and experimental evaluations," 2013) [170].

2.2 Introduction

The impact of bone, either surrounding or adjacent to a soft tissue tumor, on thermal ablation with interstitial ultrasound ablation has not been well defined. It is a major component in understanding the performance of interstitial ultrasound ablation of targets involving bone, providing the motivation of this study.

Reflection, refraction, and shear mode conversion play significant roles in ultrasound wave propagation at bone/soft tissue interfaces, making bone surfaces much more complex to acoustically model than soft tissue interfaces. Due to high differences between the acoustic impedances of bone and soft tissue, a significant portion of the acoustic energy traveling though

soft tissue is reflected upon reaching a bone surface, with the remaining energy transmitted at a refracted angles [114, 157]. Shear wave transmission in fluids and soft tissues is negligible, but at incidence angles above about 27°, the majority of the acoustic energy transmitted into bone is converted to shear waves [114, 157]. Furthermore, the high ultrasound attenuation coefficient of bone, over an order of magnitude higher than that of most soft tissues [59], results in considerable heating at bone surfaces when ultrasound is applied [115, 157]. These interactions at bone surfaces may require special consideration in acoustic models involving bone.

Previous studies have taken a variety of approaches to modeling ultrasound propagation in and near bone. To calculate the acoustic power loss in bone as a function of depth and incident angle, Chan *et al*. calculated the full stress tensor, with shear and longitudinal components, in bone as a function of incidence angle instead of throughout a 3D region [114]. Others did not consider shear mode conversion, which allowed for simpler implementation of full wave methods [158] or the Rayleigh-Sommerfeld diffraction integral [159, 163, 165] to simulate propagation through the interface. Some studies modeled ultrasound intensity with an exponential falloff from the transducer and multiplied the intensity in the bone with a transmission coefficient that may [173] or may not [161, 166] have considered the incident angle and shear mode conversion.

A recent study investigated bone heating with cylindrical transurethral ultrasound transducers [160]. They applied numerical models with constant transmission coefficients independent of incidence angle and did not consider reflection [160]. However, many prior acoustic and thermal simulations of ultrasound near bone have been performed with either planar transducers [159, 161, 165, 174], assuming low incidence angles and purely longitudinal transmission [161, 174], or focused [157, 158, 163, 166, 173] transducers.

The objectives of this study are to develop 3D transient biothermal and acoustic models specific to interstitial ultrasound ablation of tumors within or adjacent to bone. Different approaches for approximating ultrasound propagation at bone/soft tissue interfaces are developed and incorporated into the models. The models are appraised using parametric studies and through comparison to one another.

2.3 Materials and Methods

2.3.1 Finite element analysis of heat transfer

In order to investigate the effects of bone on acoustic propagation, temperature distributions, and thermal dose distributions during interstitial ultrasound ablation, 3D finite-element models were developed based on the Pennes bioheat transfer equation [148]:

$$\rho c \frac{dT}{dt} = \nabla \cdot \mathrm{k}\nabla \mathrm{T} - \omega \mathrm{c}_b (T - T_b) + Q \qquad 2.1$$

where ρ is density (kg/m^3), c is specific heat capacity (J/kg/°C), T is temperature (°C), t is time (s), k is thermal conductivity (W/m/°C), ω is blood perfusion (kg/m^3/s), Q is heat deposition due to ultrasound (W/m^3), and the subscript b refers to blood. Capillary blood temperature is assumed to be 37°C. Dynamic changes in perfusion due to coagulation are incorporated into models of *in vivo* ablations. To simulate the effect of heating-induced microvascular stasis, perfusion is reduced to zero at a thermal dose threshold of 300 EM43°C [142], with thermal dose (t_{43}) calculated according to Sapareto and Dewey 2.2) [34]:

$$t_{43} = \int_0^t R^{43-T} dt', \quad R = \begin{cases} 0.5, & T > 43 \\ 0.25, & T \leq 43 \end{cases} \qquad 2.2$$

where T is temperature (°C) and t is time (min). The tissue and material properties used in this study are summarized in Table 2.1.

Medium	Density (kg/m^3)	Velocity (m/s)	Attenuation (Np/m/MHz)	Thermal conductivity (W/m/°C)	Specific heat (J/kg/°C)	Perfusion rate (kg/m3/s)
Muscle	1041 [59]	1576 [59]	5 [130]	0.5 [59]	3430 [59]	0.692 [59]
Generic composite bone	1420 [59]	3260 [59]	105 [59]	0.38 [59]	1700 [175]	0.892 [176]
Cancellous bone	1080 [59]	2198 [177]	117.4 [177]	0.29 [178]	2828 [178]	3.78 [179]
Cortical bone	1990 [59]	3540 long 1770 shear [59, 180]	84 long 127 shear [180]			
Blood					3800 [59]	

Table 2.1 Material properties applied in biothermal models used to validate approximations. The attenuation of the catheter wall was modeled as 43.9 Np/m/MHz [181].

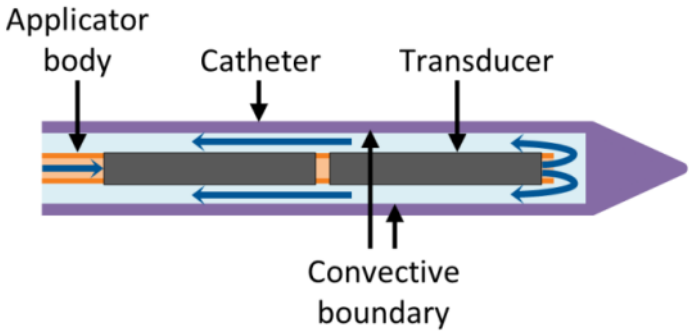

Figure 2.1 Diagram of the ultrasound applicators modeled. Blue arrows indicate the direction of cooling flow, which runs through the center of the applicator, out the tip, and then between the applicator and the catheter. A convective boundary condition is applied to the inner wall of the catheter.

The catheter-cooled ultrasound applicators considered consisted of an array of two cylindrical transducers, each 1.5 mm outer diameter (OD) and 10 mm long (L), sonicating at 6.9-7 MHz from within a plastic implant catheter (2.4 mm OD, 1.89 mm inner diameter (ID)) with integrated water-cooling (Figure 2.1).

Finite element analysis was performed using COMSOL Multiphysics 4.3 with MATLAB to generate transient temperature and thermal dose distributions for various model configurations and to model experimental studies within *ex vivo* tissues and phantoms. Simulations were performed on an Intel Xeon X5680 processor, with 6 cores each operating at 3.33 GHz on a Rad Hat Linux operating system. The catheter was modeled as a 1.89 mm ID and 2.4 mm OD cylinder, with a maximum mesh size of 0.4 mm on its inner surface. The ultrasound source was modeled as two cylinders (1.5 mm OD, 1 cm L) within the catheter. The maximum mesh size on the outermost boundaries of the geometry was 5 mm, and the maximum mesh size on heated bone surfaces was 0.3-1 mm, with finer bone meshes used when the applicator was closer to the bone surface. The mesh size in the soft tissue between the applicator and the bone was limited to a maximum of 0.7-2.5 mm, depending on the distance between the catheter and bone surfaces. Convergence tests were performed to ensure that all mesh sizes on the bone, near the applicator, and on outer boundaries were sufficiently fine for a stable solution. The initial temperature was set to 37°C. An implicit transient solver with a variable time step taken at least once in each 10 second time span was used to solve the transient bioheat equation. The maximum step size for thermal dose calculations was 10-20 seconds. Fixed temperature boundary conditions (equal to the initial temperature) were applied at the outermost boundaries of the geometry. A convective boundary condition was imposed on the inner surface of the catheter, with a heat transfer coefficient h = 1000 W/m^2/°C [182, 183] and flow temperature T_f = 22°C.

$$-\hat{\boldsymbol{n}} \cdot (-k\nabla \mathrm{T}) = h(T_f - T) \tag{2.3}$$

where $\hat{\boldsymbol{n}}$ is the unit vector normal to the boundary.

2.3.2 Acoustic heat deposition in bone

Acoustic heat deposition in tissue, Q (W/m^3), is defined as:

$$Q = -\frac{1}{2}\nabla \cdot Re[\boldsymbol{v} \cdot \boldsymbol{T}^*] \tag{2.4}$$

where $\boldsymbol{v}$ is the velocity vector (m/s), $\boldsymbol{T}$ is the stress tensor (kg/m/s^2), $Re[\ \ ]$ indicates "the real part of," and an asterisk indicates the complex conjugate [114, 184].

$$\boldsymbol{T} = \begin{bmatrix} \boldsymbol{T}_{xx} & \boldsymbol{T}_{xy} & \boldsymbol{T}_{xz} \\ \boldsymbol{T}_{yx} & \boldsymbol{T}_{yy} & \boldsymbol{T}_{yz} \\ \boldsymbol{T}_{zx} & \boldsymbol{T}_{zy} & \boldsymbol{T}_{zz} \end{bmatrix} \tag{2.5}$$

$\boldsymbol{T}_{ii}$, represents longitudinal stress. $\boldsymbol{T}_{ij}$, where $i \neq j$, represents shear stress.

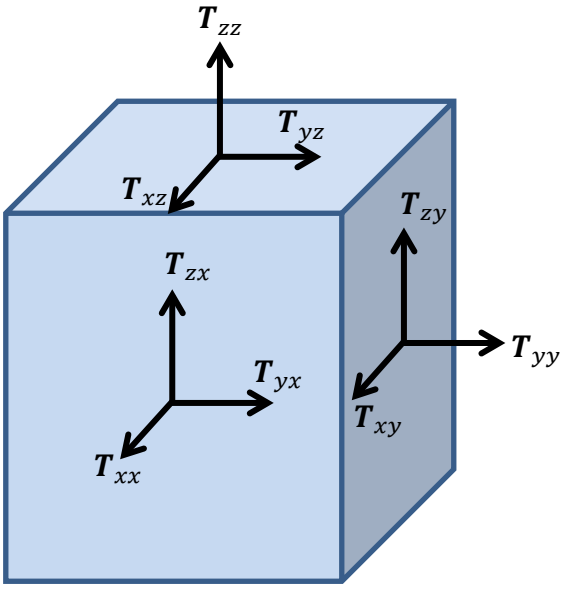

Figure 2.2 Components of the stress tensor showing the longitudinal and shear forces on a volume. Forces on opposite faces are symmetrical; otherwise, the object would be in motion. For example, the upward force on the upper face, $\boldsymbol{T}_{zz}$, is balanced by an equal and opposite downward force on the lower face. The shear force to the right on the front face, $\boldsymbol{T}_{yx}$, is balanced out by an equal and opposite shear force to the left on the back face.

Liquids and soft tissues cannot support shear waves, and longitudinal stresses are uniform on all sides of a small fluid volume dV. Thus, the nine-dimensional tensor can thus be simplified as a one-dimensional hydrostatic pressure, P (kg/m/s^2).

$$\boldsymbol{T}_{fluid} = \begin{bmatrix} \boldsymbol{T}_{xx} & \boldsymbol{T}_{xy} & \boldsymbol{T}_{xz} \\ \boldsymbol{T}_{yx} & \boldsymbol{T}_{yy} & \boldsymbol{T}_{yz} \\ \boldsymbol{T}_{zx} & \boldsymbol{T}_{zy} & \boldsymbol{T}_{zz} \end{bmatrix} = \begin{bmatrix} -P & 0 & 0 \\ 0 & -P & 0 \\ 0 & 0 & -P \end{bmatrix} \quad 2.6$$

$$Q = -\frac{1}{2}\nabla \cdot Re[\boldsymbol{v}P^*] = -\nabla \cdot < \boldsymbol{v}P > = -\nabla \cdot I \quad 2.7$$

where I is intensity and <> indicates an average over time. Attenuation causes the time-averaged intensity of an acoustic beam to decrease exponentially over space:

$$I = I_s e^{-2\alpha x} \quad 2.8$$

where I_s is the intensity on a planar transducer surface (W/m^2), α is the ultrasound absorption coefficient (Np/m), and x is the axis along which a plane wave travels (m).

$$Q = -\nabla \cdot (I_s e^{-2\alpha x}) = -\frac{\partial}{\partial \mathrm{x}}(I_s e^{-2\alpha x}) = 2\alpha(I_s e^{-2\alpha x}) = 2\alpha I \quad 2.9$$

This produces the familiar equation for acoustic heat deposition: $Q = 2\alpha I$.

Unlike liquids and soft tissue, bone and other solids can support shear waves. Thus, the nine-dimensional stress tensor cannot be simplified to a one-dimensional pressure as it can be in soft tissue. This significantly complicates mathematical models of ultrasound propagation in bone.

An approximation is needed to mathematically describe the heating produced by tubular interstitial transducers in bone. Instead of using full wave methods, the acoustic power deposition Q (W/m^3) from cylindrical radiators can be described as a longitudinally collimated and radially diverging intensity pattern (I) [65, 185].

$$Q = 2\alpha I = 2\mathcal{T}\alpha I_s \frac{r_t}{r} e^{-2\int_{r_t}^{r} \mu dr'} \quad 2.10$$

where $\mathcal{T}$ is the acoustic intensity transmission coefficient (unit-less), I_s is the time-averaged acoustic intensity on the transducer surface (W/m^2), r_t is the transducer radius (m), r is the radial distance from the transducer's central axis (m), and μ is the ultrasound attenuation coefficient

(Np/m). In this work, the absorption coefficient α is assumed to be equivalent to the attenuation coefficient, with scattered energy locally absorbed.

When an acoustic wave travelling through soft tissue hits a cortical bone surface, a significant portion of the energy is reflected due to an impedance mismatch. At normal incidence, the remaining energy is transmitted as longitudinal waves. If the incident angle is not normal, some or all of the transmitted energy is converted to shear waves, and both longitudinal and shear transmitted waves are refracted (Figure 2.3).

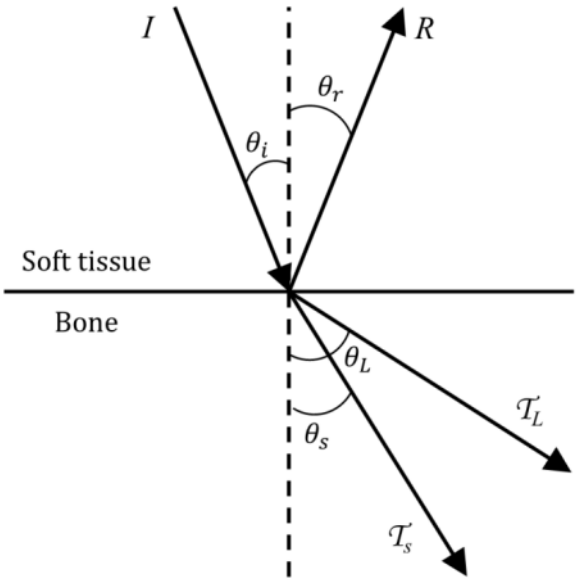

Figure 2.3 Ultrasound reflection and refraction at bone/soft tissue interfaces, as used to derive the models herein. An incident wave strikes the bone surface at angle θ_i and intensity I. The reflected wave, refracted longitudinal wave, and refracted shear wave have intensities R, $\mathcal{T}_L$, and $\mathcal{T}_s$ and travel at angles θ_r, θ_L, and θ_s, respectively.

Defining θ as the angle between the direction in which the wave travels and the normal of the bone surface, the reflection and refraction angles of an acoustic beam incident on bone can be defined by Snell's Law.

$$\theta_r = \theta_i \tag{2.11}$$

$$\theta_L = \begin{cases} \sin^{-1}\left(\frac{v_L \sin(\theta_i)}{v_1}\right), & \theta_i \leq \sin^{-1}\left(\frac{v_1}{v_\mathrm{L}}\right) \\ \frac{\pi}{2}, & \theta_i > \sin^{-1}\left(\frac{v_1}{v_\mathrm{L}}\right) \end{cases} \quad 2.12$$

$$\theta_s = \begin{cases} \sin^{-1}\left(\frac{v_s \sin(\theta_i)}{v_1}\right), & \theta_i \leq \sin^{-1}\left(\frac{v_1}{v_\mathrm{s}}\right) \\ \frac{\pi}{2}, & \theta_i > \sin^{-1}\left(\frac{v_1}{v_\mathrm{s}}\right) \end{cases} \quad 2.13$$

where subscript r refers to the reflected wave, subscript i refers to the incident wave, subscript L refers to the longitudinal wave in bone, subscript s refers to the shear wave in bone, subscript 1 refers to soft tissue, subscript 2 refers to bone, and v is the speed of sound (m/s). The intensity transmission and reflection coefficients as an acoustic wave travels from soft tissue into bone are defined [186] as:

$$R \equiv \frac{I_r}{I_i} = \left|\frac{Z_L\cos^2(2\theta_s) + Z_s\sin^2(2\theta_s) - Z_1}{Z_L\cos^2(2\theta_s) + Z_s\sin^2(2\theta_s) + Z_1}\right|^2 \quad 2.14$$

$$\mathcal{T}_L \equiv \frac{I_L}{I_i} = \frac{\rho_2 \tan\theta_i}{\rho_1 \tan\theta_L}\left|\frac{2\rho_1 Z_L\cos(2\theta_s)}{\rho_2(Z_L\cos^2(2\theta_s) + Z_s\sin^2(2\theta_s) + Z_1)}\right|^2 \quad 2.15$$

$$\mathcal{T}_s \equiv \frac{I_s}{I_i} = \frac{\rho_2 \tan\theta_i}{\rho_1 \tan\theta_s}\left|\frac{2\rho_1 Z_s\sin(2\theta_s)}{\rho_2(Z_L\cos^2(2\theta_s) + Z_s\sin^2(2\theta_s) + Z_1)}\right|^2 \quad 2.16$$

$$Z_1 = \frac{\rho_1 v_1}{\cos\theta_i} \quad 2.17$$

$$Z_L = \frac{\rho_2 v_L}{\cos\theta_L} \quad 2.18$$

$$Z_s = \frac{\rho_2 v_s}{\cos\theta_s} \quad 2.19$$

where R is the reflection coefficient, $\mathcal{T}$ is the transmission coefficient, and I is intensity (W/m^2).

In contrast to ultrasound incident on cortical bone, specular reflection and transmission cannot be assumed in cases when cancellous bone is in direct contact with an osteolytic tumor

without a smooth cortical shell between the bone surface and the transducer. Cancellous bone consists of a sponge-like trabecular bone structure with marrow filling the interstitial spaces. The incidence angle on the individual trabeculae is different from the incidence angle on the bulk tissue as a whole. Thus, we assume that 10% of the energy incident on cancellous bone is reflected and 90% is transmitted and locally absorbed, regardless of incidence angle [177, 187].

Model	**A: Angle-dependent volumetric**	**B: Constant transmission volumetric**	**C: Angle dependent boundary**	**D: Constant transmission boundary**
Bone heat source	Volume	Volume	Surface	Surface
Transmission coefficient	Angle-dependent	Constant	Angle-dependent	Constant
Shear mode conversion	Yes	No	Yes	No
Reflection	Yes	No	No	No
Refraction	Yes	No	No	No

Table 2.2 Summary of the four types of models.

In order to determine what approximations can accurately represent interstitial ultrasound heating at a bone/soft tissue interface, a series of models of decreasing complexity were developed (summarized in Table 2.2). These simplified models were devised to investigate the relative impacts of reflection, refraction, mode conversion, and heating throughout the bone volume on predicted temperatures and on thermal lesion sizes.

2.3.3 Model A - Angle-dependent volumetric

The angle-dependent volumetric model, Model A, considers reflection, refraction, and shear mode conversion at cortical bone interfaces. To describe heating within and adjacent to bone, the equations describing acoustic power deposition were multiplied by the appropriate transmission and reflection coefficients, as in Moros et al. and Lin et al. [161, 173]:

$$Q_1^A = Q_{1,i} + Q_{1,r} = 2\alpha I_s \frac{r_t}{r} e^{-2\int_{r_t}^{r} \mu dr'} + 2R\alpha I_s \frac{r_t}{r_r} e^{-2\int_{r_t}^{r_r} \mu dr'} \quad 2.20$$

$$Q_2^A = Q_{2,L}^A + Q_{2,s}^A = 2\mathcal{T}_L \alpha_L I_s \frac{r_t}{r} e^{-2(\int_{r_t}^{r_1} \mu dr' + \int_{r_1}^{r} \mu_L dr')} + 2\mathcal{T}_s \alpha_s I_s \frac{r_t}{r} e^{-2(\int_{r_t}^{r_1} \mu dr' + \int_{r_1}^{r} \mu_s dr')} \quad 2.21$$

where $r_r - r_t$ is the distance the reflected wave travels through soft tissue from the surface of the transducer and r_1 is the radial distance from the transducer center to the point where the wave crosses the bone surface. Q_1^A, the heat deposition in soft tissue in Model A, contains contributions from the incident and reflected waves. Q_2^A, the heat deposition in bone in Model A, contains contributions from the longitudinal and shear waves.

2.3.4 Model B - Constant transmission volumetric

In Model B, the constant transmission volumetric model, a constant attenuation coefficient and a constant transmission coefficient, both independent of incident angle, were used in bone. Reflection and refraction were not considered. Transmitted energy is assumed to be absorbed so close to the bone surface that refraction has little effect, and the heating contributions of reflected energy are assumed to be insignificant compared to heating from the incident waves and conduction from the highly absorbing bone. The transmission coefficient ($\mathcal{T}_I$) is calculated for normal incidence on a bone. Here,

$$\mathcal{T}_I \equiv \frac{I_2}{I_i} = \frac{4\rho_1 v_1 \rho_2 v_2}{(\rho_1 v_1 + \rho_2 v_2)^2} = 77.3\% \quad 2.22$$

$$Q_1^B = Q_{1,i} = 2\alpha I_s \frac{r_t}{r} e^{-2\int_{r_t}^{r} \mu dr'} \quad 2.23$$

$$Q_2^B = 2\mathcal{T}_I \alpha I_s \frac{r_t}{r} e^{-2\int_{r_t}^{r} \mu dr'} \quad 2.24$$

2.3.5 Model C - Angle-dependent boundary and Model D - Constant transmission boundary

Models C and D are based upon similar equations as Models A and B, respectively, but all energy is assumed to be absorbed at the bone surface without penetration into the bone. Instead of volumetric power deposition within bone, bone heating is modeled as an energy (q) applied to the bone surface as a power flux (W/m^2) equal to the intensity on the bone surface multiplied by a transmission coefficient. The assumption is that all transmitted energy (shear and longitudinal) is absorbed within such close proximity to the bone surface that the energy may be approximated as absorbed on the bone surface. Reflection was not considered and refraction is not applicable, as this approximation assumes that the energy does not penetrate any distance into the bone.

$$q = -\vec{n} \cdot (-k\nabla \mathrm{T}) \tag{2.25}$$

$$Q_1^C = Q_1^D = Q_{1,i} = 2\alpha I_s \frac{r_t}{r} e^{-2\int_{r_t}^{r} \mu dr'} \tag{2.26}$$

$$q_2^C = (\mathcal{T}_L \cos\theta_L + \mathcal{T}_s \cos\theta_s) I_s \frac{r_t}{r} e^{-2\int_{r_t}^{r_1} \mu dr'} \tag{2.27}$$

$$q_2^D = \mathcal{T}_I \cos\theta_2 \, I_s \frac{r_t}{r} e^{-2\int_{r_t}^{r_1} \mu dr'} \tag{2.28}$$

$\vec{n}$ is the unit vector normal to the bone surface. The cosine terms in Equations 2.27 - 2.28 define the normal component of the energy flux through the bone surface. The transmitted angle in Model D (θ_2) is the same as the incidence angle (θ_i).

The transmission and reflection coefficients in the angle-dependent models, A and C, require separate shear and longitudinal components, so these two models are calculated using the acoustic properties of cortical bone. All other properties for Models A-D are those of whole composite bones.

2.3.6 Comparison of models in perfused tissue

The four models were first compared in simulations of perfused tissues, with an initial temperature of 37 °C. The applicator was positioned in a block of muscle with its axis parallel to a flat bone 10 or 20 mm away from it, as in Figure 2.4. A 6.9 MHz applicator, with two transducers sectored longitudinally to produce acoustic energy in a 180° angular expanse and powered at 9.4 acoustic W/cm^2, was modeled. The initial temperature was set to 37°. For each model, identical transient solvers (geometric multigrid) and meshing parameters were used.

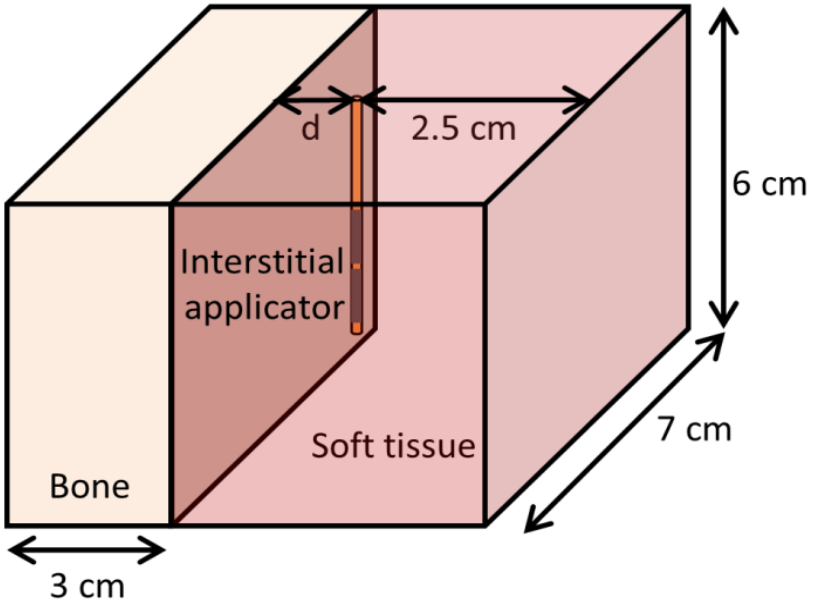

Figure 2.4 Geometry used to model interstitial ultrasound ablation with the applicator at various distances (0.5 cm ≤ d ≤ 3.2 cm) from the surface of a flat bone.

2.3.7 Parametric investigations

To investigate these models and the effects of varying tumor properties, a 7 MHz applicator with a 135° active acoustic zone and 2 cylindrical transducers was modeled in soft tissue next to a plane of composite bone, as in Figure 2.4. The largest tumor size that could be ablated within 10 minutes for various tumor attenuation coefficients and perfusion rates was determined. The

tumor attenuation was varied from 3 to 15 Np/m/MHz, representing a range of soft tissue neoplasms [59]. Tumor perfusion was varied from 0 to 13 kg/m^3/s, representing zero perfusion in necrotic tumors to the high perfusion observed in some tumors [188, 189]. All other tumor properties were set to those of muscle. The target was considered fully ablated when 99% of the area between the catheter and the bone surface, ranging from 1 mm below the upper transducer's upper edge to 1 mm above the lower transducer's lower edge, exceeded 240 EM43°C, which is considered a lethal thermal dose [33]. A proportional integral controller (k_p = 0.2, k_i = 0.0017) was implemented to modulate the power supplied to the transducers (limited to a range of 0-21.2 W/cm^2 acoustic) in order to approach and maintain a peak temperature of 85°C. 10 minute ablations using the constant transmission volumetric model were simulated. For low and high attenuations, Models A, C, and D were also applied.

2.4 Results

2.4.1 Comparison of models in perfused tissue

The ultrasound heat deposition in bone and soft tissue was calculated using Models A-D (Figure 2.5). Figure 2.6 shows the temperature maps predicted by Model B and the 240 EM43°C contours, which correspond to ablated regions, for the four models when the applicator is placed in perfused muscle at distances of 1 and 2 cm from a flat bone surface. The approximations in Models B and D produced thermal dose contours that closely matched the more comprehensive Model A. However, when the applicator was close enough to ablate the bone surface, Model C produced 240 EM43°C contours that did not extend as deeply (5.0 mm) into the bones as the other three (5.3-5.8 mm). The boundary models (C and D) had significantly shorter computation times than the volumetric models (A and B). Model D was solved 3.6, 2.6, and 1.5 times faster

than Models A, B, and C, respectively, when the applicator was 1 cm from bone. It took 218, 156, 89, and 60 minutes, respectively, to compute ten-minute transient simulations using Models A-D on an Intel Xeon X5680 processor. In these cases, Models C and D had a mesh size of 0.8 mm on the heated portion of the bone surface and 332,741 elements total, while Models A and B, which required a finer bone mesh, had a mesh size of 0.5 mm on heated bone surfaces and 540,505 elements total.

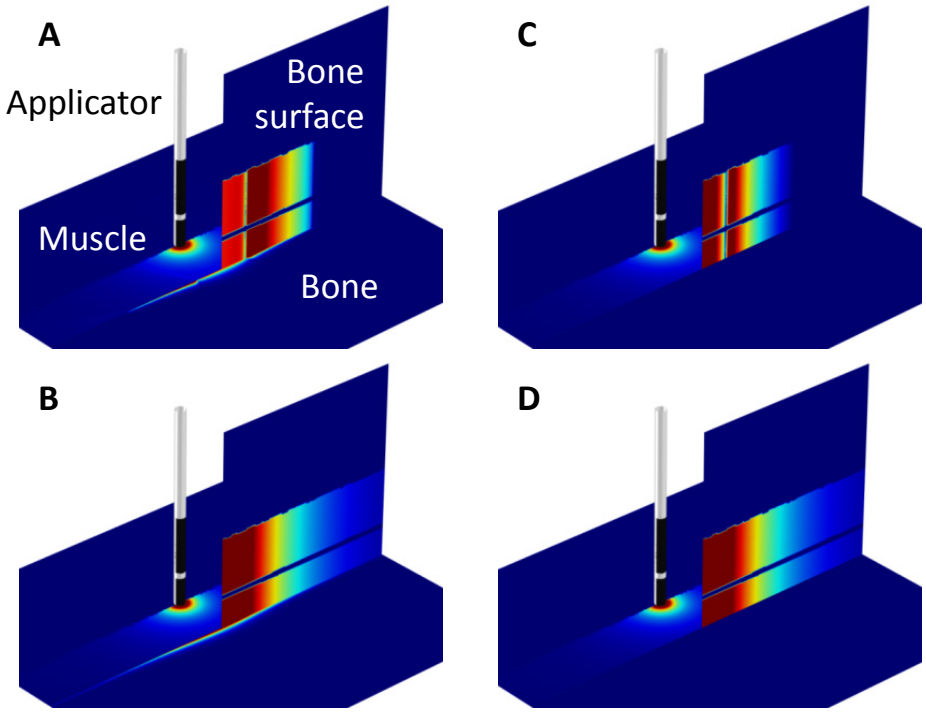

Figure 2.5 Color map of heat deposition Q in tissue according to Models A-D. A 180° applicator was placed in muscle and the acoustic output was directed towards the bone surface. Models A and B consider transmission into the bone volume, while C and D do not. Models A and C employ a transmission coefficient dependent on incident angle, while Models B and D use a constant transmission coefficient.

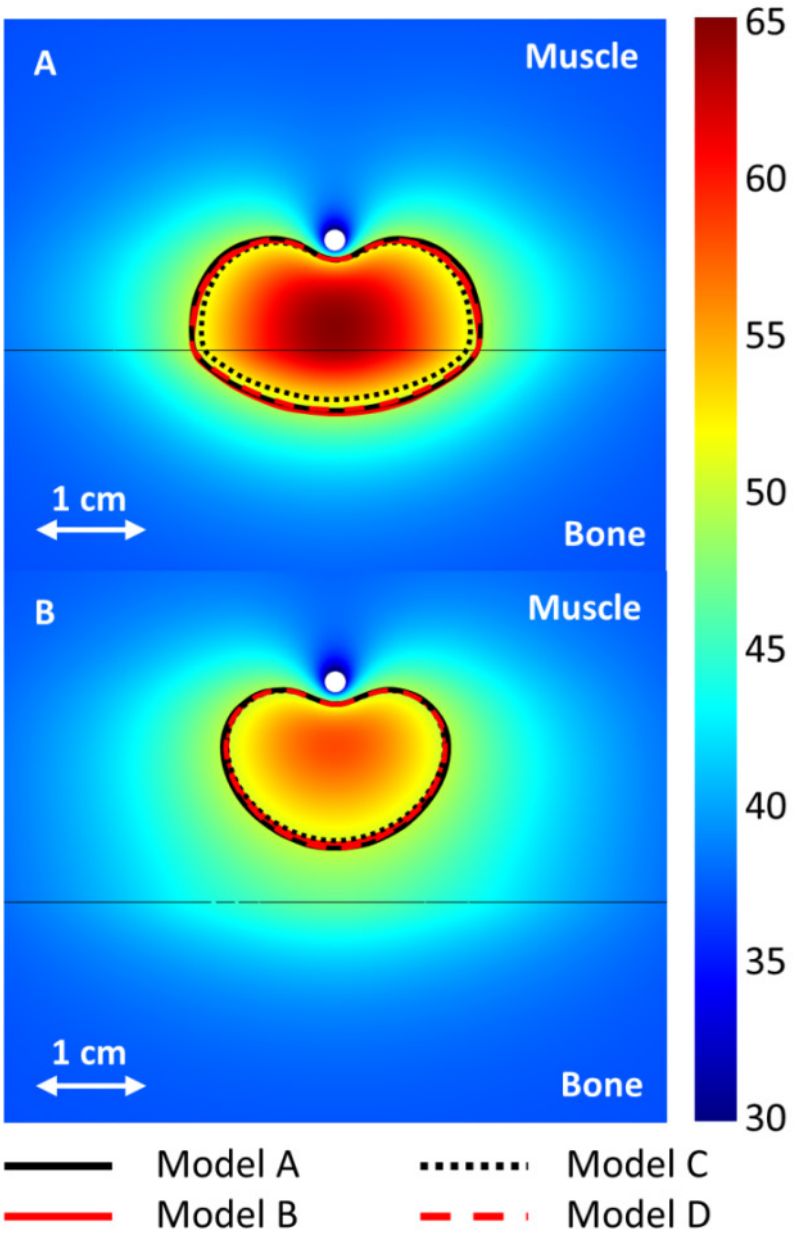

Figure 2.6 240 EM43°C contours calculated with Models A-D after a 10 minute ablation are shown in the central plane between the two transducers. The applicators (white circle) are placed 1 and 2 cm from a flat bone (black line) in A and B, respectively. A color map shows the temperatures (°C) calculated with the constant transmission volumetric model (Model B).

2.4.2 Parametric investigations

A parametric study was performed to investigate the influence of attenuation and perfusion on the volume of tissue that could be ablated in the presence of bone and to determine how the models perform in tissues with various properties. The maximum distance between the

applicator and a flat bone at which all tissue between the two could be ablated is shown in Figure 2.7 for various soft tissue perfusions and attenuations. The maximum tumor size that could be ablated with zero perfusion in soft tissue without bone present is also shown.

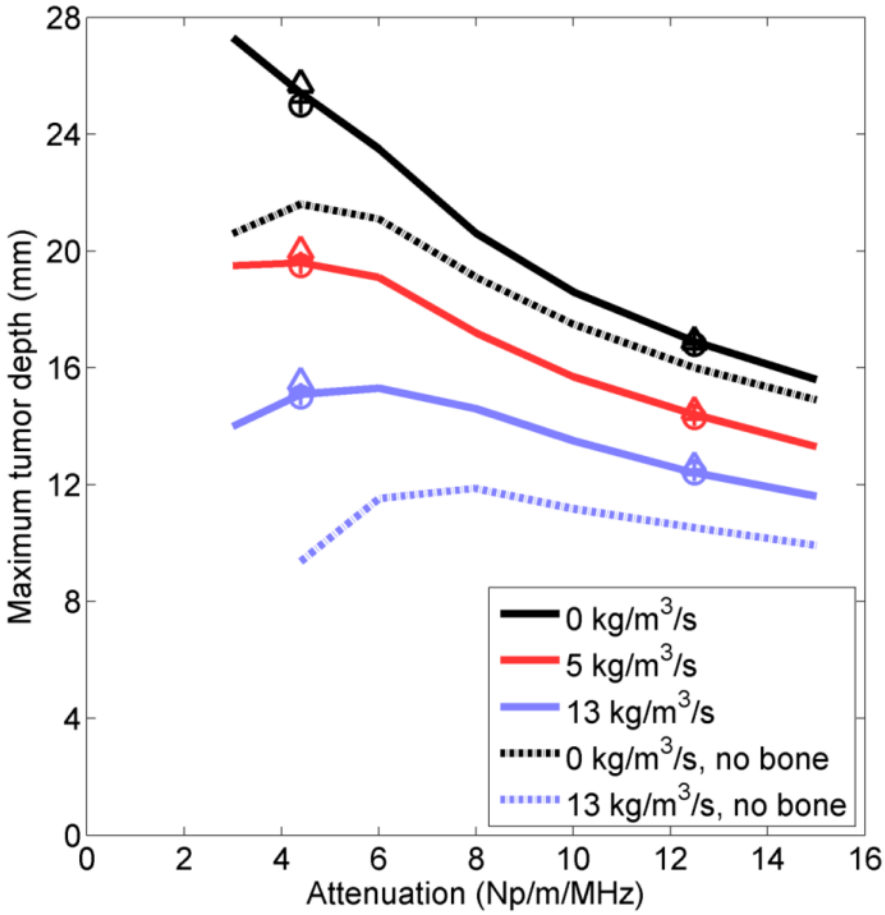

Figure 2.7 The maximum distance between an applicator and a flat bone at which all tumor tissue between the two can be ablated within 10 minutes, given various ultrasound attenuations and blood perfusion rates in the tumor, as calculated by Model B. The maximum radius that can be fully ablated when bone is absent is also shown for 0 and 13 kg/m^3/s perfusion in the tumor. The maximum distance between an applicator and bone for which all intervening tissue can be ablated is also plotted for models A (+), C (○), and D (Δ) for attenuations of 4 and 12.5 Np/m/MHz and perfusions of 0 (black), 5 (red), and 13 (blue) kg/m^3/s.

Significantly larger tumors could be ablated when bone was present at the outer boundary, especially when the tumor attenuation was low. The largest tumors that could be ablated with bone present had low attenuations and perfusions, though there was a falloff in the

volume that could be ablated at the lowest attenuations. At a relatively high perfusion of 13 $kg/m^3/s$ and exceptionally low attenuation (3 Np/m/MHz), the combined effects of perfusion, low absorption, and catheter cooling for the parameters tested herein resulted in reduced heating in the tissue immediately adjacent to the applicator, so it could not be ablated within 10 minutes at the maximum allowable power unless bone was present. In practice, the cooling flow could be applied at a higher temperature or turned off immediately after power application to effectively coagulate tissue adjacent to the applicator. The four models agreed well on the radii of the ablated volumes, regardless of the tumor attenuation or perfusion, with better agreement at high attenuations. The discrepancy between the calculations made by Model A and the calculations made by the other models of the maximum distance between the bone and applicator at which all intervening tissue could be ablated was less than 2.6% for all cases evaluated.

2.5 Discussion

Bone has an acoustic absorption coefficient 1-2 orders of magnitude higher than that of soft tissue [59], resulting in preferential heating at bone surfaces [115, 157]. Furthermore, acoustic impedance differences between bone and soft tissue soft tissue result in reflection, refraction, and mode conversion at the interface, which complicate wave propagation and prediction of resultant heating patterns. Complex accurate acoustic modeling of this interface is computationally intensive and difficult, especially considering that the stress tensor in solids cannot be simplified as a one dimensional pressure as it can be in liquids. In this work, we have devised approximate models of the interactions of interstitial ultrasound with bone. Comparative theoretical studies indicate that omission of reflection, refraction, shear mode conversion, and acoustic penetration into bone from FEM models may not result in any significant loss in accuracy.

Models using four methods (A-D) of decreasing complexity to calculate heat deposition in bone were developed and compared. Models B and D produced temperature and thermal dose distributions very similar to the more comprehensive Model A (Figure 2.6 - Figure 2.7), demonstrating that neither angle-dependent nor volumetric heat sources are crucial to modeling high-frequency interstitial ultrasound heating in bone. Any discrepancies between the four models generally occurred near the most heated portions of the bone surface and were lower at earlier time points. Model C, which included angle-dependent transmission but excluded reflection, produced somewhat lower temperature and thermal dose distributions than the other models.

At 7 MHz, 69% (longitudinal) to 83% (shear) of the acoustic energy entering bone is attenuated and absorbed within 1 mm, and 97% (longitudinal) to 99.5% (shear) is absorbed within 3 mm. Shear and longitudinal penetration beyond 3 mm is negligible. Unless the bone is very thin, the amount of energy that exits the bone to propagate through soft tissue, which is further decreased by the transmission coefficient, is negligible and does not need to be modeled. Thus, the high attenuation coefficient of bone allows for so little acoustic penetration that the different pathways of shear and longitudinal waves do not need to be modeled separately, and heating can be approximated as occurring on the face of the bone surface.

2.6 Conclusion

Comparative simulations show that approximations of acoustic heat deposition in bone at 7 MHz excluding reflection, refraction, shear mode conversion, and penetration into the bone volume result in relatively small losses in accuracy. Simulations indicate that the use of these approximations generates smaller errors when the applicator is placed in mediums with higher

attenuation coefficients. These approximations may be useful for modeling interstitial ultrasound ablation involving bone with less complexity and computation time than more comprehensive models.

Chapter 3

Experimental validation of techniques for modeling interstitial ultrasound ablation involving bone

3.1 Abstract

Purpose: The objectives of this study were to evaluate and validate the performance of numerical models of interstitial ultrasound ablation of tumors within or adjacent to bone through comparison to experiments, and to investigate the effect of bone on the temperature and thermal dose distributions produced during interstitial ultrasound ablation.

Methods: Experiments within e*x vivo* tissues, *in vivo* tissues, and phantoms were performed with the applicator placed both directly into bone and in soft tissue at several distances from bone. Temperature distributions were measured using needle thermocouples or MR temperature imaging (MRTI). Finite element meshes were created using both simple geometrical

representations of tissues, and including complex anatomical representations based on segmented MR images. Models using four different approximations of 7 MHz ultrasound propagation at bone/soft tissue interfaces were developed based on experimental setups and were evaluated through comparison to experimental data.

Results: High ultrasound absorption at bone/soft tissue interfaces increased the volumes of target tissue that could be ablated. Models using simplified approximations produced temperature profiles closely matching both more comprehensive models and experimental results, with good agreement between 3D calculations and MRTI. The correlation coefficients between simulated and measured temperature profiles in phantoms ranged from 0.852 to 0.967 (p-value < 0.01) for the four models.

Conclusions: Models using approximations of interstitial ultrasound energy deposition around bone/soft tissue interfaces produced temperature distributions in close agreement with comprehensive simulations and experimental measurements. These models may be applied to predict temperatures produced during interstitial ultrasound ablation involving bone, with applications toward treatment planning.

A large portion of the work in this chapter has been published by Scott et al. ("Approaches for modeling interstitial ultrasound ablation of tumors within or adjacent to bone: Theoretical and experimental evaluations," 2013) [170].

3.2 Introduction

Interstitial ultrasound ablation is a treatment modality with directional control that produces high temperature peaks on bone surfaces. Bone surfaces sonicated with ultrasound experience preferential heating because bone has such a high ultrasound absorption coefficient that ~97-

99.5% of all transmitted energy is absorbed over the first three millimeters. Interstitial ultrasound ablation could potentially take advantage of preferential bone heating to ensure that the boundaries of tumors adjacent to bone are heated and to attain quick and thorough ablations.

In Chapter 2, techniques for developing 3D transient finite element models of interstitial ultrasound ablation through bone were developed. The objectives of this study are to experimentally validate the various models of interstitial ultrasound heating of bone and to experimentally investigate the impact of bone on ablation performance. Thermocouple and MR-based thermometry are used in *ex vivo, in vivo,* and phantom experiments to obtain transient temperature distributions for comparison with numerical predictions. The theoretical models considered in this study provide quantitative assessment of interstitial ultrasound ablation of tumors in and near bone, and can be applied to treatment planning.

3.3 Materials and Methods

3.3.1 Interstitial ultrasound applicators

Catheter-cooled applicators were either placed directly into bone or into phantoms or soft tissue with their active sectors directed towards bone. The applicators contained two 1.5 mm OD 135-180° sectored tubular transducers sonicating at 6.9-7.5 MHz, and were operated from within a water-cooled Celcon catheter (2.4 mm OD, 0.25 mm wall thickness). 6.5 and 4.2 MHz planar applicators were also considered, each with one transducer (10.1 x 2.2 mm and 8.5 x 2.0 mm, respectively) with efficiencies of 39.3% and 34.6%, respectively, mounted on a polyimide body (2.0 mm OD). The planar applicators were operated from within a water-cooled polyimide catheter (ID = 2.8 mm, wall thickness = 0.0508 mm).

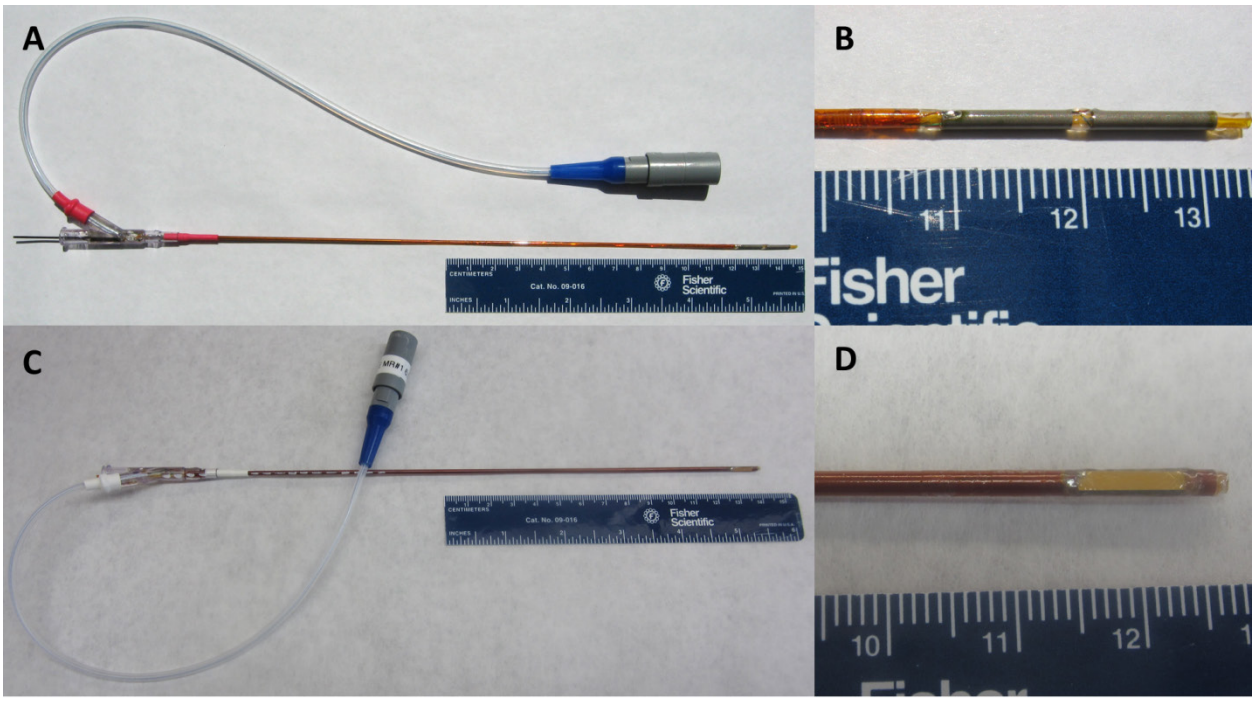

Figure 3.1 Examples of interstitial ultrasound applicators with tubular (A-B) and planar (C-D) transducers. The full applicators are shown in A and C, and the transducers at the tips are shown in B (gray) and D (gold).

3.3.2 Finite element analysis of heat transfer

To model interstitial ultrasound ablation of *ex vivo* bone and soft tissues, 3D finite-element models were created based on the Pennes bioheat transfer equation (Equation 2.1). Biothermal and acoustic finite element models were created using COMSOL Multiphysics 4.3 in conjunction with MATLAB. Initial simulation temperatures were set to 22°C or 37°C, depending on whether the simulation was performed to model bench-top or physiological conditions. Unless otherwise specified, all methodologies, equations, applicator specifications, mesh sizes, and modeling platforms employed are detailed in Chapter 2.

Models using four approximations of varying comprehensiveness to describe ultrasound propagation and absorption in bone and soft tissue were considered (Table 2.2). Model A (Equations 2.20-2.21), considered reflection, refraction, and shear mode conversion as a function

of incident angle. Model B, equations 2.22-2.24, ignored reflection, refraction, and shear mode conversion, assuming a constant transmission coefficient into bone. Models C and D, Equations 2.26-2.28, were similar to Models A and B, respectively, but instead of considering ultrasound absorption throughout a bone volume, all acoustic energy reaching the bone surface was assumed to be absorbed on the interface. These four models are described in more detail in Sections 2.3.3-2.3.5 of Chapter 2.

Medium	**Density (kg/m^3)**	**Velocity (m/s)**	**Attenuation (Np/m/MHz)**	**Thermal conductivity (W/m/°C)**	**Specific heat (J/kg/°C)**	**Perfusion rate ($kg/m^3/s$)**
Muscle	1041 [59]	1576 [59]	5* [130]	0.5 [59]	3430 [59]	0.692 [59]
Generic composite bone	1420 [59]	3260 [59]	105 [59]	0.38 [59]	1700 [175]	0.892 [176]
Cancellous bone	1080 [59]	2198 [177]	117.4 [177]	0.29 [178]	2828 [178]	
Cortical bone	1990 [59]	3540 long 1770 shear [59, 180]	84 long 127 shear [180]			
Medullary cavity	980 [59]	1460** [59]	See equation 3.1	0.25** [59]	2500** [59]	
Phantom	1030 [190]	1602 [190]	5.6 [190]	0.59 [190]	4900 [190]	
Blood					3800 [59]	

Table 3.1 Material properties applied in biothermal models used to validate approximations. The attenuation of the Celcon catheter wall used with tubular transducers was modeled as 43.9 Np/m/MHz [181]. Based upon measured values, the polyimide catheter used with planar transducers was modeled with an ultrasound attenuation coefficient of 600 Np/m/MHz.
*In *ex vivo* experiments performed at physiological temperatures, muscle attenuation was assumed to linearly increase from 4.4 Np/m/MHz at 49.2°C to 6.6 Np/m/MHz at 65°C [130].
**Material properties of fat were applied for some medullary cavity properties.

The material properties of the *ex vivo* tissues simulated in this study are given in Table 3.1. Perfusion was assumed to be 0 $kg/m^3/s$ in models of bench-top experiments. The

temperature-dependence of muscle attenuation was considered only when modeling *ex vivo* experiments performed at physiological temperatures. Otherwise, muscle attenuation was set to 5 Np/m/MHz.

3.3.3 Thermal lesions: *Ex vivo* bone and tissue studies

A bench-top experimental setup, including *ex vivo* porcine loin muscle and bovine bones (store bought), was developed to investigate the impact of bone on thermal ablation with interstitial ultrasound (Figure 3.2). Bovine rib and cervical vertebrae were cleaned of soft tissue, and the vertebrae were sectioned to produce a flat slab of cancellous. The bones and porcine loin muscle were degassed, allowed to equilibrate to 37°C in a water bath, and positioned adjacent to one another in a plastic template in the bath. A catheter-cooled 6.9 MHz ultrasound applicator with two 135° tubular transducers was inserted through the template into the muscle 5-35 mm away from and parallel to an adjacent bone surface. Acoustic energy (output intensity = 11.1, 12.5, or 22.2 W/cm^2) was delivered for a 10 minute ablation. 18 ablations incorporating rib bones and 11 ablations incorporating vertebral bones were performed, with a separate portion of the muscle and bone tissues heated in each trial. The soft tissue was then cut through the center of the ablation zone and the dimensions of gross tissue discoloration (coagulation) were measured.

Simulations of three trials with the tissue heated at 12.5 acoustic W/cm^2 were performed using Models A-D, the geometry of Figure 2.4, and parameters mimicking experimental conditions with the applicator positioned 15, 20, and 32 mm away from the bone. The simulated size and shape of thermal lesions, defined as cross-sectional area of the 52°C contour [191], were compared to the lesions measured in tissue.

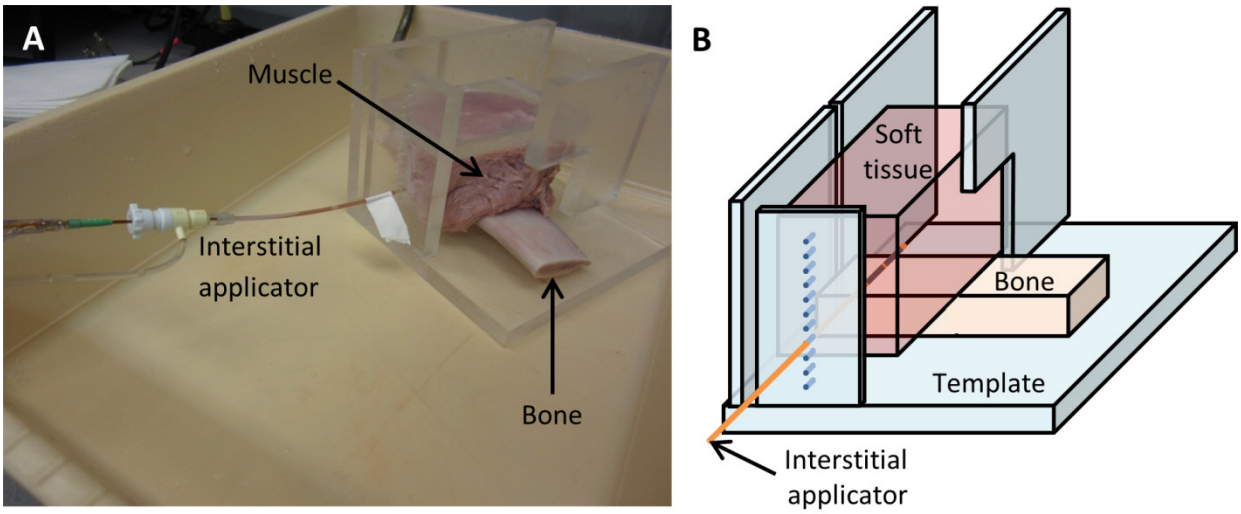

Figure 3.2 Setup of bench-top experiments with *ex vivo* muscle and bone, shown without water bath for clarity. A cut of porcine muscle was placed on top of bovine bone and heated with interstitial ultrasound.
Phantom studies with invasive thermometry

To quantify the temperatures attained during interstitial ultrasound ablation involving bone, experiments were performed in soft tissue equivalent gel phantoms with embedded bones. Store bought bovine rib (representing cortical bone) and bovine cervical vertebrae were boiled and cleaned of soft tissue. The vertebrae were sectioned to produce a flat slab of cancellous bone, and all bones were degassed under a vacuum. Two 22 G needles were inserted into holes predrilled through the bones, holding them with their flat surfaces upright. A tissue-mimicking gel phantom designed for ultrasound ablation was poured around the bones and allowed to solidify. The phantom, which has stable acoustic, thermal, and MR properties that are similar to tissue, consists of a gellan gum hydrogel containing aluminum oxide particles [190]. A multi-junction thermocouple (5 junctions, spaced every 5 mm) was placed inside one of the needles to measure the temperature in the phantom and the bone. An interstitial ultrasound applicator (6.9-7.3 MHz, 135°, tubular transducers) within a catheter was inserted through a template into the phantom 30 mm in front of the bone, with the center of one transducer adjacent to the thermocouple (Figure 3.3). At 5 and 10 minutes into the heating, the thermocouple was

repositioned in increments within the needle to 6-8 locations to record a detailed temperature profile at up to 40 points spaced 0-5 mm apart. After the phantom cooled to ambient temperatures, the whole process was repeated to measure temperature profiles with the center of the applicator 25, 20, 15, 10, and 5 mm from the bone surface, in that order. Temperature profiles at each applicator location were obtained in 3-4 phantoms with an embedded rib bone and in 3-4 phantoms with an embedded vertebral bone, for 40 ablation experiments total.

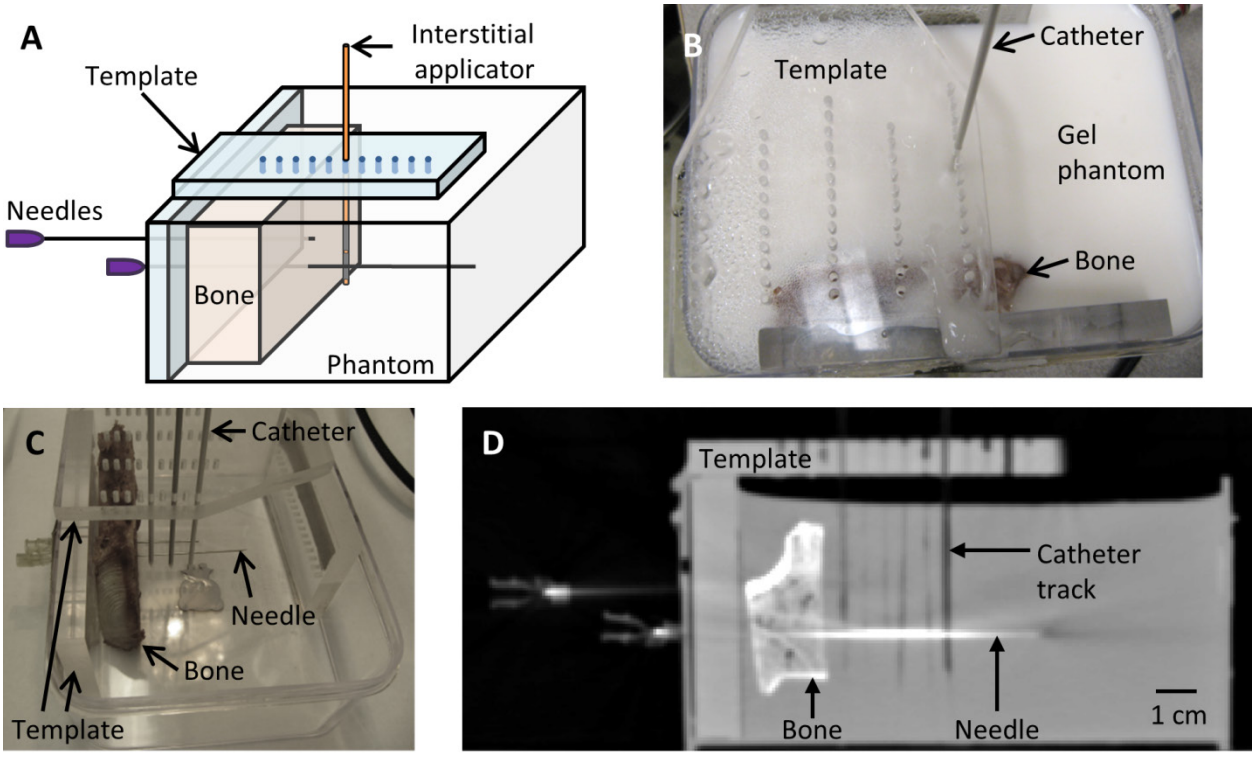

Figure 3.3 Setup of *ex vivo* bone and phantom experiments. The temperature rise in a phantom with an encapsulated bone was measured by thermocouples within needles. (A) Diagram of experimental setup. Photos of the setup after (B) and before (C) the phantom was poured are shown. (D) CT scan of a phantom with encapsulated cancellous bone after ablation was performed with the applicator 6 distances from the bone. The catheter was inserted at one position at a time, starting far from the bone and moving progressively closer in 5 mm increments after each ablation.

The heating of the phantoms was simulated using the geometry in Figure 2.4, with sonication of 135° active sectors at 6.9 MHz and 16.6 acoustic W/cm^2. The ribs were modeled

as composite bone, and the cervical vertebral bones as cancellous bone. Simulated and experimental temperature profiles were compared.

3.3.4 MRTI of *ex vivo* bone and soft tissue

Bovine rib and vertebrae with surrounding soft tissues (store bought) were heated with interstitial ultrasound and monitored with MR temperature imaging (n=2). The *ex vivo* tissues, previously degassed and equilibrated to room temperature, were placed inside a birdcage transmit/receive head coil in a 3T MR scanner (GE Healthcare, Waukesha, WI). A 7.45 MHz MR-compatible interstitial ultrasound applicator with 180° active acoustic tubular sectors was inserted into muscle, 5-10 mm from the irregular cortical bone surfaces, with the active sectors facing the bones. The tissues were heated with applied intensities of 9.1-10.2 acoustic W/cm^2 to each transducer segment for 10 minutes. MRTI was performed during heating, using a 2D fast spoiled gradient echo sequence with TE = 8 ms, TR = 120 ms, flip angle = 30°, and field of view = 12x12 cm^2 (rib) or 14x14 cm^2 (vertebra) in eight slices that were 5 mm thick and perpendicular to the applicator axis. The shift in the proton resonance frequency (PRF) of water, via phase mapping, was used to calculate temperature [123]. As commonly applied with this approach, phase unwrapping of the complex MR signal was performed to correct jumps in the phase changes from $-\pi$ to π [192].

3D models of the *ex vivo* rib and vertebrae ablations monitored with MRTI were developed. The Mimics Innovation Suite (Materialise NV, Leuven, Belguim) was used to manually segment MR images acquired before each ablation and to create finite element method (FEM) meshes specific to the tissue geometry. To create FEM meshes, the segmented 3D images were converted to 3D objects represented by triangular surface meshes and smoothed. A cylinder with a diameter of 1.89 mm was added to the geometry to represent the cooled inner

surface of the catheter. All the surface meshes were refined to lie within the size ranges used in this study (0.3-5 mm, with finer meshes where more acoustic energy is deposited), and combined into a single surface mesh of the volume. The surface mesh was then converted to a volume mesh and imported into Comsol.

The spatial distribution of heat deposition in tissue (Q) was calculated in MATLAB and imported into Comsol. First, the ultrasound attenuation coefficients throughout the volume, as defined in Comsol, were imported into MATLAB. MATLAB was then used to integrate the acoustic attenuation over a fine spatial resolution, to calculate the transmission coefficients, and to determine the acoustic heat deposition on the finite element grid. The calculation of heat deposition in the bone is described in further detail in Appendix A. In contrast, heat deposition in volumes composed of rectangular prisms to model tissue and cylinders to model ultrasound applicators (Figure 2.4) was calculated analytically within Comsol. Meshes representing such volumes were also developed within Comsol. Because tissue surfaces relatively close to the heated region were exposed to air in the cases monitored with MRTI, a heat flux with h = 10.5 W/m/°C [193, 194] and T_f = 22°C was applied on the outer boundaries (Equation 2.3). Due to the complexity of tracing the paths of reflected and refracted rays through the irregular geometries of bone/muscle interfaces as required for Model A, these two cases were modeled using Models B-D.

3.3.5 MRTI of *in vivo* bone and soft tissue

An *in vivo* study of the influence of bone on ablation was performed and applied to validate numerical models. This study was performed in a subject also used in an acute prostate ablation study. An MR-compatible interstitial ultrasound applicator with two sectored 180° tubular transducers was placed in a canine thigh 13-28 mm from the curved surface of the bone. 7.5

MHz ultrasound was directed towards the bone. The tissue was heated at 17.1 and 9.0 acoustic W/cm^2 by the tip and second transducers, respectively, for 10 minutes. PRF-based phase mapping was used to measure temperature throughout heating (TE = 8 ms, TR = 35 ms, flip angle = 10°, FOV = 15x15 cm^2, slice thickness = 5 mm). Imaging was performed using an endorectal coil.

3D biothermal and acoustic simulations of this experiment were performed, based on segmented MR images and using the techniques described in Section 3.3.4 and Appendix A. A 15° acoustic dead zone was assumed on each side of the active transducer sector [195]. Models B-D were applied. All three models considered perfusion, which was assumed to reduce to zero at a thermal dose of 300 EM43°C due to heating-induced microvascular stasis. *In vivo* bones were modeled as composite bone. The temperature profiles calculated by these models were compared to those measured experimentally.

3.3.6 MRTI and invasive thermometry in *ex vivo* cortical bone

To study the effects of thick cortical bone on interstitial ultrasound ablation, heating was performed with an applicator inserted into the medullary cavity of an *ex vivo* bovine femur, parallel to the length of the bone and 8.5 mm from the bone surface (Figure 3.4). Separate bone segments purchased from Animal Technologies (Tyler, TX) were used in each of two experiments. An MR-compatible interstitial ultrasound applicator with two 180° 7.8 and 7.6 MHz sectored tubular transducers was fabricated for use in this and the following MR studies. The applicator was placed within the medullary cavity with the transducers centered along the bone's length, and with the directional acoustic output directed towards the cortical shell.

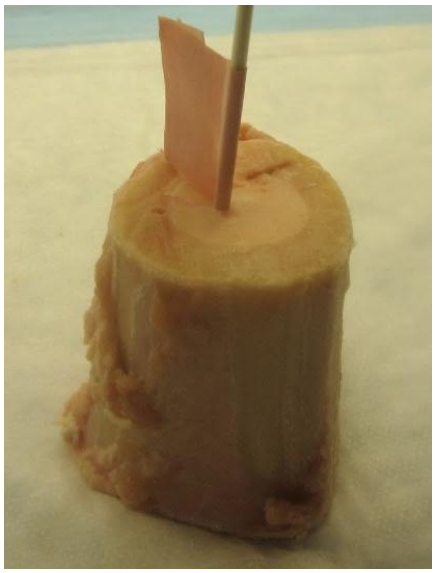

Figure 3.4 Water-cooled catheter inserted into a bovine medullary cavity 8.5 mm from thick cortical bone.

In a preliminary bench-top experiment, temperature was monitored using two invasive temperature probes: a fiber-optic temperature probe and a thermocouple, both inserted along the bone surface into the medullary cavity at the location of maximum expected bone heating (Figure 3.5). Variable power levels were applied in order to determine what powers could provide high (~40-60°C) temperature increases over an extended heating process (Table 3.2). The femur was heated for 825 seconds with the following acoustic output intensities:

Time (s)	0-318	318-390	390-480	480-640	640-825	825-1320
Acoustic intensity on tip transducer (W/cm^2)	8.0	9.3	12.1	13.8	12.1	0.0
Acoustic intensity on 2^{nd} transducer (W/cm^2)	7.9	9.6	12.4	14.1	12.4	0.0

Table 3.2 Acoustic intensities as varied over time

To confirm that the two temperature sensors were in agreement and calibrated to the same values, the thermocouple was repositioned to a location immediately adjacent to the fiber-optic temperature probe 45 sec after power was shut off (860 sec after heating began).

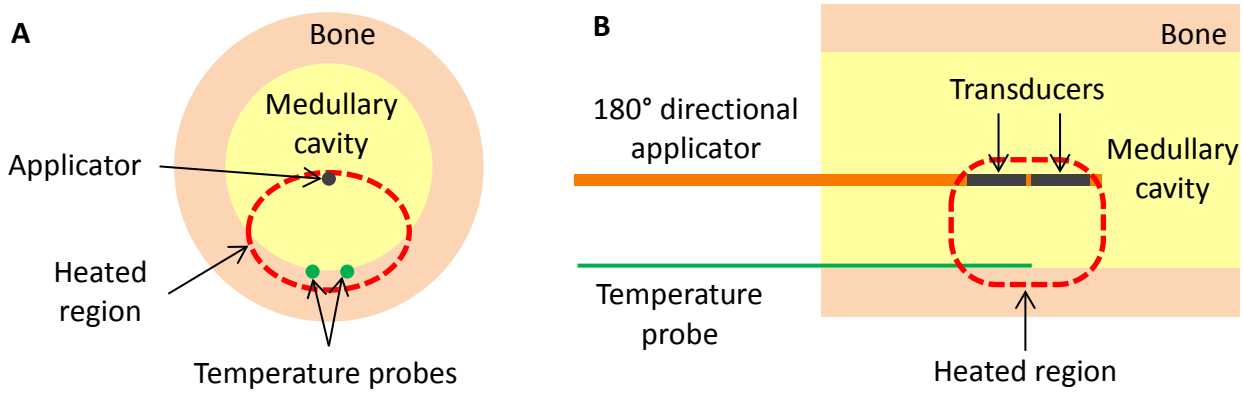

Figure 3.5 Cross-sectional diagrams of applicator and temperature probe placement in the medullary cavity in the bench-top experiment

In a second experiment, temperature was monitored using MRTI. T1 and T2 relaxation times in fat, of which the yellow marrow in the medullary cavity is primarily composed [125], increase roughly linearly with temperature [196, 197]. An 8-channel phased-array wrist coil was used in a Discovery MR 750w 3T scanner (GE Healthcare, Waukesha, WI). The tissue was heated for 26 min and 40 sec at 11.8-12.2 W/cm^2. As previously mentioned, the PRF-based approach for measuring temperature is not accurate in bone. To qualitatively monitor temperature, T2 mapping were performed in bone marrow, and ultrashort echo-time (UTE) sequences were applied for T1 mapping in thick cortical bone, as currently under investigation at UCSF. To monitor temperature changes in the bone marrow throughout heating, T2 mapping was performed with a double-echo 2D fast spin-echo sequence (TR = 666 ms, TE = 35.6 and 185 ms, echo train length = 40, FOV = 10 x 10 cm^2, slice thickness = 4 mm). 10 minutes after heating began, the temperature was assumed to have reached steady state, and 3D UTE imaging was performed to visualize changes in T1 in cortical bone, using a non-selective hard pulse excitation, 3D radial acquisitions, RF spoiling, TR = 11 ms, TE = 76 μs, two flip angles of 8° and 44°, 1 mm isotropic spatial resolution, FOV = 9 x 9 x 7.8 cm^3, and acquisition time = 4.3

min. UTE images and T2 maps were compared to baseline images taken before heating to assess temperature changes.

Simulations of the two experiments were created using Models B-D, and compared to experimental temperature distributions. Following measurements of the bone, the medullary cavity was modeled as a 51 mm long, 21 mm diameter cylinder, surrounded by a 51 mm long, 39 mm outer diameter, 9 mm thick cylindrical cortical shell. A boundary heat flux with h = 10.5 W/m/°C [193, 194] and T_f = 22°C was applied to the outermost tissue surfaces to simulate standing air. The measured and modeled initial tissue temperatures were 17.8°C and 18.6°C for the bones monitored with invasive temperature sensors and MRTI, respectively. Because the acoustic attenuation coefficient of the medullary cavity varies widely with temperature, temperature-dependence was considered, and the attenuation coefficient of the marrow was defined as follows [198], with properties of fat used above 39.1°C [199]:

$$\mu_{medullary\ cavity} = \begin{cases} -1.1787\frac{Np}{m\ MHz\ K}(T-24°C)+29.111\frac{Np}{m\ MHz} & T<24.5°C \\ -1.3158\frac{Np}{m\ MHz\ K}(T-25°C)+26.3149\frac{Np}{m\ MHz} & 24.5°C\le T<33.6°C \\ -0.5208\frac{Np}{m\ MHz\ K}(T-34°C)+14.802\frac{Np}{m\ MHz} & 33.6°C\le T<39.1°C \\ 0.1698\frac{Np}{m\ MHz\ K}(T-44.5°C)+13.075\frac{Np}{m\ MHz} & 39.1°C\le T \end{cases} \quad (3.1)$$

3.3.7 MRTI and invasive thermometry in *ex vivo* cancellous bone

To investigate temperature distributions created by high and low frequency applicators inserted directly into cancellous bone, ablation was performed with applicators placed in an *ex vivo* porcine vertebra and in the heads of *ex vivo* bovine femurs purchased from Animal Technologies (Tyler, TX). Ablations (n=6) were monitored using either T1 mapping or thermocouples.

A preliminary investigation of heat distributions in the spine produced by interstitial ultrasound was performed in an *ex vivo* porcine vertebra (L1) under MR monitoring. Tissues were obtained from Animal Technologies (Tyler, TX). An MR-compatible interstitial ultrasound applicator with two 180° sectored tubular transducers was inserted into a 2.4 mm diameter hole drilled into the vertebra, using an anterior approach. Power was applied only the tip transducer, at 7.8 MHz with an intensity of 7.5 W/cm^2 for 16 minutes. Heating was performed with the tissues situated inside a knee coil in a Discovery MR 750w 3T scanner. T1 mapping of the fat in bone marrow between trabeculae was used to monitor temperature changes in bone (TR = 6.9 ms, TE = 2.2, 3.0, and 3.8 ms, flip angle = 4° and 27°, FOV = 14 x 14 cm^2, 128 x 128 pixels, slice thickness = 3 mm).

A 7.7 MHz applicator with two sectored 180° tubular transducers was inserted into a 2.4 mm diameter hole drilled into a femur head that had equilibrated to room temperature. The tissue was ablated for 19 minutes with an acoustic output of 8.1-8.3 W/cm^2. T1 mapping was performed to determine temperature distributions in cancellous bone, using a flex coil in a Discovery MR 750w 3T scanner. A 3D FGRE sequence with IDEAL fat/water separation was used to map changes in T1 of the fat in the bone marrow between trabeculae (TR = 7.5 ms, TE = 2.18, 2.97, and 3.76 ms, flip angles = 4° and 27°, FOV = 12 x 12 cm^2, 128 x 128 pixels, slice thickness = 3 mm).

To compare high and low frequency ablation, a second experiment employed 6.5 and 4.2 MHz applicators, each with one planar transducer. The bone was degassed under water, and not removed from the water throughout the experiment to avoid air pockets between trabeculae. Two 15 minute ablations at each frequency were performed with 6 W applied electrical power (10.6 W/cm^2 acoustic output at 6.5 MHz, 12.2 W/cm^2 at 4.2 MHz). Temperatures were

measured by two thermocouples inserted parallel to the catheter and 5 and 10 mm in front of it. The depth of the thermocouples within the bone was adjusted during heating to ensure that temperatures were recorded at the level of maximal heating.

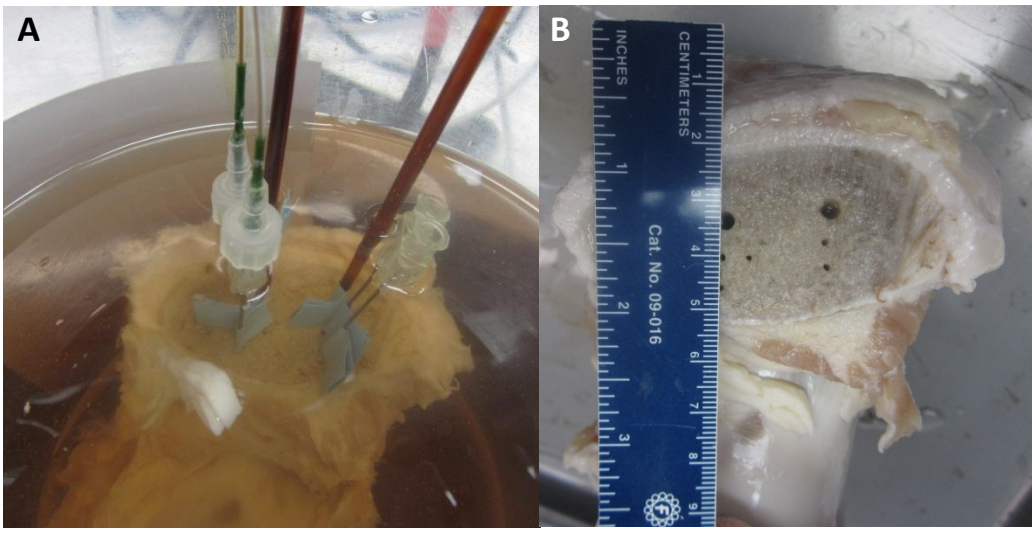

Figure 3.6 Femur head sonicated at 6.5 and 4.2 MHz with planar transducers. Holes were drilled into the bone for two applicator positions, each with a set of two thermocouple positions. (A) Ablation of setup, with a planar applicator and two thermocouples inserted into the bone on the left. An empty polyimide catheter (the second applicator position) and two needles to hold thermocouples are inserted into the bone on the right. (B) Femur head with catheters and thermocouples removed from the large and small holes, respectively. (The small hole to the lower right of the large left hole was unused.)

The ablations performed with cylindrical and planar transducers were simulated using Models B and D. Because the incidence angles on individual trabeculae are not the same as the incident angles on bulk tissue, Models A and C are not applicable to cancellous bone. In Model D, all acoustic energy was assumed to be absorbed on the bone surface adjacent to the catheter. The bone was modeled as a 5-5.1 cm long, 6 cm diameter cylinder with an applicator positioned in the center. Equations 2.23, 2.24, 2.26, and 2.28 were used to describe heat deposition from tubular transducers. Heat deposition Q (W/m^3) from planar transducers was calculated using techniques adapted from Moros et al. and Lin et al. [161, 173]:

$$Q^{B}_{2,\text{planar}} = 2\mathcal{T}_I \alpha I_s e^{-2\int_{x_t}^{x} \mu dx'} \tag{3.2}$$

$$q^{D}_{2,\text{planar}} = \mathcal{T}_I \cos\theta_2 \, I_s e^{-2\int_{x_t}^{x} \mu dx'} \tag{3.3}$$

where $\mathcal{T}_I$ is the acoustic intensity transmission coefficient at normal incidence (96.6%, calculated using Equation 2.22), α is the ultrasound absorption coefficient (Np/m), I_s is the acoustic intensity on the transducer surface (W/m^2), x is the x-coordinate, x_t is the x-coordinate of the transducer surface, μ is the ultrasound attenuation coefficient (Np/m), and θ_2 is the angle (radians) between the transmitted wave and the normal to the bulk bone surface, which is assumed to be the same as the angle between the incident wave and the normal to the bone surface. Superscript B refers to Model B, superscript D refers to Model D, and subscript 2 refers to bone. The cosine term defines the normal component of the energy flux through the bone surface. Heat deposition is calculated in front of the planar transducer and is set to zero beyond the length and width of the transducer.

Because the 50.8 μm thick catheter is too thin to resolve with a 0.4 mm finite element mesh, the inner and outer boundaries were modeled as one, and the heat deposition in the catheter was modeled as a power flux (W/m^2) on the boundary equivalent to the integral of the heat deposition over the boundary:

$$q_{catheter,\text{planar}} = \int_{x_1}^{x_2} 2\alpha I_s e^{-2\mu(x-x_1)} \, dx \tag{3.4}$$

where x_1 and x_2 are the coordinates at which the planar wave enters and exits the catheter.

3.4 Results

3.4.1 Thermal lesions: *Ex vivo* bone and tissue studies

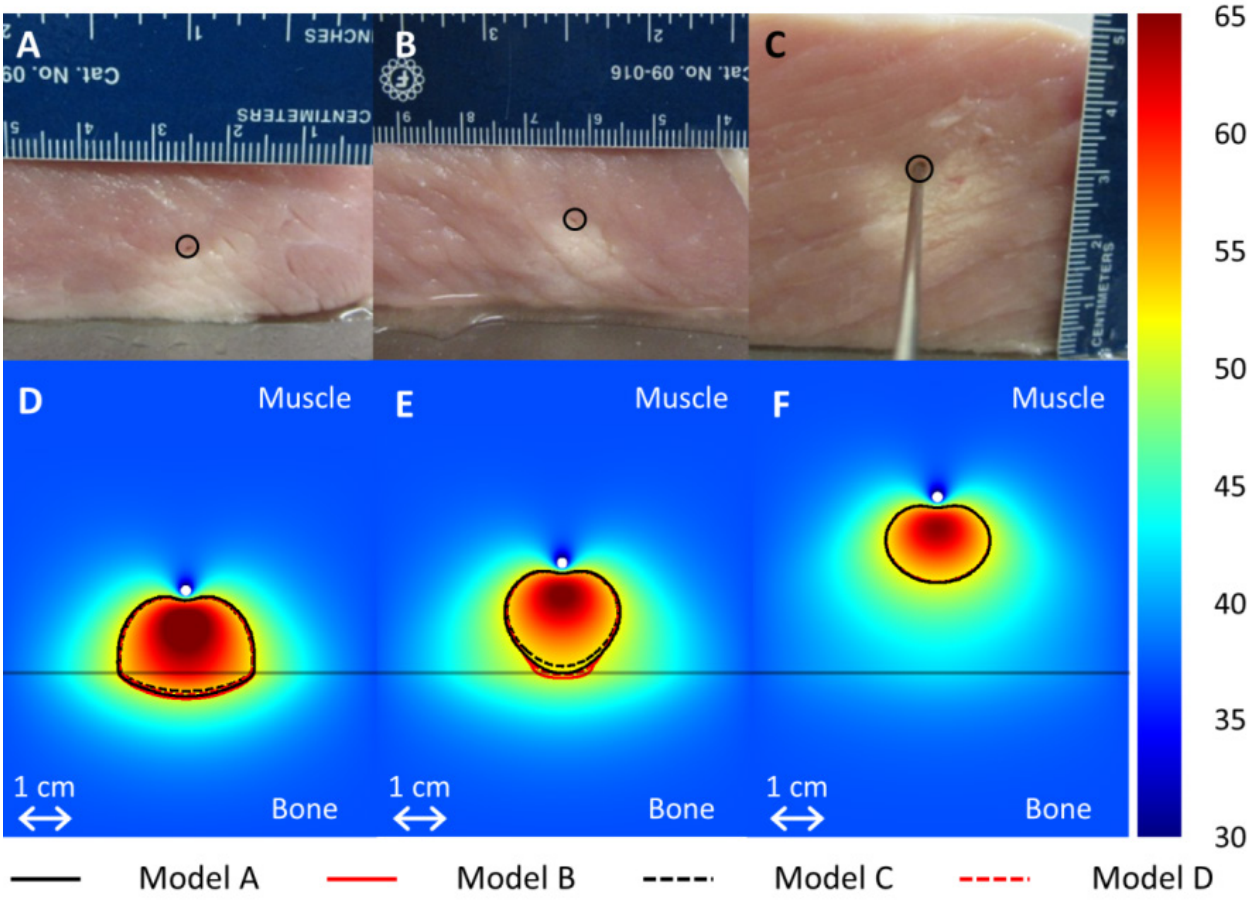

Figure 3.7 (A-C) Thermal lesions created by 10 minute ablations at 12.5 acoustic W/cm^2 in porcine muscle positioned directly atop bovine rib bone, shown in central cross sections through the lesions. The catheter was measured as 15.2, 19.7, and 32.3 mm away from the bone before heating in A-C respectively, and 11.5, 17, and 32 mm away from the bone after the experiment. The catheter track is circled, and the side of the tissue that was against the bone is shown against the table in each image. In (C), a metal rod illustrates the catheter position. (D-F) The experiments were modeled with the applicator 15, 20, and 32 mm away from the bone, respectively, and the results after a 10 minute ablation are plotted in the central plane between the two transducers. The resulting temperature profiles produced by Model A are shown in a color map (°C). A black line indicates the bone/muscle boundary, and curves outline the 52°C temperature contours for Models A-D.

Porcine muscle in a 37°C water bath was ablated using interstitial ultrasound, with the applicator positioned at various distances from flat slabs of cortical and cancellous bone. Models A-D predicted coagulated regions of similar sizes and shapes as those produced experimentally

(Figure 3.7). Model C tended to slightly underestimate the size of thermal lesions as compared to the other models. The measurement of the distance between the applicator and the bone was consistently lower after the ablation, particularly at higher powers, than the measurement from before the ablation, by an average of 2.3 mm, which is attributed to tissue shrinkage during coagulation [200]. Unless otherwise specified, all distances refer to the first measurement.

Bone type	**Power (W/cm^2)**	**n**	**Distances between bone and applicator position, Measurement 1 (mm)**	**Maximum distance from applicator to bone for which ablated zone reached bone, Measurement 1, Measurement 2 (mm)**	**Mean difference between Measurements 1 and 2 (mm)**
Cortical	11.1	6	5-30	14.3, 14.5	0.6
Cortical	12.5	6	5-32.3	15.2, 11.5	2.4
Cancellous	12.5	10	6-29.2	15, 13.3	1.6
Cortical	22.2	6	13.7-35	21.5, 15.5	4.1
Cancellous	22.2	1	14.8-14.8	14.8, 10	4.8

Table 3.3 Powers applied and distances between applicator and bones during experiments with porcine tissue set atop a bone in a 37°C water bath.

All tissue between the applicator and bone could be fully ablated at 11.1-12.5 acoustic W/cm^2 when the applicator was placed within 14.3-15.2 mm of cortical or cancellous bone, or 11.5-14.5 mm as measured after the ablation (Table 3.3). At 22.5 W/cm^2, all tissue between the applicator and cortical bone could be ablated with the applicator up to 17.5-21.5 mm from the bone (or 14.3-15.5 mm as measured after the ablation). At 11.1-12.5 W/cm^2, the size of the lesions created on the face of the tissue pressed against the bone was largest in two trials when the applicator was placed 9.2-11.5 mm from the bone. These two lesions were 26 and 25 mm long, 21 and 21 mm wide, and 8 and 7 mm high, respectively.

In the two cases when the center of the applicator was placed 5-6 mm away from the bone, creating lesions 1 – 3 mm high spanning the distance between the bone surface and the

applicator, the tissue that was pressed flat against the bone turned brown. The brown coagulated region did not extend from the surface into the volume of the soft tissue. The lesion was wide along both directions in the plane of the bone surface, but only present in the narrow region between the catheter and the bone, as well as next to either side of the applicator.

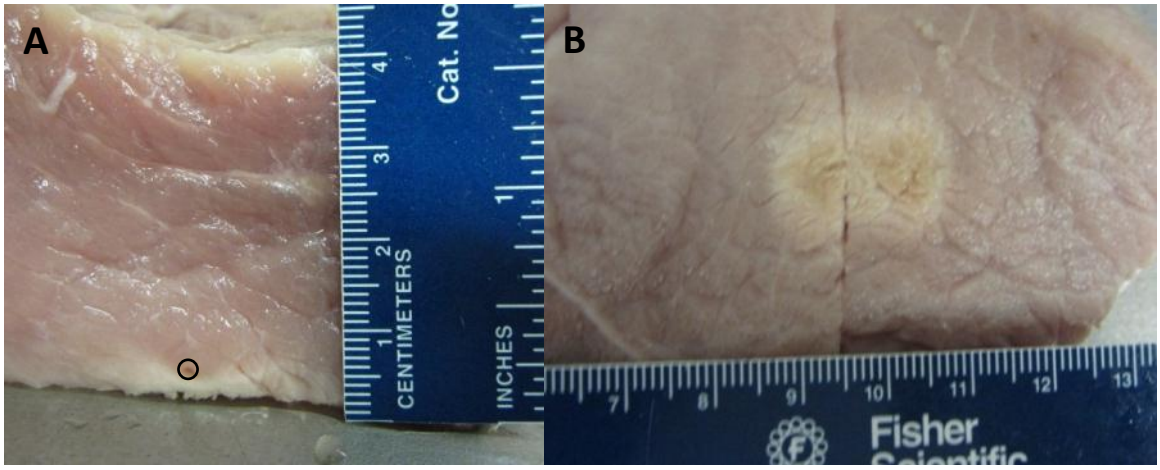

Figure 3.8. Thermal lesion created by 10 minute ablation at 12.5 acoustic W/cm^2 in porcine muscle positioned directly atop bovine vertebral bone. The catheter was measured as 6.0 mm away from the bone before heating, and 3 mm away from the bone after the experiment. (A) Central cross section through the lesion in a plane perpendicular to the applicator. The catheter track is circled, and the side of the tissue that was against the bone is shown against the table. (B) The surface of the tissue that was adjacent to the bone.

Although the thermal lesions reached the bone surface in 16 of the 29 trials, discoloration of the bone itself was rarely observed. Thermal lesions in cancellous bone are difficult to visualize due to the spongy structure. The only case with an unmistakable thermal lesion in the bone occurred when the applicator was placed 5 mm away from cortical bone (2 mm by the second measurement) and ablated at 12.5 W/cm^2.

Figure 3.9 Thermal lesion on a rib bone.

3.4.2 Phantom studies with invasive thermometry

Figure 3.10 shows a series of temperature profiles measured in one phantom containing a rib bone (A) and another phantom containing cancellous bone (B) after 10 minute ablations by applicators positioned 5-30 mm from the bone/phantom interface. The temperatures were measured by thermocouples along a line running through the bone, into the phantom, and alongside one transducer (Figure 3.3). The experiments were modeled, and the theoretical results created using the constant transmission volumetric model (Model B) are superimposed over experimental data in Figure 3.10. The temperature peaked near the applicator, and a secondary peak or inflection was observed at the bone surface, behind which the temperature would sharply drop off. This secondary peak, which widened the heated zone, was more prominent 5 minutes into the ablation, before conduction smoothed it. When the bone was within 1 cm of the applicator, the primary and secondary peaks overlapped, producing a single, higher temperature peak. The simulated models A-D demonstrated all of these trends in temperature.

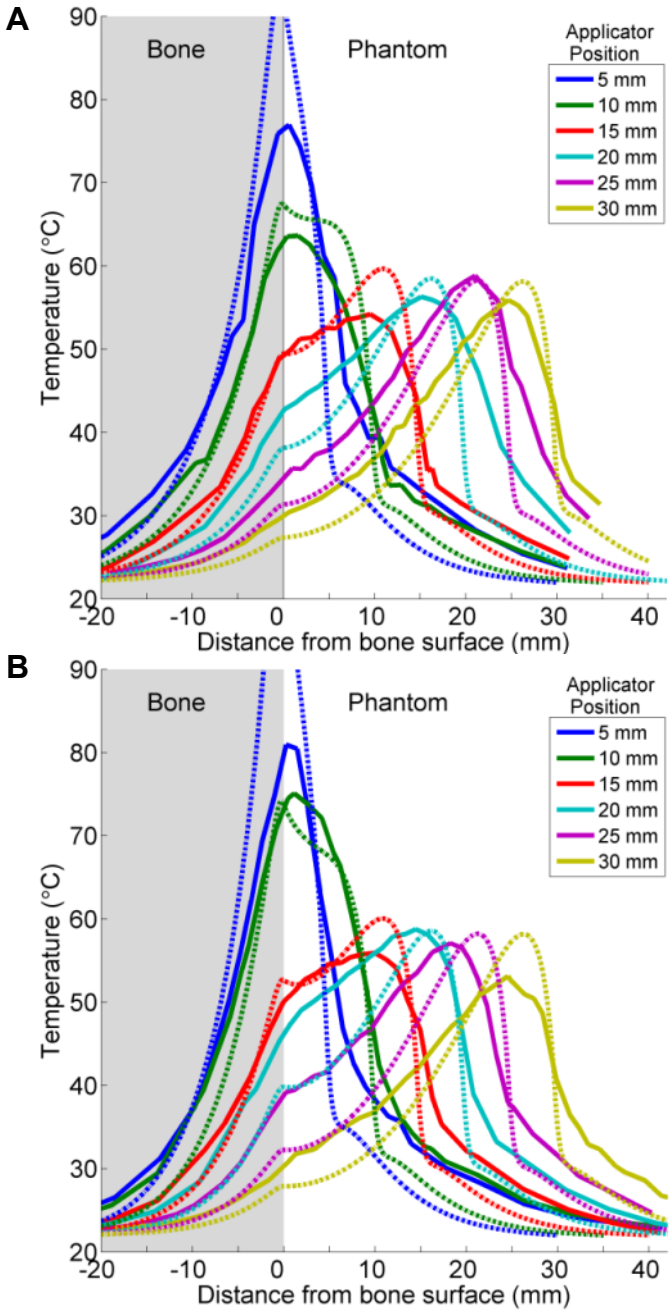

Figure 3.10 Experimental (———) and simulated (- - -) temperature profiles after 10 minute ablations in two phantoms containing cortical (A) or cancellous (B) bone. Temperature along a line perpendicular to the bone surface and adjacent to the center of one transducer, as in Figure 3.3, is plotted as a function of distance from the bone surface, which is at x = 0. Positive x-values are in the phantom, and negative values are inside the bone. Each solid curve corresponds to a single experimental trial with the applicator placed at the designated distance from the bone. The experiments were simulated with Model B, and the theoretical results are superimposed as dashed lines.

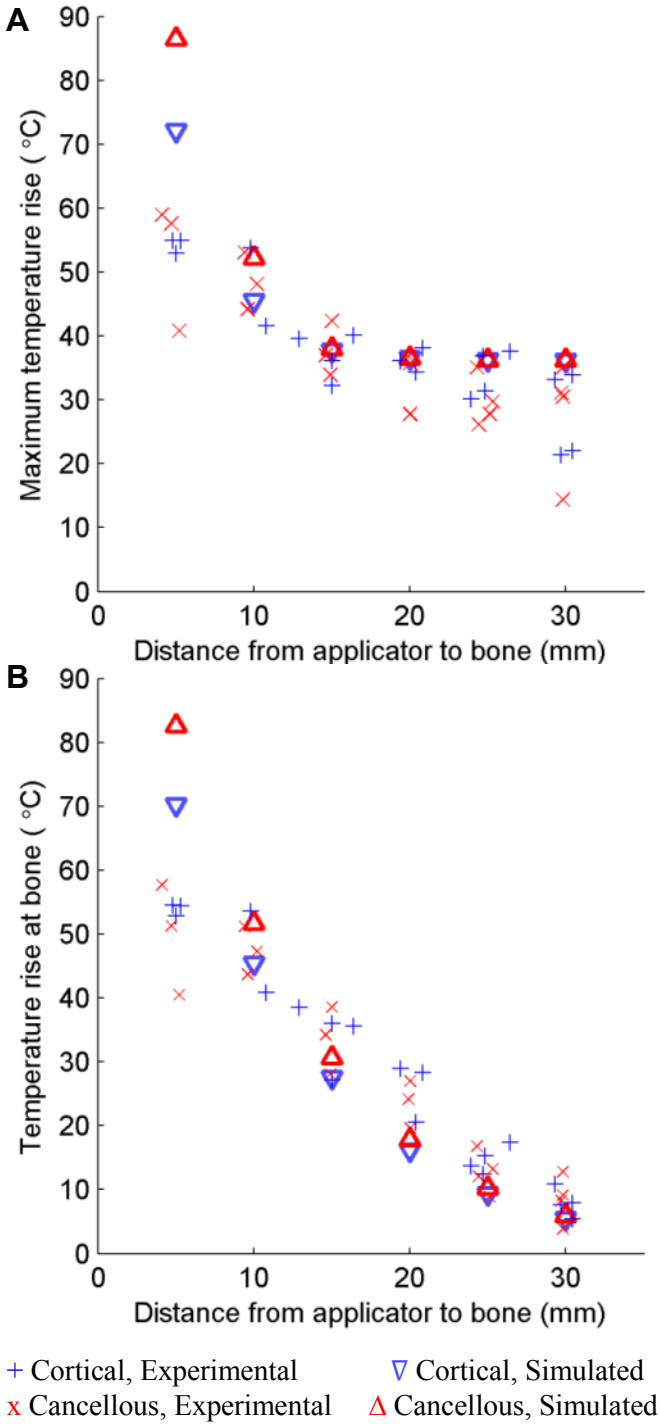

Figure 3.11 The maximum temperature increase measured at the end of each 10 minute ablation of a phantom with an embedded bone is plotted in (A). The temperature increase at the bone surface at the end of each trial is plotted in (B). Peak (A) and bone (B) temperature increases produced by simulations using the constant transmission longitudinal model (Model B) are superimposed.

The maximum temperature rises recorded after a 10 minute ablation are plotted against the distance between the applicator and the bone surface for each of the 40 trials in Figure 3.11A, with simulated data superimposed. Figure 3.11B shows the recorded and simulated temperature rises at the bone surface for each trial. Ablations of phantoms containing cortical and cancellous bones produced very similar temperature rises. The maximum temperature achieved tends to be constant with respect to applicator location until the applicator is within 1 cm from the bone, at which point the primary and secondary temperature peaks overlap, and the maximum temperature increases sharply. Overall, the simulations predicted the maximum temperatures fairly accurately and reproduced the same trends as experiments. Some deviations between the two were observed, in that the simulations underestimated bone surface temperatures when the applicator was 15 mm or more from the bone, and over-predicted bone surface temperatures when the applicator was 5 mm from the bone.

Figure 3.12 shows the mean measured temperature profiles from experiments compared to simulated temperature profiles corresponding to each of the four models, for two example cases with the applicator 10 and 25 mm from cortical bone. Good agreement was observed between the experimental temperature profiles and simulations with Models A-D for all six distances between the applicator and the bone, with correlation coefficients ranging between 0.852 to 0.967 (Table 3.4). The maximum p-value, based on a t-statistic, was 1.9e-31. The correlation coefficients between Model A and Models B-D were at least 0.995 for all six applicator locations, with maximum p-values, based on a t-statistic, of zero.

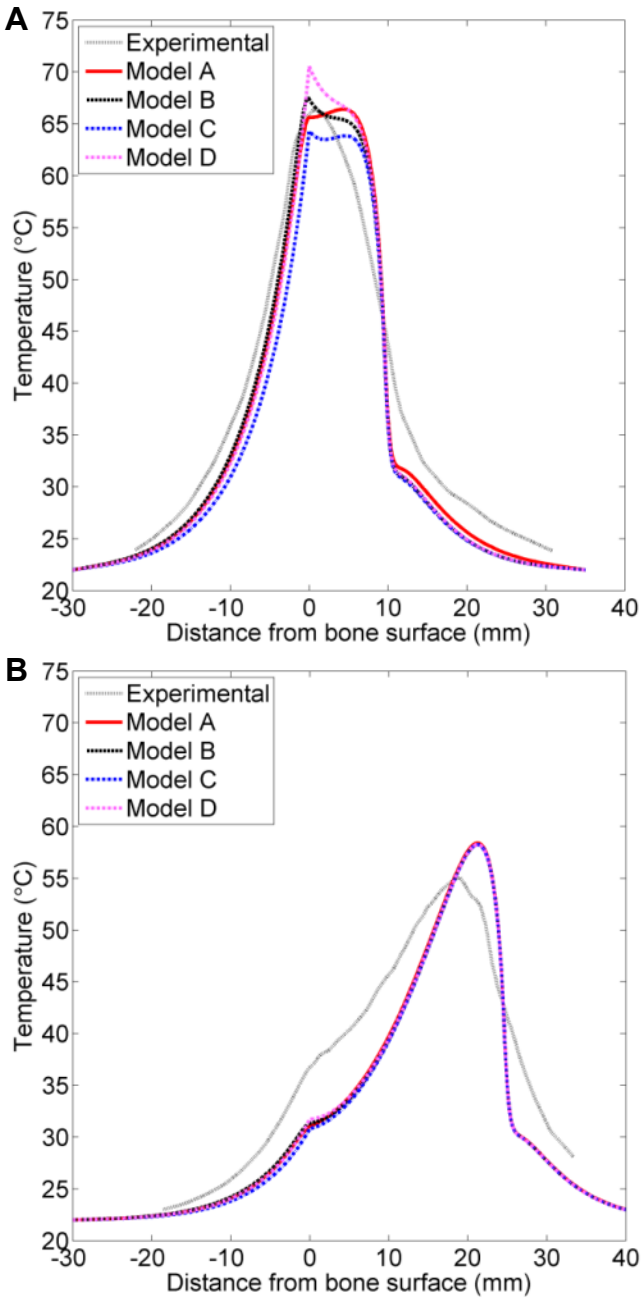

Figure 3.12 Simulated and experimental temperature profiles in phantoms with an applicator placed 10 mm (A) and 25 mm (B) from a rib surface. Temperature along a line perpendicular to the bone surface and adjacent to the center of one transducer, as in Figure 3.3, is plotted as a function of distance from the bone surface, which is at x = 0. Recordings were made after 10 minutes of heating. The experimental curve is an average of the recordings in 3-4 experiments with the applicator at the given position. The bone surface is at x = 0. Positive x-values indicate locations in the phantom, and negative values are inside the bone.

Distance between applicator and bone (mm)	30	25	20	15	10	5
Model A	0.854	0.893	0.886	0.901	0.955	0.967
Model B	0.853	0.892	0.888	0.908	0.960	0.958
Model C	0.852	0.890	0.878	0.889	0.944	0.961
Model D	0.853	0.893	0.890	0.907	0.955	0.958

Table 3.4 The correlation coefficients between each of the 4 models A-D and the temperature measurements recorded at all thermocouple locations in 3-4 phantoms after a 10 minute ablation were calculated for each of the 6 applicator positions. The maximum p-value, based on a t-statistic, was 1.9e-31.

3.4.3 MRTI of *ex vivo* bone and soft tissue

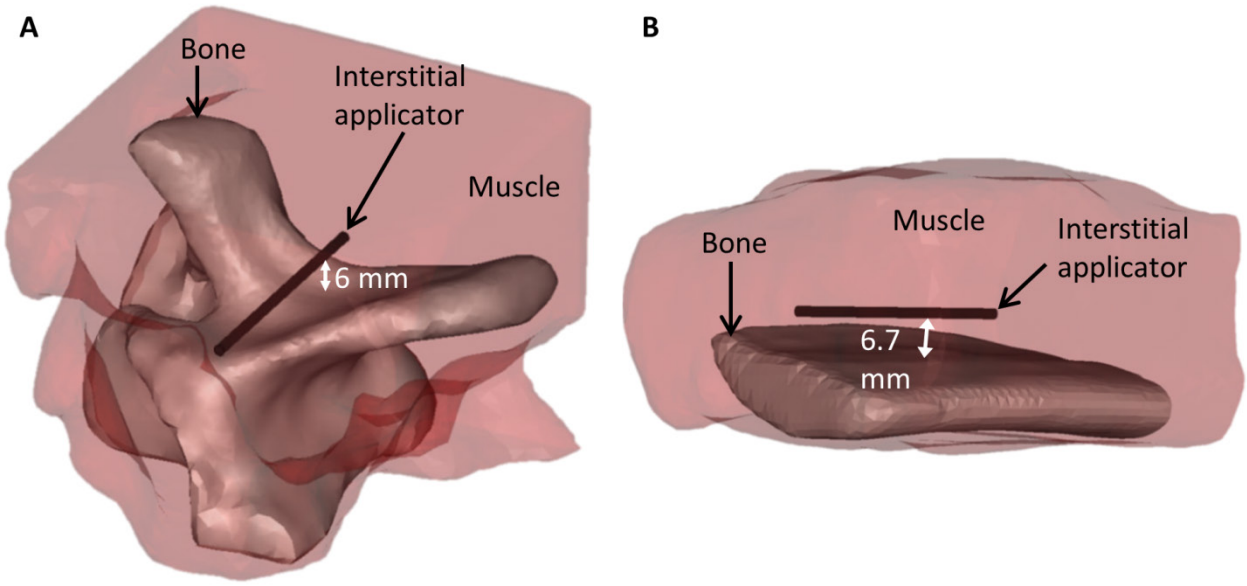

Figure 3.13 3D objects that were meshed to model the bovine vertebra (A) and bovine rib (B) ablations monitored by MR thermometry.

The FEM meshes created based on segmented MR images captured the applicator position and the complex geometry of the soft tissues, bovine rib, and bovine vertebrae heated under MRTI monitoring (Figure 3.13). Parametric studies with complex geometries based on segmented MR images as well as with simple geometries based on the phantom setup indicated that a 0.3-1 mm

mesh was necessary on heated portions of the bone surface when using Models A and B, depending on the distance between the applicator and the bone, while a 0.8-1 mm mesh on heated bone surfaces was sufficient for Models C and D. The total mesh sizes and computation times for the rib models were 413,000 elements and 47 minutes for Model B, and 350,000 elements and 32-36 minutes for Models C and D. For the vertebra case, the simulations performed with Model B had 802,000 elements and took 85 minutes, while simulations using Models C and D had 428,000 elements and both took 49 minutes. These ten-minute-long transient simulations were performed on an Intel Xeon X5680 processor.

With the applicator placed 5-10 mm above the curved surface of the vertebrae, MRTI registered a maximum increase above room temperature of 49°C. With the applicator positioned 7-9 mm above the rib, MRTI registered a maximum temperature increase of 45-48°C. No visible thermal lesions were observed in either case upon dissection after heating.

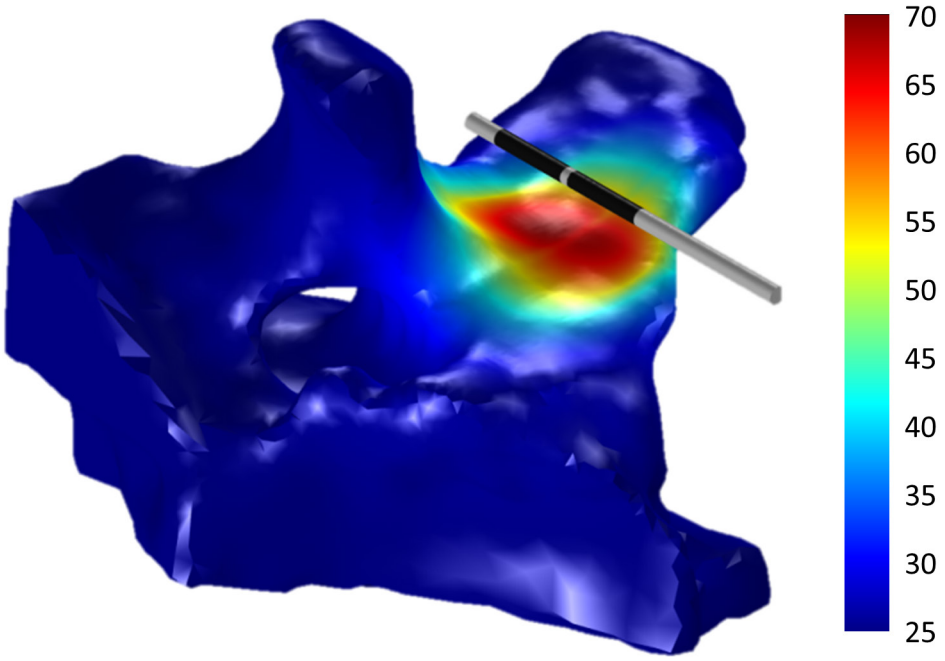

Figure 3.14 Temperature profile (°C) produced by Model D after 10 min of heating on the bone surface of the *ex vivo* bovine vertebra segment heated under MRTI monitoring. The applicator is shown in gray, with transducer locations indicated in black.

Figure 3.14 shows the temperature distribution on the vertebral bone surface produced by Model D. Figure 3.15 and Figure 3.16 show the recorded temperature increases and simulated temperature contours 5 minutes into the ablation, when all soft tissue between the applicator and the bone was heated at least 15°C, which is ablative under *in vivo* conditions [191]. The predictions of the temperatures, as the well as the shapes and sizes of the isothermal contours, produced by Models B and D were in fair agreement with MRTI. Model C produced the smallest contoured areas, and Model B produced the largest.

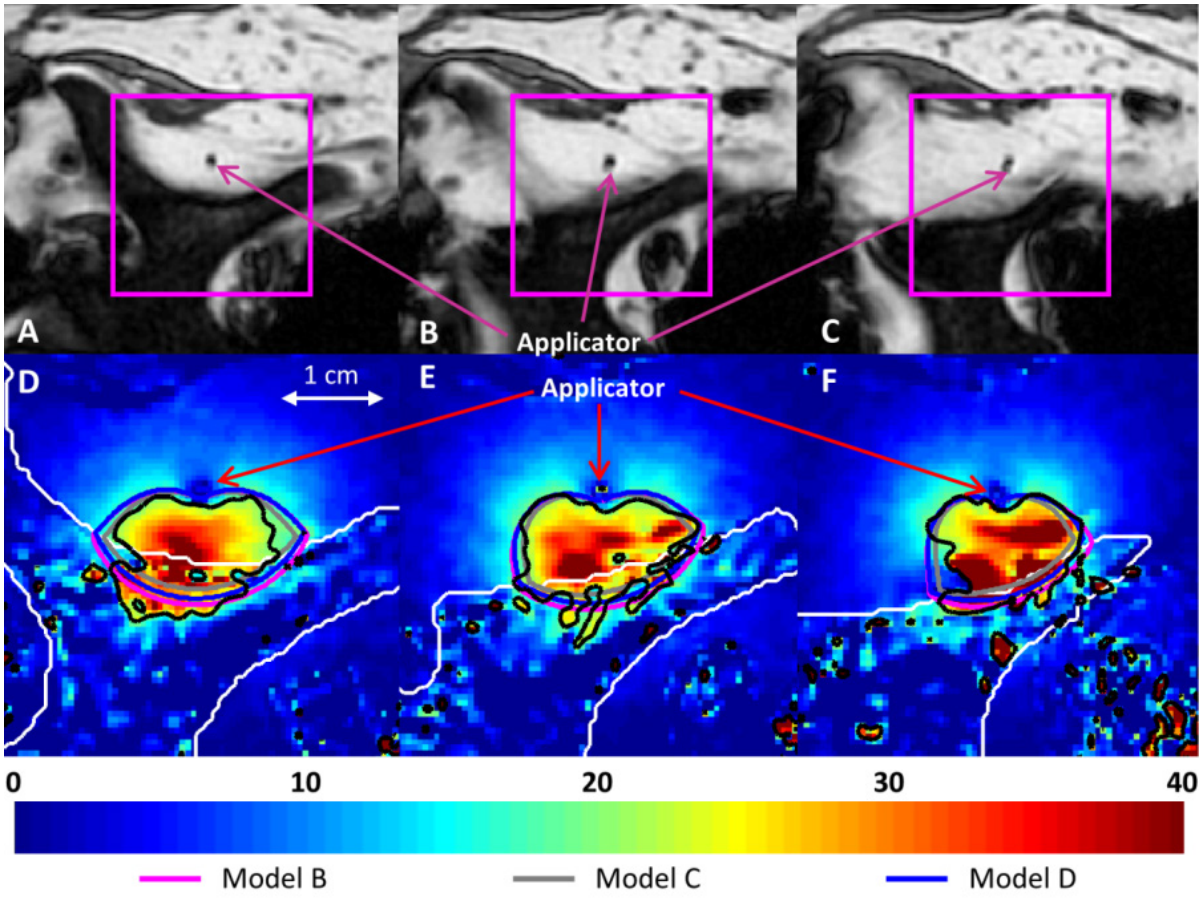

Figure 3.15 (A-C) MR images of the 3 central heated axial slices of ex vivo bovine vertebrae, spaced 5 mm apart. (D-F) Color map of temperature increases (°C) recorded with MRTI in a smaller field of view (magenta box) for each slice 5 min into the ablation. Bone is outlined with a white line, and the 20°C temperature increase contours recorded by MRTI are outlined in black. Also shown are the simulated 20°C temperature increase contours produced by Models B (magenta), C (gray), and D (blue).

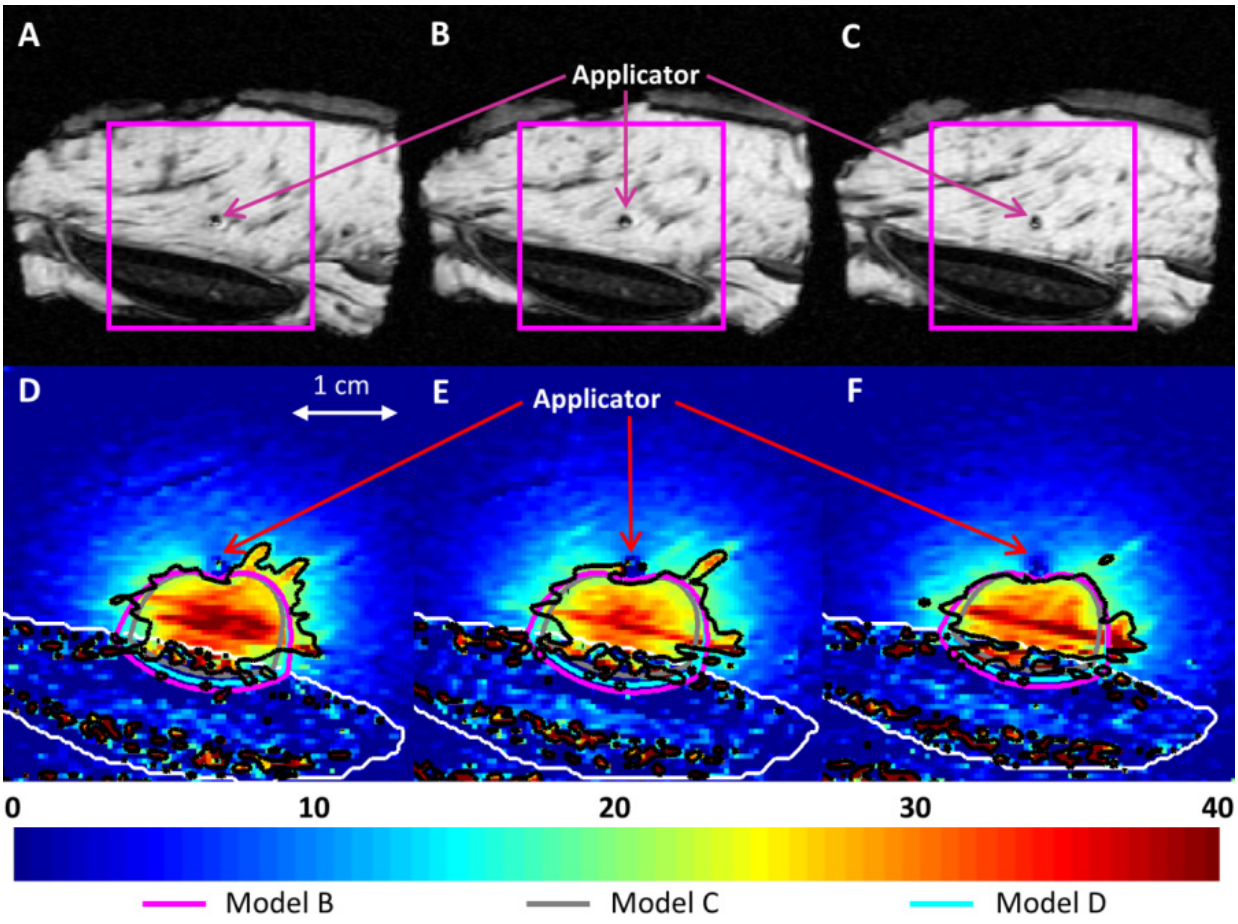

Figure 3.16 (A-C) MR images of the 3 central heated axial slices of ex vivo bovine rib, spaced 5 mm apart. (D-F) Color map of temperature increases (°C) recorded with MRTI is shown in a smaller field of view (magenta box) for each slice 5 min into the ablation. Bone is outlined with a white line, and the 20°C temperature increase contours recorded by MRTI are outlined in black. Also shown are the 20°C temperature increase contours produced by Models B (magenta), C (gray), and D (cyan).

In the muscle surrounding the vertebrae in a 24 x 33 x 30 mm region around the transducers, the temperatures produced after a 10 minute ablation by Model B had an error of 0.1±4.0°C (mean ± standard deviation), Model C had an error of -1.2±3.8°C, and Model D had an error of -0.1±3.9°C when compared to experimental measurements. In the muscle surrounding the rib in a 24 x 37 x 30 mm region around the transducers, the temperatures produced by Model B had an error of -1.3±3.9°C (mean ± standard deviation), Model C had an

error of -2.3±3.8°C, and Model D had an error of -1.4±3.8°C as compared to experimental measurements.

The deviation of the models from experimental values was less significant at earlier time points. The models under-predicted the mild temperature rises experimentally observed behind the applicator, which is not heated by incident ultrasound energy, with errors less than or equal to the errors in the zones of maximal heating. Generally, lower errors in simulated temperatures were observed in the periphery, away from the zones of maximal heating. Tissue heterogeneity and the limitations of the slice thickness in MR images could possibly contribute to these errors.

3.4.4 MRTI of *in vivo* bone and soft tissue

Interstitial ultrasound ablation was performed in *in vivo* deep thigh muscle with the acoustic output of the applicator directed towards bone. MRTI measured temperature within the soft tissues using PRF-based phase mapping. Figure 3.17 shows the measured temperature distributions in two central slices 5 mm apart. Based on core temperature measurements, the initial body temperature is assumed to be 33°C.

Two temperature peaks were observed: a wide peak close to the applicator and a lower secondary peak immediately adjacent to the curved bone surface, which was 13-28 mm from the applicator. The temperature contours of the directional heating pattern were wider on the side of the active transducer sector pointing towards the bone surface; the 40°C contour extended further out to touch the bone. The peak temperature on the bone surface was 47.6°C, while the peak temperature overall was 81.4°C.

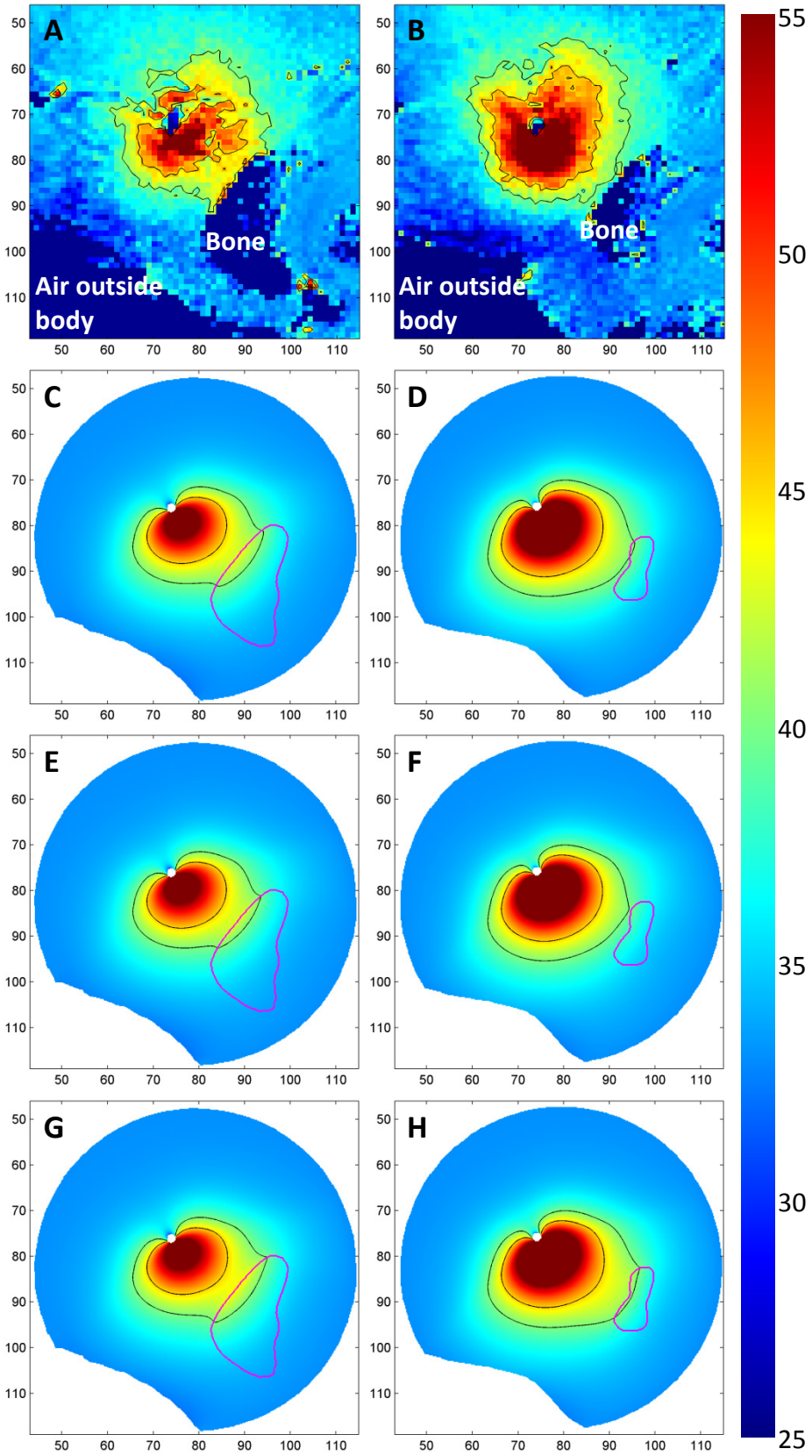

Figure 3.17 Interstitial ultrasound ablation of *in vivo* bone and soft tissue, monitored by MRTI (A-B) in two slices 5 mm apart. Temperature distributions (°C) simulated by Models B (C-D), C (E-F), and D (G-H) in the same slices are also shown. The 40 and 45°C temperature contours are outlined in black in (A-H). The bone is outlined in magenta in (C-H).

3D simulations of the experimental setup using numerical models were predictive of these trends. The simulated temperature distributions and the sizes and shapes of the simulated temperature contours were similar to experimental measurements. Models B, C, and D predicted peak overall temperatures of 75.3, 75.2, and 75.3°C, respectively, which are 6.1-6.2°C lower than the values measured with the PRF method. At the bone surface, Model D generally predicted higher temperatures than the more comprehensive Model B, and Model C predicted lower temperatures than Model B. Models B-D predicted peak bone surface temperatures of 43.5, 43.3, and 44.9°C, respectively, which are only 2.7-4.3°C lower than measured values, with Model D the most accurate. Models B and D estimated that the 40°C temperature contour would extend 3 mm into bone, while Model C estimated that it would only extend 2 mm into the bone. Overall, the temperatures predicted by Models B-D were very similar to one another, differing by 0-3.1°C, with the lowest discrepancies in locations situated away from heated bone surfaces.

3.4.5 MRTI and invasive thermometry in *ex vivo* cortical bone

Interstitial ultrasound applicators were inserted into the medullary cavities of bovine femur bones, and the acoustic outputs of the tubular transducers were directed towards the thick cortical bone. Temperature was either measured in the expected zone of maximal bone heating with a thermocouple and a fiberoptic sensor, or was monitored throughout the volume using T1 and T2 mapping. The experiments were simulated using simple geometric models, with the bones and medullary cavities modeled as cylinders.

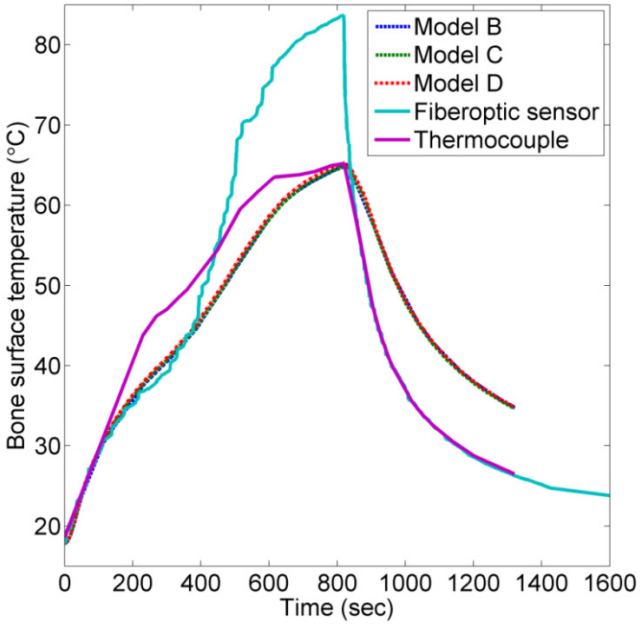

Figure 3.18 Temperatures measured by a fiberoptic temperature sensor and by a thermocouple placed in the medullary cavity along the bone surface in the expected areas of maximal bone heating. The maximum bone surface temperatures calculated using Models B, C, and D are superimposed.

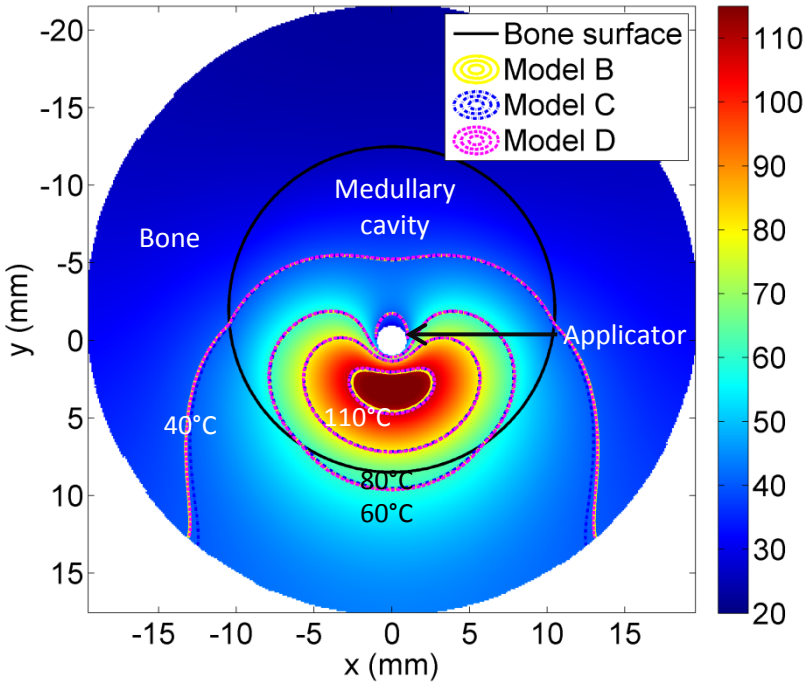

Figure 3.19 Temperature map (°C) in a central plane produced by Model B, shown at the end (t = 825 s) of the ablation of the medullary cavity that was monitored using invasive temperature sensors. The 40°C, 60°C, 80°C, and 110°C temperature contours calculated by Models B, C, and D are superimposed.

High temperatures were measured by invasive temperature probes at the bone surfaces in the medullary cavity, with a maximum of 83.7°C. The two probes measured very similar temperatures at the start of treatment, but the measured temperatures curves diverged after 112 seconds of heating (Figure 3.18). When the thermocouple was repositioned to the location of the fiber-optic probe during cooling, the two sensors were in near-perfect agreement, indicating that device calibration did not contribute to the discrepancy between the two probes. Disparities between the two measurement probes may have been caused by the spatially heterogeneous power output of the transducers and/or by viscous heating artifacts.

The modeled temperature distributions were similar to those measured with invasive thermometry (Figure 3.18). Simulated data closely followed the shapes of the measured temperatures curves, with correlation coefficients of 0.83-0.89, and were quite similar to the temperatures measured by the thermocouple in particular. The temperatures measured by the fiberoptic temperature probe during the first 390 seconds of heating were an extremely close match to simulated data (correlation coefficient = 0.996), though the discrepancy between them increased after the acoustic intensity was increased above 12 W/cm^2.

The temperature distributions calculated by the three models were very similar to one another, as seen in Figure 3.18 and Figure 3.19. The discrepancy between the measurements of the peak bone surface temperature by Models B-D, as plotted in Figure 3.18, ranged from 0.0-0.99°C. Model D produced slightly higher temperatures than the other two, and Model C calculated slightly lower temperatures.

In a second experiment, UTE imaging was used to qualitatively observe temperature-induced changes in T1 in cortical bone, and T2 mapping was used to qualitatively observe temperature-induced changes in T2 in the fat of the medullary cavity (Figure 3.20). T1 maps in

cortical bone indicated moderate thermal penetration through the thick cortical shell. T2 in the medullary cavity, a qualitative measurement of heating, peaked between the applicator and the bone, rather than at the bone surface. Simulations showed the same trends (Figure 3.20B). Models B-D produced temperature distributions very similar to one another, although the temperature contours produced by Model C were significantly lower within cortical bone than those of the other two models.

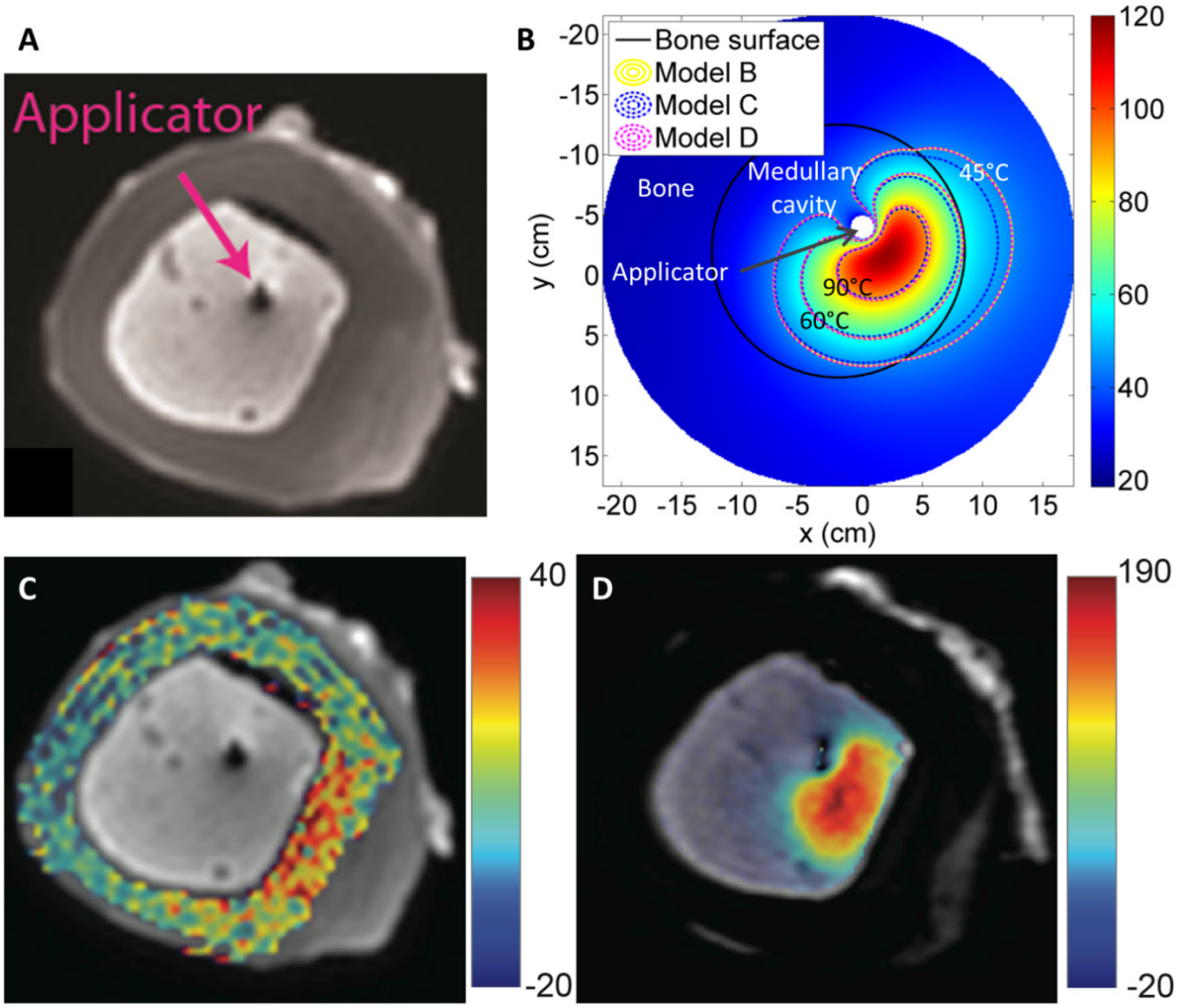

Figure 3.20 (A) shows a UTE image of an *ex vivo* bovine femur. (B) shows a temperature map (°C) produced by simulations of the experiment performed using Model B, as well as 45, 60, and 90°C temperature contours calculated by Models B-D. (C) shows the change in T1 in cortical bone (ms), and (D) shows the change in T2 in bone marrow (ms) over the course of heating. (C-D) qualitatively show heating-induced increases in T1 and T2, rather than quantitative temperature measurements.

3.4.6 MRTI and invasive thermometry in *ex vivo* cancellous bone

The highly attenuating cancellous bone in bovine femur heads and a porcine vertebra was heated with tubular and planar interstitial ultrasound applicators to measure heating distributions, to compare devices, and to investigate theory. The applicators were positioned at the side of the vertebral body or in the cancellous bone near the center of a femur head.

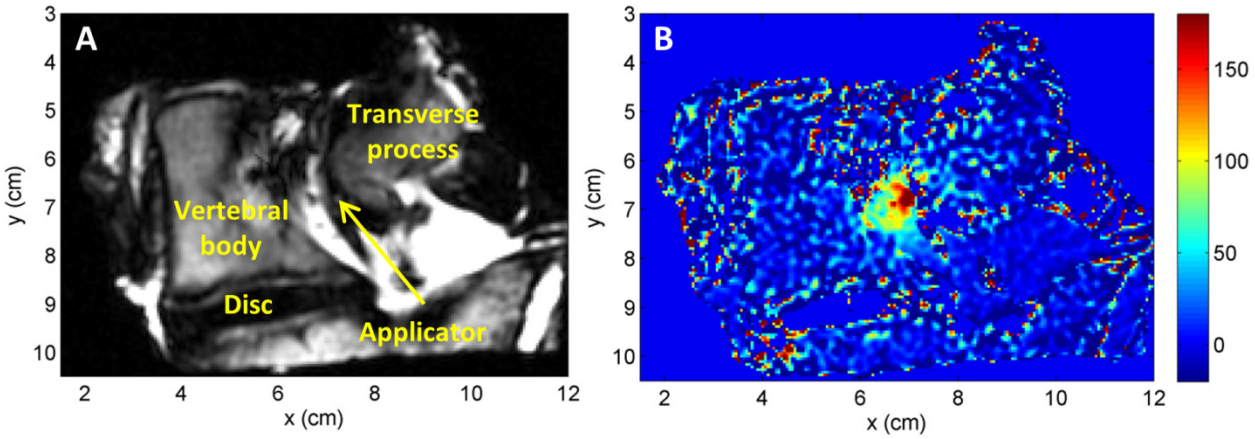

Figure 3.21 (A) Anatomical image in the central heated slice of the *ex vivo* porcine vertebra heated with interstitial ultrasound. (B) Map in the same slice of the changes in T1 (ms) that occurred during heating.

In maps of temperature-induced changes in T1 caused by tubular transducers, the changes in T1 were high near the applicator and fell off very rapidly (Figure 3.21 - Figure 3.22), creating small, well-defined heated regions. Significant heating penetrated less than 2 cm into the bovine femur and the porcine vertebra. Contiguous ΔT1 contours of 100, 200, and 300 ms in the central heated slice had radial depths up to 7.1, 3.3, and 1.6 mm, respectively, from the applicator placed in the vertebra. The maximum recorded values of the change in T1 due to heating in the central slice in the vertebra were 523, 553, and 1243 ms, as observed in 3 pixels around the applicator. Contiguous ΔT1 contours of 50, 100, 200, 300, 600, and 1000 ms in the three central slices of the femur had radial depths up to 13.2, 8.6, 6.1, 4.9, 3.6, and 2.6 mm, respectively, from the applicator center. The maximum values of the changes in T1 in the femur were 1403-3051 ms

(mean 1720 ms, median 1514 ms), as observed in the 9 most heated sonicated pixels in the three central heated slices. As more acoustic energy was deposited into the femur (19 min, 8.1-8.3 W/cm^2, 2 transducers) than into the vertebra (16 min, 7.5 W/cm^2, 1 transducer), more heating and greater thermal penetration over a larger number of slices was observed in the femur.

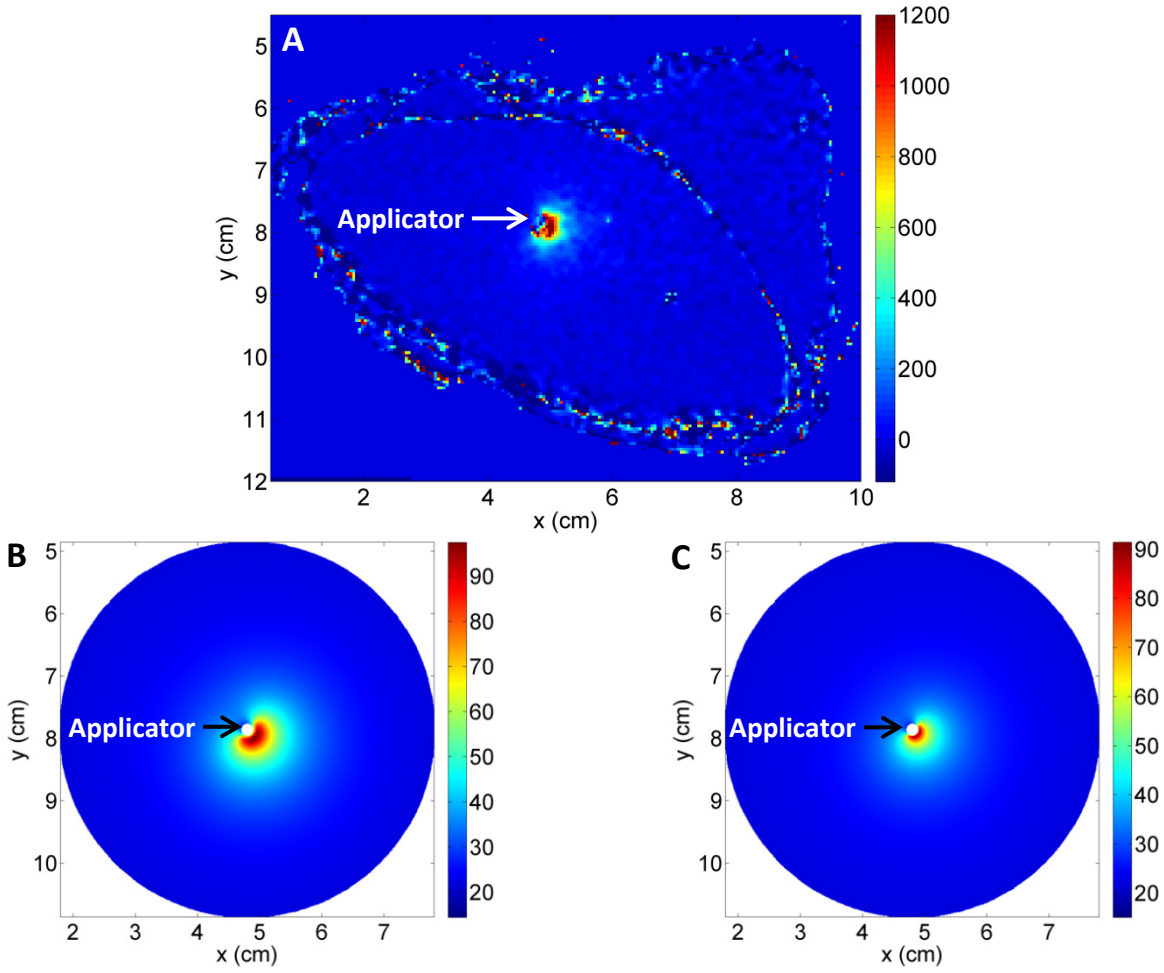

Figure 3.22 (A) Map of the changes in T1 (ms) that occurred during ablation of cancellous bone in an *ex vivo* bovine femur head. (B) and (C) show the temperature maps (°C) produced by Models B and D, respectively, in simulations of the experiment in a slice through the center of one of the two transducers. Temperature color maps in (B) and (C) range from the peak simulated temperature, down to the initial temperature minus 10% of the temperature rise, in accordance with the color scale in (A), which ranges from -120 ms to 1200 ms.

To compare the heating profiles produced in cancellous bone by interstitial ultrasound at various frequencies, bovine cancellous bone was ablated with 6 W of electrical power applied to

6.5 MHz and 4.2 MHz applicators with planar transducers. The acoustic output intensities, areas, and efficiencies of the 6.5 and 4.2 MHz transducers were, respectively, 10.6 & 12.2 W/cm^2, 22.2 & 17 mm^2, and 39.3 34.6%. Temperatures were measured using thermocouples inserted 5 and 10 mm from the applicator.

Frequency (MHz)	**Distance to applicator (mm)**	**Measurement 1 (°C)**	**Measurement 2 (°C)**	**Mean measured (°C)**	**Model B (°C)**	**Model D (°C)**
4.2	5	6.65	12.76	9.7	40.4	11.6
4.2	10	1.44	2.51	2.0	11.8	3.8
6.5	5	19.29	30.49	24.9	28.1	12.4
6.5	10	3.66	11.3	7.5	9.1	4.2

Table 3.5 The maximum temperature rises experimentally recorded 5 and 10 mm in front of planar applicators inserted directly into cancellous bone are shown for each trial (n = 2). The temperature rises in the same locations as calculated using Models B and D are also given.

Invasive temperature probes recorded higher temperatures produced by the 6.5 MHz applicator than by the 4.2 MHz applicator. At both frequencies, temperature sharply fell off with distance from the applicator. The temperature change produced by the 4.2 MHz transducer 5 mm from the applicator was 4.6-5.1 times higher than that 10 mm from the applicator, while the temperature change produced by the 6.5 MHz transducer was 2.7-5.3 times higher at 5 mm from the applicator than at 10 mm.

Simulations reflected these trends. Models B and D predicted that the temperature increases produced by the two frequencies at 5 mm from the applicator would be 3.0-3.4 times higher than at 10 mm (at the same frequency), which is within the range of experimental values. Simulations with Model D, but not Model B, correctly indicated that the high frequency transducer would produce greater temperature increases several millimeters from the applicator than the low frquency transducer would, though the differences between the temperatures

produced by Model D at the two frequencies were less than the differences measured experimentally.

In locations more than a few millimeters from an applicator inserted directly into cancellous bone, Model D approximated experimental heat distributions better than Model B in simulations of four of the five experiments in femur bones. Model D, which assumed a heat source on the bone adjacent to the catheter, predicted less thermal penetration than did Model B, which considered volumetric heat deposition (Figure 3.22, Table 3.5).

Both Models B and D predicted very high peak temperatures close to the applicator, where temperatures were not recorded experimentally. All four simulations, using low and high frequencies and Models B and D, indicated that temperatures surpassed 100°C within 10-20 seconds after heating began, with maximum temperatures at the end of heating of 107.5-144.7°C. These high temperatures fell off quickly with distance from the applicator, resulting in considerably lower temperatures (25.8-62.4°C) predicted 5 and 10 mm from the applicator (). Model B produced significantly higher peak temperatures (144.7 & 127.0°C at low and high frequencies, respectively) than did Model D (118.1 & 107.5°C, respectively), possibly because the bone surface heated with Model D was immediately adjacent to the water-cooled catheter, while Model B allowed for some penetration into the bone away from the water cooling. Based on observations of Figure 3.22, Model B may possibly have approximated experimental temperature distributions very close to the applicator somewhat better than Model D.

3.5 Discussion

The presence of bone within or adjacent to a target region can dramatically influence the heating characteristics of ultrasound therapy in general, and specifically interstitial ultrasound as

addressed in this study. Bone/soft tissue interfaces are complicated by two distinct parameters: the high acoustic absorption coefficient of bone and high acoustic impedance differences. Bone has an ultrasound absorption coefficient 1-2 orders of magnitude higher than that of soft tissue [59], causing preferential heating at bone surfaces [115, 157], effectively creating a secondary heat source away from an applicator placed in soft tissue (Figures 3.10, 3.12, 3.15, 3.16) and insulating structures behind the bone (Figures 3.7, 3.10, 3.12, 3.17, 3.21). Impedance differences result in significant reflection, refraction, and shear mode conversion when an acoustic wave travelling through soft tissue reaches a bone surface. Four simplified models of acoustic heat deposition in bone and soft tissue were compared to experimental measurements in bone/tissue phantoms, *ex vivo* tissues, and *in vivo* tissues. Theoretical and comparative experimental studies demonstrate that these simplifications can provide accurate estimations of temperature distributions with reduced modeling complexity and computational requirements.

Although Model D included the most approximations, it performed very well. Model D approximated Model A (the most comprehensive model) more closely than Models B and C did in almost all locations over a few millimeters away from the bone/phantom interface when the applicator was 1-3 cm away from it (Figure 3.12). Model A, which included reflection, produced slightly higher temperatures in the volumes of soft tissue that are not heated by incident ultrasound energy than did other models (Figure 3.12). The root mean square (RMS) errors in Models A-C, as compared to experimentally measured values in regions heated at least 5°C in phantoms, were each within 0.5°C of the RMS error of Model D. Also, Model D was much better than Model C and just slightly worse than Model B in estimating temperature measurements made by MRTI with the applicator 5-10 mm from bone. When the applicator was

inserted directly into cancellous bone, Model D performed better than both Models B and C in approximating experimentally observed thermal penetration (Table 3.5, Figure 3.22).

The angle-dependent boundary model (Model C), however, consistently produced temperature distributions that were overall lower than the 3 other models and MRTI data (Figures 2.6, 2.7, 3.4, 3.9, 3.12-3.14). In regions with measured temperature increases over 15°C, Model C produced temperature increases 3.1±3.5% (mean ± standard deviation) below those of Model A in phantoms, and 6.9±13.2% below those of thermocouple measurements in phantoms. The low heating observed in Model C may have resulted from the use of lower transmission and attenuation coefficients near normal incidence than Models B and D, as well as from neglecting the heat generated by reflected waves. When constant transmission coefficients are used (Models B and D), the lack of reflected energy resulted in only a slight decrease in soft tissue temperatures as compared to Model A (Figure 3.12).

Models A, B, and D are all suitable for simulating interstitial ultrasound ablation involving bone. The volumetric models A and B, however, can require a much finer mesh size (0.3-1 mm) at the bone surface than the surface models C and D (0.8-1 mm), possibly because they may need a fine resolution to capture the rapid falloff in acoustic intensity behind the bone surface. This greatly increases computational time, particularly when the bone has a high surface area. Model A is also difficult to model in complex geometries, as the paths of reflected and refracted beams must be traced. Although development of a fast modeling platform is not a primary goal of this study, the impact of model approximations on computation time was analyzed in consideration of potential future treatment planning applications. Since Models A, B, and D yield similar temperature predictions, the simplest and fastest one would be best suited to treatment planning. As such, Model D may be the most practical method for accurately

simulating interstitial ultrasound bone ablation, with Model B preferable in cases when the bone is less than 1-2 mm thick.

Simulations produced temperature profiles and ablated volumes that closely matched experimental data in size and shape (Figures 3.4, 3.7-3.9, 3.12-3.15, 3.17, 3.18). The difference between the outputs of the four models was generally less than the difference in measurements from different experimental trials, and simulated temperatures generally fell within the range of temperatures measured experimentally using invasive temperature sensors and MRTI. The main exception was the over-prediction of peak temperatures in phantoms when the applicator was 5 mm from the bone surface. Thermocouple conduction artifacts, which smear heating along the multi-junction thermocouple wires, may have contributed to this discrepancy [121]. This artifact would be more pronounced when a large amount of heat is deposited in a small region, as in the 5 mm phantom case, lowering the measured temperatures below the actual temperatures. Discrepancies between measured and simulated data, and between multiple experimental trials (Figure 3.11, Figure 3.18, Table 3.5), may also be partially due to errors and/or inconsistencies in the alignment of invasive temperature sensors with the acoustic output, which is nonuniform with peaks and valleys. The predicted temperatures at the phantom/bone interface when the applicator was 10 mm or more away from the bone or inserted directly into bone were generally within the range of experimental values (Figure 3.11, Table 3.5). Figures 3.4, 3.7-3.9, and 3.12-3.14 show fairly good agreement of temperature and thermal dose profiles between models and the experiments at the end of treatment, especially in the zones of maximal heating. Discrepancies between the models and experiments were generally even smaller at earlier time points and in locations away from the zones of maximal heating.

These simulations do not consider energy contributions to the vaporization of water or the material properties of gas. The vast majority of experiments were performed well below the boiling point of water (Figures 3.7, 3.8, 3.12-3.14). However, simulations of experiments with the applicator inserted directly into bone predicted temperature rises approaching (tubular transducers in cancellous bone) or above (medullary cavity experiments and planar transducers in cancellous bone) the boiling point of water. Because the models do not consider the energy applied to convert water from liquid to gas, the material properties of water vapor, or ultrasound reflection off of bubbles of water vapor, they can be inaccurate above the boiling point of water. This may be a reason why Model B, which produced higher temperatures than Model D, predicted inaccurately high thermal penetration from applicators inserted into cancellous bone (Figure 3.22,). If water vaporization were taken into consideration, Model B could potentially be more accurate in such cases. Nevertheless, gas formation was not observed in MR images of cancellous bone or of the medullary cavity, perhaps due in part to low water content in the medullary cavity, so these two sets of simulations may potentially be valid.

The results of this study demonstrate the importance of modeling the interactions of interstitial ultrasound with bone, as preferential bone heating can dramatically impact heating and thermal dose profiles. Simulations and temperature measurements in phantoms indicate that when an applicator is within 1 cm of the bone surface, the temperature peaks at the bone surface and in the soft tissue overlap, creating a high, narrow peak near the bone surface (Figure 3.10). When the applicator is further from the bone, the secondary peak at the bone surface can widen the ablated region without significantly changing peak temperatures (Figure 3.10, Figure 3.11, Figure 3.17). This effect is more pronounced at low attenuations and perfusions, for which ultrasound can penetrate further into the tumor to reach the bone and less of the absorbed energy

is carried away by flowing blood (Figure 2.7). When the applicator was placed 8.5 mm from the bone surface in the medullary cavity, temperature peaked in the medullary cavity between the applicator and the bone (Figure 3.19, Figure 3.20), rather than at the bone surface as it did in phantoms (Figure 3.10), as the medullary cavity has a much higher attenuation coefficient than phantom or muscle [59, 190, 198].

The results of this study agree with those of Moros et al., who performed similar experiments using phantoms with bone inclusions and an external planar transducer to study hyperthermia at 1.0 and 3.3 MHz in superficial tissues above bone [201]. They found that increased heating near the bone surface can be significant, and that it can be used to enhance acoustic and thermal penetration into deep tissue regions directly above bone. These studies also corroborated extensive theoretical investigations [161, 165], which were employed in part for the development of our models herein.

In contrast to other simulations (see Section 5.4), experiments and simulations using Model D did not show that ablation at lower frequencies could provide increased penetration into bone. These disparities may be partially due to the low sample size (n=2 for each frequency) and the difference in the size and efficiency of the two applicators considered. The same powers were applied to the two applicators, but the 6.5 MHz applicator was larger (10.1 x 2.2 mm) and slightly more efficient (39.3%) than the 4.2 MHz applicator (8.5 x 2.0 mm, 34.6%). Because the transducers were small, any misalignment between the applicators and the thermocouples could result in significant inaccuracies in the measured temperatures.

Comparison with MRTI data shows that the simulations of irregularly shaped bones produced fairly accurate biothermal and acoustic models (Figure 3.15 - Figure 3.17). MRI is highly useful for its ability to monitor heating and to create images on which 3D models for

treatment planning can be based. MRTI measured temperature rises in the soft tissue adjacent to bone using the PRF method. MRTI data within bone measured with the PRF method herein is inaccurate because cortical bone has a very short T2 relaxation time [124] and because cancellous bone has a high fat content. However, mapping of changes in the T1 and T2 relaxation times of fat was applied to qualitatively visualize temperature distributions in bone marrow, and UTE imaging was successfully applied to qualitatively visualize temperature distributions in cortical bone.

3.6 Conclusion

Models and experimental data showed that preferential heating at bone surfaces can cause higher temperature elevations or allow larger volumes to be ablated with interstitial ultrasound than in the absence of bone. Four types of biothermal and acoustic models of interstitial ultrasound ablation involving bone, applying various approximations, were validated through comparison to experimental data. Three of the models produced temperature and thermal dose profiles similar to those observed experimentally. Approximations that considered a constant transmission coefficient, heat sources applied to the bone/soft tissue boundary, no reflection, and no shear mode conversion represented heating in bone and soft tissues with good accuracy, while simplifying and speeding up simulations. Models generated for case-specific anatomy, incorporating finite element meshes representing the precise geometry of the tissues heated, made fairly accurate temperature predictions, as evidenced by favorable comparison with MRTI data.

3.7 Acknowledgements

I would like to thank Misung Han et al., who developed and performed the MR scans that monitored temperature within bone. I would also like to thank the rest of the MR thermometry groups at UCSF and Stanford, including Viola Rieke, Roland Krug, Eugene Ozhinsky, and Juan Plata.

Chapter 4

Parametric simulations for determination of appropriate treatment parameters for interstitial ultrasound ablation in the spine

4.1 Abstract

Purpose: The aim of this study is to determine appropriate treatment parameters for interstitial ultrasound ablation of tumors in and near bone, with a focus on the spine.

Methods: 2D axisymmetric parametric studies were performed to assess the impact of osteolytic lesion size, the thickness of bone protecting critical structures, and tumor attenuation values on appropriate treatment parameters, such as treatment duration and energy.

Results: 6-44 mm diameter soft tissue tumors surrounded by bone and blastic lesions up to 20 mm in diameter were fully ablated by 7 MHz interstitial ultrasound using 120-5,900 J with treatment durations of 0.4-15 min. The use of high powers and short treatment times, as opposed to low powers and long treatment times, resulted in lower thermal doses to nearby nerve tissue

when ablation of osteolytic tumors less than 20 mm in diameter were modeled. Simulations showed that a 4 mm thickness of bone or a 2 mm thickness of carbon dioxide could serve as sufficient insulation between a round tumor and nervous tissue, with full ablation of the tumor and no damage to the nerves.

Conclusions: Parametric studies indicate that tumors up to 44 mm in diameter in and near the spine can be treated using interstitial ultrasound in cases where nerves are separated from the tumor by at least 4 mm of bone or 2 mm of carbon dioxide.

The majority of this work, in conjunction with portions of Chapter 5, is summarized in a research paper by Scott et al. ("Interstitial ultrasound ablation of vertebral and paraspinal tumors: Parametric and patient specific simulations," 2014) [172].

4.2 Introduction

When tissue adjacent to bone is treated with interstitial ultrasound ablation, preferential heating occurs on the bone surfaces. This heating can significantly raise peak temperatures in some cases, and widen the ablated volume in others, as shown in Chapter 3. In homogenous soft tissues, heat deposition is dependent mainly on power, the distance from the applicator, the acoustic absorption coefficient, and blood perfusion. When interstitial ultrasound is directed at bone, the distance from the applicator to the bone surface is also a major factor in the resultant heat deposition distributions. To effectively treat osteolytic tumors in bone without obtaining unexpected temperature distributions, a thorough understanding of the appropriate powers and treatment times necessary to obtain the desired temperature distributions is needed.

In cases with tumors close to sensitive anatomy, such as osteolytic tumors within the vertebrae, guidelines for the preservation of critical anatomy are also necessary. In prior RF

ablation, laser ablation, and cryoablation studies, an insulating barrier of healthy bone or carbon dioxide has been shown to protect the spinal cord from damage [103, 104, 113]. During ultrasound ablation, these substances could provide acoustic as well as thermal insulation. However, preferential ultrasound absorption at the surface of the insulating bone would also have to be taken into account during treatment planning.

Thermal and acoustic properties of tumor tissue generally have significant influence on treatment guidelines. Blood perfusion is known to act as a heat sink, and may need to be taken into account during treatment planning [148-150]. Small pieces of bone remaining within an osteolytic tumor volume would likely increase acoustic absorption and scattering, raising the overall acoustic attenuation coefficient above that of a tumor with greater bone resorption. High acoustic attenuations may limit the volumes that can be treated.

Parametric studies were performed to determine the influence of the material properties of tissue and of various insulating techniques on temperature and thermal dose distributions during interstitial ultrasound ablation involving bone. Acoustic attenuation, blood perfusion, osteolytic tumor diameter, various target temperatures, and gaseous insulation of nervous tissues were considered. Guidelines for the powers and treatment times necessary to ablate lesions of various sizes with minimal thermal doses to sensitive nerves were developed.

4.3 Materials and Methods

4.3.1 Interstitial ultrasound applicators

The interstitial ultrasound applicators considered in this study contain a linear array of three 7 MHz cylindrical ultrasound transducers (10 mm L, 1.5 mm OD) with 360° angular sectors. The applicator is operated from within a 1.89 mm ID, 2.4 mm OD, water-cooled plastic catheter.

4.3.2 Biothermal and acoustic simulations

Heat transfer in tissues were modeled using Pennes bioheat transfer equation (Equation 2.1) [148] and Model B, as described in Section 2.3.4. The various tissue properties are summarized in Table 4.1. Attenuation over the catheter wall is assumed to be 43.9 Np/m/MHz [181]. Perfusion is assumed to reduce to zero at 300 EM43°C due to heating-induced microvascular stasis [142]. Thermal dose is calculated according to Sapareto and Dewey (Equation 2.2) [34].

Medium	Density (kg/m^3)	Velocity (m/s)	Attenuation (Np/m/MHz)	Thermal conductivity (W/m/°C)	Specific heat (J/kg/°C)	Perfusion rate ($kg/m^3/s$)
Muscle	1041 [59]	1576 [59]	5 [130]	0.5 [59]	3430 [59]	0.6923 [59]
Bone	1420 [59]	3260 [59]	105 [59]	0.38 [59]	1700 [59]	0.892 [176]
Spinal canal and nerves	1038 [59]	1542 [59]	12† [59]	0.515‡ [59]	3640‡ [59]	3.63 [202]
Carbon dioxide	1.66 [203]			0.018 [203]	871.5 [203]	0
Blood					3800 [59]	

Table 4.1 Material properties of tissues used in parametric models. Tumor tissue is assumed to have the same properties as muscle, but with a higher perfusion of 2.4 $kg/m^3/s$ [188, 204]. Values for nerve (†) and brain (‡) were used for some spinal canal properties.

Acoustic heat deposition from a tubular ultrasound source was modeled as a radially divergent intensity pattern well-collimated to the length of the transducer [65], as described in Equation 2.10. It was assumed that 50% of the applied electrical power was converted to acoustic output power [68, 195]. The power applied to a transducer sector was determined by a PI feedback controller (k_p = 0.375 W/K, k_i = 0.003 W/K/s) designed to maintain the maximum temperature in a region of interest (ROI) at a control temperature T_c. The ROI was defined as a 1 cm high cylindrical portion of the osteolytic tumor around the central transducer, ranging radially from 1 mm away from the outer surface of the catheter to the bone surface (Figure 4.1).

The acoustic intensity on the transducer surface (I_s) was limited to a realistic value 21.2 W/m^2 to protect the transducers from damage.

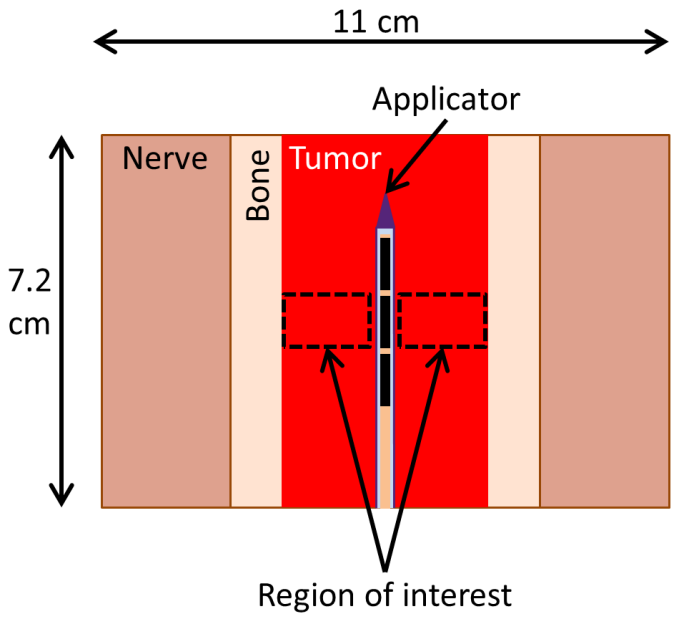

Figure 4.1 The geometry of the parametric simulations consisted of a 7.2 cm L, 11 cm OD cylinder with an applicator in the center. The applicator consists of three transducers (black) operated within a water-cooled catheter (purple). The tissues ablated could consist of only tumor tissue, tumor surrounded by bone, or tumor surrounded by bone surrounded by nervous tissue. There could also be a 2 mm thick layer of carbon dioxide gas between the nerve and bone. The temperature of a 1 cm long ROI in the center of the tumor was controlled to a maximum temperature T_c.

The absorption of incident waves by soft tissue and bone contributes significantly more to heat generation than absorption of reflected waves [170]. Ultrasound waves in bone are attenuated so rapidly that they do not penetrate deep enough for refraction or shear mode conversion to significantly affect temperature distributions [170]. Hence, this model does not consider reflection, refraction, or shear wave generation. The transmission coefficient ($\mathcal{T}_I$) into a given tissue can be approximated as [170]:

$$\mathcal{T}_I \equiv \prod_{i=2}^{n} \frac{I_i}{I_{i-1}} = \prod_{i=2}^{n} \frac{4\rho_i v_i \rho_{i-1} v_{i-1}}{(\rho_i v_i + \rho_{i-1} v_{i-1})^2} \qquad 4.1$$

where ρ is density (kg/m^3), v is the speed of sound (m/s) and the tissues that are traversed are numbered from 1 to n, beginning with the catheter. It is assumed that there is zero transmission through tissue/gas boundaries, and that there is 100% transmission through the catheter into tumors.

COMSOL Multiphysics 4.3 (Burlington, MA) was used to generate finite element meshes and to perform finite element analysis. Based upon convergence tests, maximum mesh sizes were limited to 0.4 mm on the inner surface of the catheter, 0.5 mm on heated bone surfaces, and 5 mm overall throughout the volume. An implicit transient solver with variable time stepping was used to calculate temperature and thermal dose, with maximum time steps of 10 s. Dirichlet boundary conditions fixed the temperature on the outer boundaries of the simulated volumes to 37°C. A convective boundary condition, Equation 2.3, was applied to the inner surface of the water-cooled catheter, with a heat transfer coefficient of 1000 W/m^2/°C, and a flow temperature of 22°C.

2D axisymmetric parametric studies were performed to determine the influence of preferential bone heating, osteolytic tumor diameter, tumor attenuation, tumor perfusion, gaseous insulation, and the insulating effects of bone on necessary treatment parameters. The geometries considered consisted of concentric cylinders of tumor, bone, and nerve tissue, with a 7 MHz applicator in the center (Figure 4.1). The ROI was considered ablated when its entire volume reached 240 EM43°C [33]. The geometric and treatment parameters of the three parametric studies performed are summarized in Table 4.2 and detailed below.

Parametric study	Effect of attenuation on thermal lesion size	Effect of bone on treatment parameters	Thermal dose on spinal cord insulated by bone
Tumor diameter	11 cm OD	0.6 – 5.0 cm OD	0.6 - 4.0 cm OD
Bone dimensions	N/A	11 cm OD	2, 3, 4 mm thick
CO_2 dimensions	N/A	N/A	0, 2 mm thick
Nerve diameter	N/A	N/A	11 cm OD
Tumor attenuation	1 - 300 Np/m/MHz	5 Np/m/MHz	5 Np/m/MHz
Control temperature	75, 85°C	75, 85°C	75, 80, 85°C
Tumor perfusion	2.4 kg/m^3/s	0.7, 2.4, 5 kg/m^3/s	2.4 kg/m^3/s
Treatment duration	5, 10, 15 min	Until target ablated	Until target ablated

Table 4.2 Geometric and treatment parameters for three parametric studies

4.3.3 Effect of attenuation on thermal lesion size

A study was performed to determine how tumor attenuation, which is influenced by osseous bone content, affects thermal lesion size. An applicator was placed in the center of a cylindrically shaped tumor (11 cm D, 7.2 cm L). The tumor attenuation was varied from 1 to 300 Np/m/MHz, a range encompassing the very low attenuations in some bodily fluids, the moderate to high attenuations expected in tumors with residual pieces of osseous bone, and the high attenuations observed in some bones [59]. To compare powers high enough ablate the full tumor but low enough to prevent water vaporization in tissue, the control temperature was set to 75 or 85°C. The thermal lesion diameter was defined as the maximum diameter of the 240 EM43°C contour [33] measured at the end of treatment.

4.3.4 Effect of bone on treatment parameters

To determine how bone adjacent to a soft tissue tumor affects the treatment parameters necessary to ablate an ROI, a parametric study was performed in highly osteolytic tumors of various diameters within bone. An applicator was placed in the center of a cylindrically shaped tumor

surrounded by bone (11 cm OD, 7.2 cm L). The power levels and treatment durations necessary to ablate the ROI, as well as the maximum bone temperature at the end of the ablation, were determined for various tumor diameters (0.6-5 cm, 7.2 cm L), tumor perfusions (0.7 – 5 kg/m^3/s), and control temperatures T_c (75 or 85°C).

4.3.5 Thermal dose on spinal cord insulated by bone

A study was performed to investigate the effects of bone and gas insulation, and to determine the powers and treatment times necessary to preserve sensitive tissue separated from a tumor by a layer of bone. An applicator was placed in a cylinder of tumor tissue (6-40 mm OD, 7.2 cm L), surrounded by a cylinder of bone (2-4 mm thick, 7.2 cm L), surrounded by a cylinder of nervous tissue (11 cm OD, 7.2 cm L). The maximum thermal dose on the canal was calculated for control temperatures of 75, 80, and 85°C. A 2 mm layer of carbon dioxide between the nerves and a 2 mm thick bone was considered for additional insulation of tumors 6-40 mm in diameter, with control temperatures of 75, 80, and 85°C.

4.4 Results

4.4.1 Effect of attenuation on thermal lesion size

Interstitial ultrasound ablation of tumors with a range of ultrasound attenuation coefficients was simulated. The diameters of the thermal lesions produced were measured for 5, 10, and 15 minute treatment times and for control temperatures of 75 and 85°C (Figure 4.2). In tumors with attenuations of 3 Np/m/MHz and higher, larger diameters (up to 60 mm) could be ablated in cases when the tumor had lower attenuations, when longer treatment times were used, and/or when higher control temperatures were used. However, at very low attenuations (below 3

Np/m/MHz), the volumes that could be ablated were smaller than in tissues with higher attenuations. At very high attenuations above about 80 Np/m/MHz, there was very little acoustic penetration, temperatures peaked within 1.5 mm of the catheter surface, and the maximum diameter that could be ablated varied relatively little with further increases in attenuation. Thus, in tumors with attenuations ranging from 1 to 100 Np/m/MHz, the lesion diameters created in 10 min (T_c = 85°C) varied 29.1 mm, while the thermal lesion diameters in tumors with attenuations of 200 to 300 Np/m/MHz only varied 0.9 mm (T_c = 85°C).

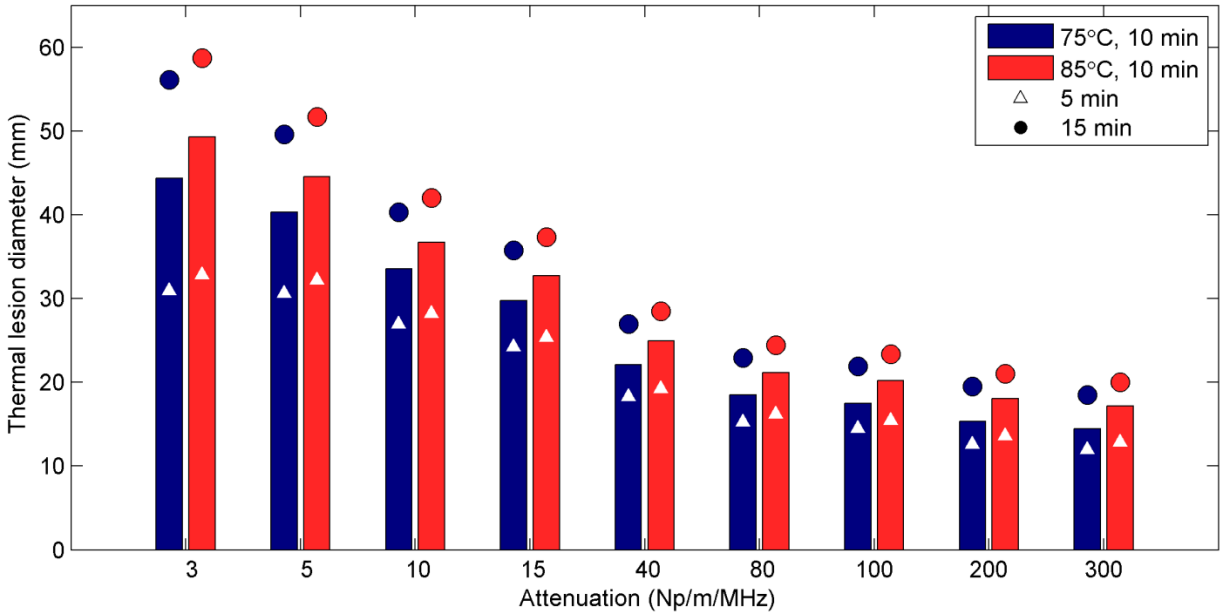

Figure 4.2 The diameter of thermal lesions in tumor tissue as a function of attenuation, ablation duration, and control temperature. Simulations for each attenuation value and each control temperature were performed for ablation durations of 5 min (triangle), 10 min (bar), and 15 min (circle).

4.4.2 Effect of bone on treatment parameters

Ablation of soft tissue lesions within bone (Figure 4.1) was simulated for a variety of lesion diameters to determine the necessary powers and ablation times, as well as the resulting bone temperatures (Figure 4.3). In tumors smaller than 12 mm D, the temperatures at the bone

surfaces were higher than those in the soft tissue closer to the applicator. The bone surface was the first portion of the tissues to reach 240 EM43°C, and then the adjacent soft tissues soon reached lethal temperatures. The tumors were quickly ablated in 21-83 s without reaching the control temperature. Peak bone temperatures (66.8-69.5°C for an 85°C set temperature and 6-12 mm D tumors) varied relatively little with tumor diameter. In 12-16 mm diameter tumors, simulations showed two temperature peaks of roughly equal height, one near the applicator and one at the bone surface. The temperatures at the bone surfaces were lower in tumors with wider diameters than in narrower tumors (Figure 4.3A). In tumors with 6-16 mm diameters, the intensities necessary to reach the set temperature increased roughly linearly with the distance between the applicator and the bone (Figure 4.3B), from 11.7 to 16.1 W/cm^2 (perfusion = 2.4 kg/m^3/s, T_c = 85°C), as more power was necessary to heat bone surfaces further away from the applicator to the control temperature. The necessary ablation times increased relatively slightly with increasing tumor diameters (Figure 4.3C), from 37 s to 81 s in a tumor with 2.4 kg/m^3/s perfusion and a set temperature of 75°C, and from 21 s to 54 s in a tumor with a 2.4 kg/m^3/s perfusion rate and a set temperature of 85°C. Up to 14.2% longer ablation durations were required in tumors with higher perfusions, resulting in bone temperatures up to 1.2°C higher. Otherwise, changes in tumor perfusion had little effect in of 6-16 mm OD tumors with low volumes and high bone heating.

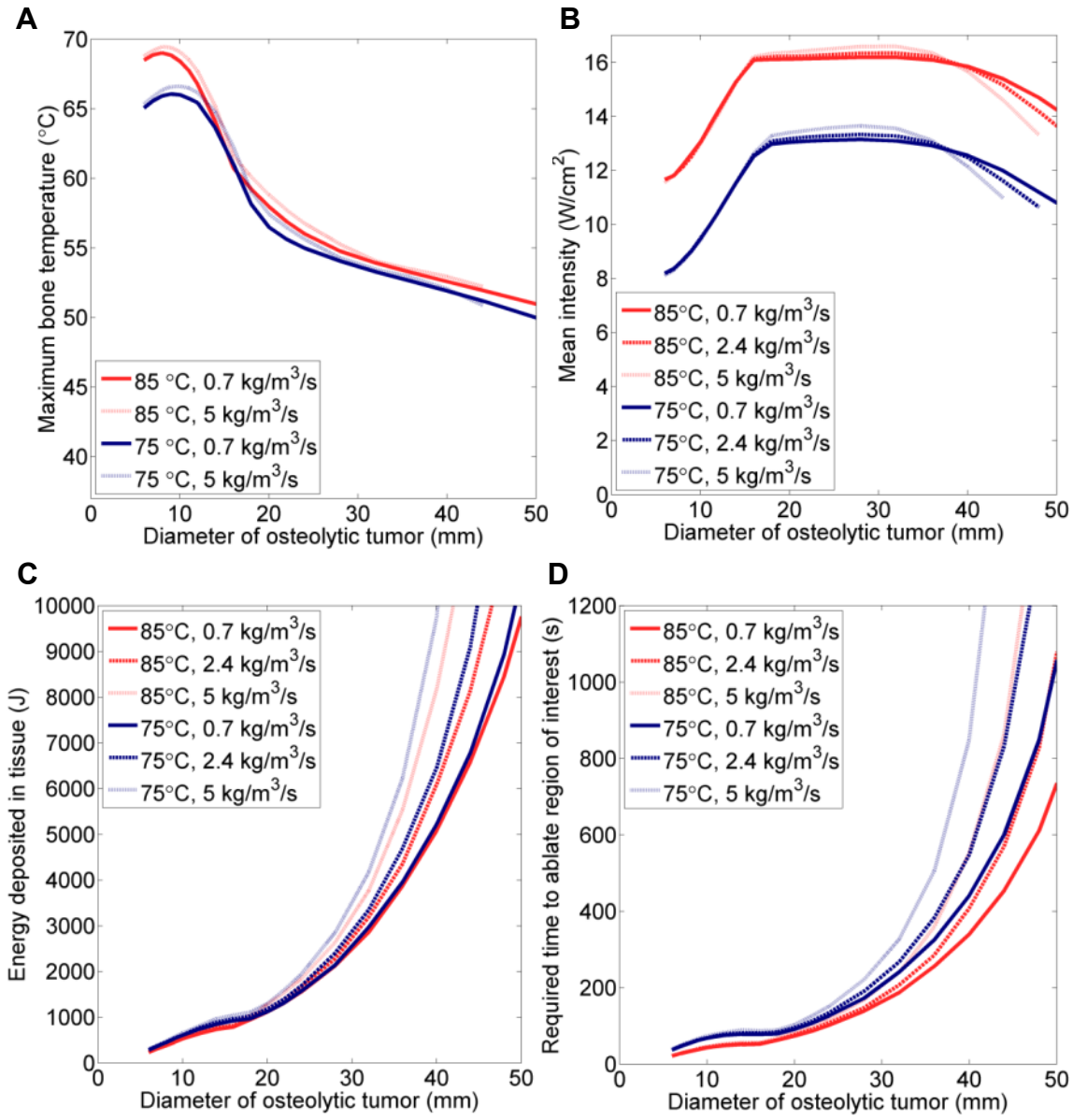

Figure 4.3 (A) The maximum bone temperature at the time ablation is completed, as a function of tumor diameter, for a variety of blood perfusion rates within the tumor and control temperatures. The mean acoustic intensity averaged over time (B), the total amount of energy deposited in the tissue (C), and the time necessary (D) to thermally ablate a tumor surrounded by bone are also shown.

Above tumor diameters of 16 mm, peaks in temperature near the applicator are higher than those at the bone surfaces (Figure 4.3). The maximum temperature, on which the power controller was based, occurred in the tumor tissue far from the bone surface, and the mean electrical power (Figure 4.3B) stayed roughly constant over tumor diameters from 16 to 36 mm

(12.2-12.9 W for a 75°C set temperature, and 15.2-15.6 W for an 85°C set temperature). The time necessary to ablate tumors over 16 mm in diameter, which had large volumes and less bone heating than smaller tumors, sharply increased with increasing tumor diameter (Figure 4.3C), from 52-88 s for a 16 mm tumor to over 1500 s for very large tumors. The applied powers decreased as temperatures approached steady state, reducing the overall acoustic intensities applied to ablate large tumors over 32 mm in diameter, by up to 2.1 W/cm^2 for a 44 mm tumor. The bone surfaces at the outer boundaries of the tumor were the last portions of the tissues to be ablated. The maximum bone temperature adjacent to tumors over 28 mm was 50-55°C, which is that necessary for ablation, with lower temperatures necessary for longer treatment times (Figure 4.3A).

The amount of energy (J) deposited within tissue (treatment time multiplied by mean power) followed trends similar to those of the required ablation times (Figure 4.3C), as the time to ablate the tissues varied much more than the powers applied. The most significant difference between the trends in energy and ablation duration was that the energy deposited within tissue did not level off in the 12-16 mm tumor diameter range, as power increased roughly linearly with diameter, while ablation time varied very little. 120-520 J were required to ablate tumors 6-16 mm in diameter with blood perfusion rates of 0.7-5 $kg/m^3/s$ perfusion rates and set temperatures of 75 or 85°C, and 390-8400 J were required to ablate tumors 16-44 mm in diameter with blood perfusion rates of 0.7-5 $kg/m^3/s$ perfusion rates and set temperatures of 75 or 85°C.

4.4.3 Thermal dose on spinal cord insulated by bone

The maximum thermal dose in nervous tissue was measured for a variety of tumor diameters, set temperatures, and thicknesses of insulating bone and gas (Figure 4.4). Gaseous insulation between the bone and the nerves was highly effective in protecting nervous tissue, decreasing the

thermal dose to the nerves by 3 orders of magnitude. Bone thickness also had a significant effect on thermal dose to nerves, with thicknesses over 4 mm generally adequate for limiting the thermal dose to nerves to 6 EM43°C. The thermal dose to nerves increased with tumor diameter by a factor of 4-15 over diameters of 6-12 mm, in which cases peak temperatures occurred on the bone surfaces. In tumor diameters from 12-16 mm, the bone temperatures sharply decreased (Figure 4.3A), as did thermal doses to nerve (Figure 4.4). Above 16-20 mm however, treatment time sharply increased with tumor size (Figure 4.3C), and thermal doses to nerves increased correspondingly.

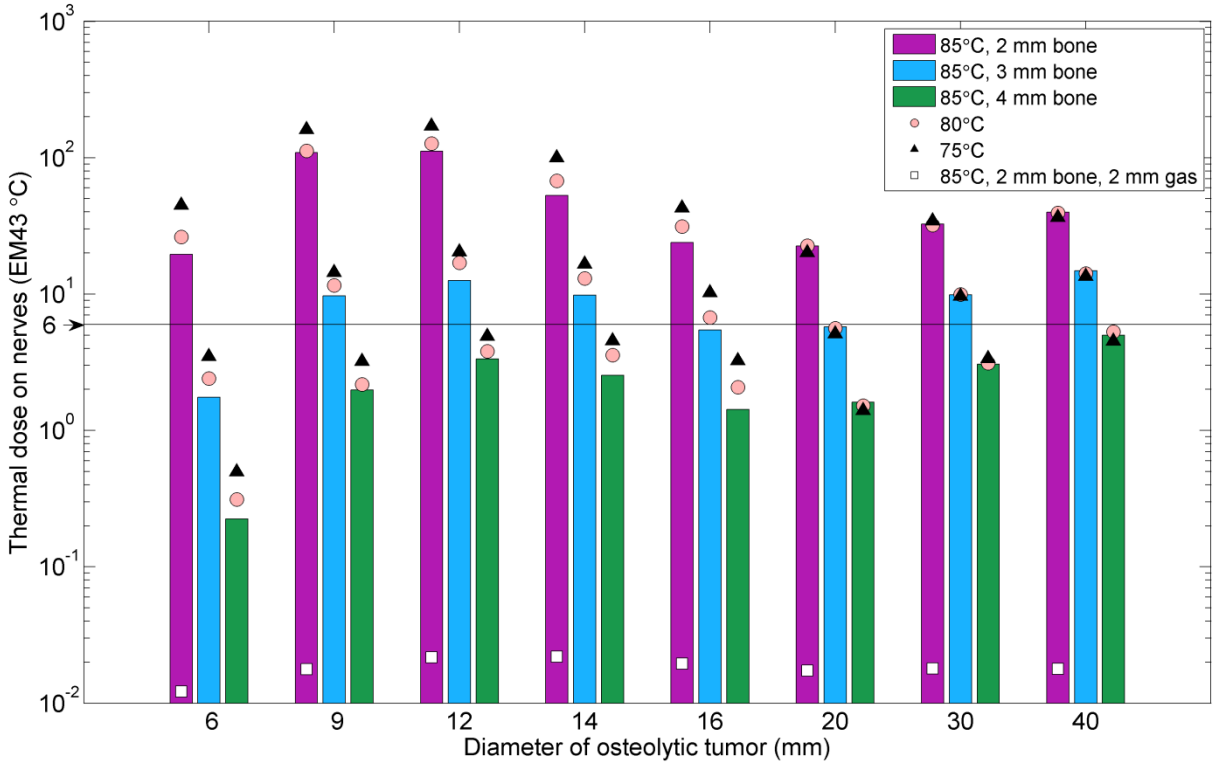

Figure 4.4 The maximum thermal dose to nervous tissue after ablation of a tumor insulated from the nerves by bone, for a variety of tumor diameters, insulation thicknesses, and control temperatures. Each tumor diameter and bone thickness was modeled with control temperatures of 85°C (bar), 80°C (circle), and 75°C (triangle).

For tumors under 20 mm in diameter, high powers (corresponding to high set temperatures) and short treatment durations produce thermal doses to nerves 1.5-2.3 times lower

than low powers and long treatment durations. Above 20 mm, the balance between power and time had far fewer effects, with high powers and short treatment durations producing thermal doses to the nerves 0.9-1.2 times higher than those produced with low powers and longer treatment times.

4.5 Discussion

Interstitial ultrasound produces high temperature peaks on bone surfaces, which significantly influences the necessary treatment parameters. This heating may potentially be used to lower treatment times and to ensure that the full volumes of osteolytic tumors are treated. Bone also provides thermal and acoustic insulation to tissues behind the surface of the bone. This simulation study was performed to determine appropriate treatment parameters and develop guidelines for interstitial ultrasound ablation of osteolytic bone tumors of various types and sizes.

Interstitial ultrasound ablation at 7 MHz is best suited for the ablation of highly osteolytic lesions. Above attenuations of about 80 Np/m/MHz, decreased acoustic penetration causes high temperature peaks very close to the applicator, limiting the powers that can be applied (Figure 4.2). Heating of outer portions of the tumors with attenuations above 80 Np/m/MHz is dominated by conduction. Thermal lesions of up to 20-24 mm in diameter can be created within 15 minutes at 7 MHz in bone tumors with high attenuations (Figure 4.2). Larger osteolytic tumors (42 – 52 mm diameter) with low acoustic attenuation coefficients of 5-10 Np/m/MHz can be treated in the same time frame (Figure 4.2).

Parametric studies indicate that highly osteolytic tumors up to 44 mm in diameter surrounded by bone can ablated within 10 minutes, and that 48-60 mm OD tumors surrounded by bone can be ablated within 25-27 minutes, depending on perfusion. These target sizes are

similar to those that can be treated with RF, laser, and cryoablation, and the treatment times are similar to or shorter than the treatment times of these other modalities [103, 106, 205]. Power limitations to prevent water vaporization resulted in large increases in the time necessary to treat larger tumors.

The treatment parameters applicable to highly osteolytic tumors surrounded by bone are strongly dependent on tumor diameter. Small osteolytic tumors 6-16 mm in diameter heat quickly, in 21-88 s, because of the high temperature peaks at the tumor/bone boundaries. Variations in perfusion in these tumors have little effect on treatment parameters, as the tumor volumes are small and are ablated very quickly. In tumors over 16 mm in diameter, the temperatures peaked in the soft tissue near the applicator, and the powers, which were linear with tumor diameter in smaller tumors, were limited to those that would not cause boiling. Because of power limitations and the higher volumes to be treated, the necessary treatment durations increase sharply with tumor diameter, from 52-88 s at 16 mm to 340-1631 s at 40 mm, depending on the powers applied and on blood perfusion in the tumor, which has more significant effects in large tumors. The relative height of the temperature peaks near the applicator and the peaks at the bone surface is the cause of the dependence of appropriate treatment parameters on the distance between the applicator and the bone.

To protect nearby critical anatomy, small osteolytic tumors under 16 mm in diameter were best heated with fast ablations and high intensities, rather than slowly with low intensities (Figure 4.4). These small tumors can heat quickly because of the high temperature peaks at the nearby tumor/bone boundaries (Figure 4.3A). In cases when the tumors were heated relatively slowly, simulations showed damage to nearby nerves (Figure 4.4), probably due to thermal conduction from the highly heated bone surfaces over time.

4.6 Conclusion

Parametric models indicated that highly osteolytic bone tumors up to 44 mm in diameter could be ablated with 7 MHz interstitial ultrasound within 10 minutes. Tumors up to 20-24 mm in diameter containing acoustically significant osseous deposits were ablated within 15 minutes. This study indicates that a layer of insulating bone at least 4 mm thick or carbon dioxide injection can serve to protect nervous tissue during complete ablation of highly osteolytic targets. When treating small tumors under 16 mm in diameter, faster ablations with high powers resulted in less nervous damage than slower ablations with lower powers.

Chapter 5

Interstitial ultrasound ablation of vertebral and paraspinal tumors: Patient specific simulations

5.1 Abstract

Purpose: The goals of this study are firstly, to theoretically assess the feasibility of interstitial ultrasound ablation of tumors in and near the spine using patient-specific models, and secondly, to identify potential energy delivery strategies.

Methods: 3D, transient, patient-specific finite element models of interstitial ultrasound ablation were generated for nine representative patient cases with tumors in or near the vertebrae. 3 and 7 MHz transducers, carbon dioxide dissection, and various applicator designs and placements were simulated.

Results: Preferential ultrasound absorption at bone surfaces allowed for faster, more effective ablations. 100% of the volumes of five simulated tumors located 4.3-14 mm from the spinal

canal and 94.6-99.9% of the volumes of four simulated tumors 0-4.5 mm from the spinal canal were ablated within 15 min without damaging critical nerves. Critical anatomy within 4–5 mm of the tumors was preserved by reducing the acoustic energy aimed towards these structures and/or through gaseous dissection.

Conclusions: Patient-specific studies demonstrated the feasibility of interstitial ultrasound ablation of paraspinal and highly osteolytic tumors within the spine.

The majority of this work, in conjunction with portions of Chapter 4, is summarized in a research paper by Scott et al. ("Interstitial ultrasound ablation of vertebral and paraspinal tumors: Parametric and patient specific simulations," 2014) [172]. A portion of the work done in this chapter and the techniques for the creation of patient-specific models described herein have been published by Scott et al. ("Interstitial ultrasound ablation of tumors within or adjacent to bone: Contributions of preferential heating at the bone surface," 2013) [171].

5.2 Introduction

Metastases to the vertebrae are highly prevalent, observed in 40% of terminal cancer patients [111]. The principle aims of treatment of vertebral metastases are pain relief, as well as restoration or preservation of both mechanical and neurological function [83]. Invasive approaches using RF, plasma-mediated RF, laser, microwave, and cryoablation have all been considered for the treatment of tumors in the spine [89, 93, 103-110], with RF ablation being the most common. Healthy bone between the tumor and the spinal canal has been found to thermally insulate the spinal cord during thermal ablation [104], and gaseous dissection has been found beneficial in cases with posterior wall defects [103, 113]. To mechanically stabilize

eroded or fractured bones and to provide further pain relief, radiotherapy and thermal ablation can both be performed in conjunction with vertebroplasty or kyphoplasty [83, 93, 94].

We propose the use of interstitial ultrasound ablation for the treatment of paraspinal tumors and highly osteolytic tumors within the spine. Unlike externally applied HIFU, interstitial ultrasound ablation does not require an acoustic window to the exterior of the body, and it can treat tumors within and shadowed by irregularly shaped vertebrae. Bone adjacent to a tumor can also serve to acoustically and thermally insulate sensitive structures near the tumor such as the spinal canal [104].

Numerical models can provide a more thorough understanding of the temperature distributions and the electric or acoustic fields during thermal ablation of the spine. With these goals and as a step towards treatment planning, Ryan *et al.* [168] and Bien *et al.* [169] have developed generalized models and a patient-specific model, respectively, of RF ablation in the spine.

The goal of this study is to implement acoustic and biothermal finite element models to assess the feasibility and to characterize the performance and potential advantages of interstitial ultrasound ablation of targets in and near the spine. To assess treatment delivery strategies, eleven 3D patient-specific models of interstitial ultrasound ablation of nine vertebral and paraspinal tumors of various shapes, sizes, and locations were developed. The tumor, bones, spinal canal, intervertebral discs, lungs, and major blood vessels were all modeled in order to determine how vascular cooling and disparate attenuation coefficients between tissues affect heating distributions. The models applied in this study are designed for the simulation of well-defined tumors that have uniform acoustic properties and are either adjacent to bone or have geographic bone destruction. As mixed and osteoblastic tumors containing acoustically

significant amounts of osseous bone are likely to have higher acoustic attenuation coefficients than more osteolytic lesions, both high and low frequency applicators were simulated for greater penetration into these tumors. This study evaluates applicator configurations, insertion strategies, and treatment parameters for tumors of various sizes, shapes, and locations in the vicinity of the spine.

5.3 Materials and Methods

5.3.1 Interstitial ultrasound applicators

The interstitial ultrasound applicators considered in this study contain a linear array of 1-4 cylindrical ultrasound transducers with 150-360° angular sectors. Transducer arrays operating at a nominal frequency of 7 MHz, a typical interstitial ultrasound configuration [65, 68], and 3 MHz were considered. The 7 MHz transducers (5, 10, or 15 mm length (L), 1.5 mm outer diameter (OD)) were operated inside a 1.89 mm inner diameter (ID), 2.4 mm OD, water-cooled plastic catheter. 3 MHz transducers (5, 10, or 15 mm L, 3.2 mm OD), considered for greater penetration into tumors with high ultrasound attenuation coefficients, were operated from within a 4 mm ID, 4.5 mm OD, water-cooled plastic catheter. Applicators either 360° sectors, two sectors of 150° and 210°, and two 180° sectors were considered. Between active transducer sectors, a 30° acoustically inactive dead zone is assumed [195].

5.3.2 Biothermal and acoustic simulations

Pennes bioheat transfer equation (Equation 2.1) was used to model heat transfer in heterogeneous tissues [148]. The various tissue properties are summarized in Table 5.1. At a thermal dose of 240 EM43°C, tissue is considered ablated, and at a thermal dose of 300 EM43°C, blood

perfusion is assumed to reduce to zero. Thermal dose is calculated according to Sapareto and Dewey [34]. Acoustic heat deposition in tissue is modeled using Model B (Equations 2.10 & 4.1), which does not consider reflection, refraction, or shear wave generation, as detailed in Section 2.3.4. It is assumed that there is zero transmission through tissue/gas boundaries, and that the catheter has the same acoustic properties as osteolytic tumors, for complete acoustic transmission into osteolytic tumors. The discretization and calculation of heat deposition in irregularly shaped tissue volumes is described in detail in Appendix A.

Medium	**Density (kg/m^3)**	**Velocity (m/s)**	**Attenuation (Np/m/MHz)**	**Thermal conductivity (W/m/°C)**	**Specific heat (J/kg/°C)**	**Perfusion rate ($kg/m^3/s$)**
Muscle	1041 [59]	1576 [59]	5 [130]	0.5 [59]	3430 [59]	0.6923 [59]
Bone	1420 [59]	3260 [59]	105 [59]	0.38 [59]	1700 [59]	0.892 [176]
Spinal canal and nerves	1038 [59]	1542 [59]	12† [59]	0.515‡ [59]	3640‡ [59]	3.63 [202]
Intervertebral disc	1165* [59]	1627** [206]	53.3* [59]	0.61 [207]	2713 [207]	0 [208]
Carbon dioxide	1.66 [203]			0.018 [203]	871.5 [203]	0
Blood					3800 [59]	

Table 5.1 Material properties of tissues used in patient-specific models. Tumor tissue is assumed to have the same properties as muscle, but a higher perfusion of 2.4 $kg/m^3/s$ [188, 204]. Values for nerve (†) and brain (‡) were used for some spinal canal properties. Values for tendon (*) and cartilage (**) were used for some intervertebral disc properties. The ultrasound attenuation coefficient of the catheter is assumed to be 43.9 Np/m/MHz [181].

The power applied to a transducer sector was either constant over time or determined by a PI feedback controller (k_p = 0.375 W/K, k_i = 0.003 W/K/s) designed to maintain a maximum temperature in the tumor and adjacent bone of 85°C. The acoustic intensity on the transducer surface (I_s) was limited to 21.2 W/m^2, above which the transducers could be damaged.

5.3.3 Finite element analysis

Finite element analysis was performed using COMSOL Multiphysics 4.3 in conjunction with MATLAB (MathWorks, Natick, MA). Based upon convergence tests, the maximum mesh sizes on the inner catheter surfaces and on heated bone surfaces were limited to 0.4 mm and 0.5 mm, respectively. The mesh size gradually increased from the catheter surface, for a maximum overall mesh size throughout the volume of 5 mm. Temperature and thermal dose were calculated by an implicit transient solver with variable time stepping (maximum 10 s). Dirichlet boundary conditions constrained the temperature on the outermost tissue boundaries to 37°C. Convective boundary conditions were applied to inner catheter surfaces, major blood vessels, respiratory passages, and skin surfaces as follows:

$$-\hat{n} \cdot (-k\nabla \mathrm{T}) = h(T_f - T) \qquad (4)$$

where $\hat{n}$ is the normal unit vector to the boundary, h is the heat transfer coefficient (W/m^2/°C), and T_f (°C) is the fluid temperature, as specified in Table 5.2.

Surface	$\boldsymbol{h}$ **(W/m^2/°C)**	$\boldsymbol{T_f}$ **(°C)**
Catheter	1000	22
Aorta	598	37
Vena cava	391	37
Carotid artery & jugular vein	970	37
Lungs & respiratory passages	40 [193]	34 [209]
Skin	10.5 [193, 194]	22

Table 5.2 Heat transfer coefficients and fluid temperatures for convective flow boundaries. Heat transfer coefficients for blood vessels are calculated based upon vessel diameters and flow rates [210-212] as described by Haemmerich et *al*. [213].

5.3.4 Patient-specific models

11 patient-specific models were developed to theoretically assess the feasibility and performance of interstitial ultrasound ablation in 9 tumors within and near the spine and to investigate treatment delivery strategies. Tumors were either segmented from 3D CT image sets

or were based on the shapes, sizes, and positions of tumors (Table 5.3) observed in patient data or the literature [97, 214-217]. Image segmentation and the generation of patient-specific FEM meshes was performed using the Mimics Innovation Suite (Figure 5.1). The FEM meshes were imported into COMSOL, where finite element analysis was performed. Powers and applicator configurations were determined iteratively, with the initial configuration based on the size of the tumor, the distance from the transducers to the bone surfaces, and the distance from the tumor to sensitive anatomy. At the end of each treatment, power and catheter cooling were shut off, and conduction through the tissues over another 10 minutes was modeled.

Case	**Tumor location**	**Tumor type**	**Tumor dimensions (mm)**	**Tumor volume (mm^3)**	**Distance from tumor to critical structures (mm)**
1	Between C4 and C5	Paraspinal	20 L, 19 OD 20 x 17 x 16	3200	SC: 6.8
2	T5, left transverse process	Osteolytic	20 L, 22 OD 20 x 20 x 19	4400	SC: 14, Lu: 6.0, A: 32
3	L3, transverse process	Osteolytic	33 L, 27 OD 29 x 28 x 20	8100	SC: 4.5
4a-b	L2, pedicle, vertebral body, spinal canal	Osteolytic	43 L, 27 OD 43 x 27 x 27	9200	SC: 0, A: 28, VC: 22
5	C5, vertebral body	Osteolytic	10 L, 10 OD 10 x 10 x 10	520	SC: 2.6, F: 4.5, Tr: 15, E: 15, C: 18
6	L1, vertebral body	Osteolytic	25 L, 13 OD 25 x 13 x 13	2040	SC: 4.3, A: 13
7	L1, anterior vertebral body	Osteolytic	23 L, 27 OD 25 x 27 x 18	6600	SC: 13, A: 10, VC: 26
8	S1	Osteolytic	24 L, 17 OD 24 x 17 x 15	3200	SC & N: 2.9
9a-b	Iliac bone	A: Osteolytic B: Mixed	32 L, 18 OD 32 x 18 x 15	4900	SC & N: 12

Table 5.3 Location, bone content, and size of tumors considered in patient-specific models.
SC: Spinal canal, Lu: Lung, A: Aorta, VC: Vena cava, F: Transverse foramen, Tr: Trachea, E: Esophagus, C: Carotid artery and internal jugular vein, N: Spinal nerves
Tumor length and diameter are defined in relation to the applicator axis. Next the dimensions of a rectangular prism around the tumor are listed.

To investigate the capacity of injected carbon dioxide to insulate the spinal canal during interstitial ultrasound ablation, ablation of a tumor with a posterior wall defect was considered with and without carbon dioxide dissection in Cases 4a and 4b, respectively. The gas bubble was added to the 3D surfaces mesh of the anatomy and included in the FEM mesh. Separate feedback controllers with identical parameters determined the powers applied to each transducer. Power to each transducer was permanently shut off 5 seconds after the tumor tissue around it was fully ablated, 5 seconds after the portion of the spinal canal next to it reached 2 EM43°C (to prevent nervous injury), or after 15 minutes of treatment, whichever occurred first. To ablate tissue adjacent to the water-cooled catheter via conduction, whenever power to a transducer was shut off, cooling flow and power to all other transducers were also shut off for 10 seconds.

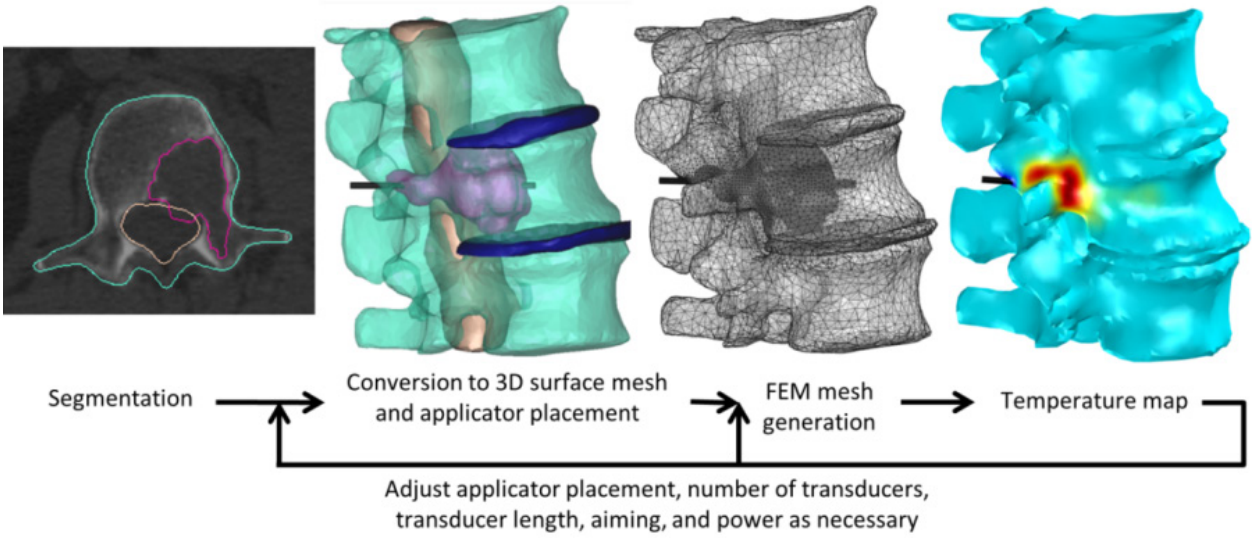

Figure 5.1 Process by which patient-specific simulations are performed.

A low frequency transducer (3 MHz) was considered for greater penetration into a mixed osteolytic and osteoblastic lesion, which had higher bone content, and was thus likely to have a higher acoustic attenuation coefficient, than purely osteolytic lesions. In Cases 9a and 9b, two interstitial ultrasound ablations of the same mixed osteolytic and osteoblastic tumor, one at 7

MHz and the other at 3 MHz, respectively, were simulated. The tumor was assumed to have the same acoustic attenuation coefficient as bone, with all other tissue properties assumed to be the same as those of osteolytic tumors. Applied powers were determined by the previously described PI feedback controller. Power and cooling flow were shut off 100 s after the entire tumor had reached at least 1000 EM43°C. Identical applicator positions and control parameters were used for both ablations.

5.4 Results

11 patient-specific models were created to simulate interstitial ultrasound ablation of 9 tumors invading paraspinal spaces (Case 1), transverse processes (Cases 2-3), vertebral bodies (Cases 4-8), and the ilium (Case 9). The amount of tumor tissue that was ablated, as well as the temperatures and thermal doses in nearby sensitive anatomy, is indicated in Table 5.4. Figure 5.2 - Figure 5.10 show the resulting temperature and thermal dose distributions in 2D slices and 3D anatomical volumes. The inner thermal dose contours correspond to 240 EM43°C, which is considered a lethal thermal dose [33], and the outer thermal doses contour correspond to 6 EM43°C, a conservative margin below which sensitive tissues should be undamaged [112]. Unless otherwise indicated, all thermal doses reported and pictured were recorded at the end of a 10 minute cooling period after the ablation. The locations of the tumor (t), vertebrae (v), spinal canal (sc), spinal nerves (n), intervertebral discs (d), Ilium (i), ribs (r), aorta (a), vena cava (vc), and lung (lu) are indicated in the figures. All treatment parameters, including the number, length, and sector angle of the transducers, the acoustic intensity, and the treatment times, are specified in Table 5.4.

Case	Sector length and angle	Acoustic intensity (W/cm^2)	Treatment time (s)	% Target ablated	Max temperature and dose on sensitive anatomy, volume canal & nerves over 6 EM43°C
1	2 x 1 cm, 360°	10.6	300	100%	SC: 42.1°C, 0.9 EM43°C, 0 mm^3
2	2 x 1 cm, 360°	11.7	300	100%	SC: 38.6°C, 0.0 EM43°C, 0 mm^3 Lu: 45.5°C, 18.7 EM43°C A: 37.0°C, 0 EM43°C
3	2 x 1.5 cm, 180° & 180°	0 & 12.2, 8.1 & 14.9	540	94.6%	SC: 42.2°C, 1.8 EM43°C, 0 mm^3
4a	4 x 1 cm, 360°, CO_2 insulation	7.8, 9.0, 8.1, 7.1*	520, 640, 380, 190	99.9%	SC: 43.5°C, 3.1 EM43°C, 0 mm^3 A: 37.1°C, 0 EM43°C VC: 37.3°C, 0 EM43°C
4b	4 x 1 cm, 360°, no CO_2 insulation	7.7, 10.2, 11.9, 8.3*	900, 220, 30, 80	59.7%	SC: 48.1°C, 12.5 EM43°C, 3.2 mm^3 A: 37.1°C, 0 EM43°C VC: 37.3°C, 0 EM43°C
5	1 x 1 cm, 210° & 150°	7.6 & 6.4	230	96.3%	SC: 45.0°C, 6.9 EM43°C, 0.03 mm^3 E: 37.0°C, 0 EM43°C, 0 mm^3 F: 46.2°C, 15.2 EM43°C Tr: 37°C, 0 EM43°C C: 37.1°C, 0 EM43°C
6	2 x 1.5 cm, 360°	6.2	180	100%	SC: 43.6°C, 2.5 EM43°C, 0 mm^3 A: 37.4°C, 0 EM43°C
7	2 x 1 cm, 360°	8.6*	600	100%	SC: 39.4°C, 0.1 EM43°C, 0 mm^3 A: 39.0°C, 0.1 EM43°C VC: 37.1°C, 0 EM43°C
8	1x1.5 cm, 180° & 180°	0-15.3 & 9.5-17.8	300	99.9%	SC & N: 44.0°C, 3.6 EM43°C, 0 mm^3
9a	0.5, 1.5, 1.5 cm, 360°, 7 MHz	8.0*	930	100%	N: 39.6°C, 0.1 EM43°C, 0 mm^3
9b	0.5, 1.5, 1.5 cm, 360°, 3 MHz	5.9*	390	100%	N: 39.8°C, 0.1 EM43°C, 0 mm^3

Table 5.4 Treatment parameters and results for patient-specific models.
*Time-average of acoustic intensities determined by a feedback controller
SC: Spinal canal, Lu: Lung, A: Aorta, VC: Vena cava, F: Transverse foramen, Tr: Trachea, E: Esophagus, C: Carotid artery and internal jugular vein, N: Spinal nerves
If different, intensities on two sectors of a single transducer are separated by an ampersand. In cases where intensities and/or ablation durations of individual transducers are varied, values are listed in order, starting with the tip transducer and separated by commas.

Preferential ultrasound absorption occurred on bone surfaces at the outer boundaries of osteolytic and paraspinal tumors. In Cases 1 and 2, in which power was applied uniformly to 360° transducers, simulations showed greater temperature rises in portions of the tumors adjacent to bone (Figure 5.2B, Figure 5.3B). To compensate for preferential bone heating in Cases 3 and 4, lower powers and/or shorter ablation times were applied to transducers and sectors near bone surfaces (Figure 5.4B, Figure 5.5A-B). In Case 4, the 360° applicator was not placed in the center of the tumor, and higher temperatures were calculated on bone surfaces that were closer to the applicator (Figure 5.5A). To take advantage of preferential ultrasound absorption by bone and to ensure that it does not cause any significant portions of the tumor to be shadowed, the applicator was placed in a location that allows for an acoustic window to all tumor tissue, such as in the center of the tumor.

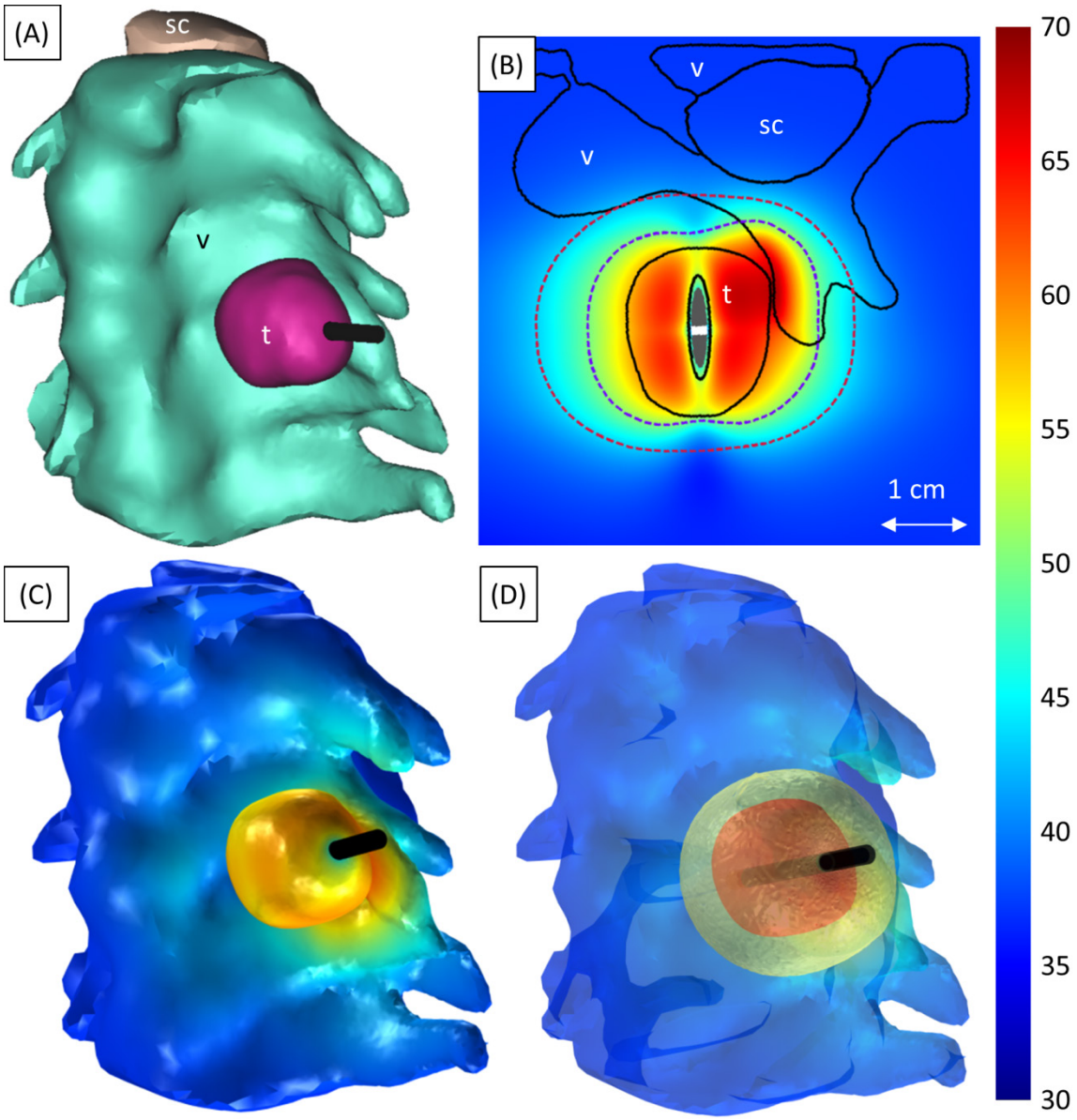

Figure 5.2 Modeled ablation of a paraspinal tumor adjacent to the cervical vertebrae C4 and C5 (Case 1). (A) 3D anatomical surface meshes used to create the finite element mesh. (B) The 240 (dashed violet) and 6 (dashed crimson) EM43°C contours in an axial slice atop a temperature map (°C). The transducer positions are shown in gray. (C) 3D temperature map . (D) A yellow cloud indicates the 240 EM43°C contour around the tumor (red). A temperature map is shown on the bone and spinal canal. The applicator is shown in black in (C) and (D).

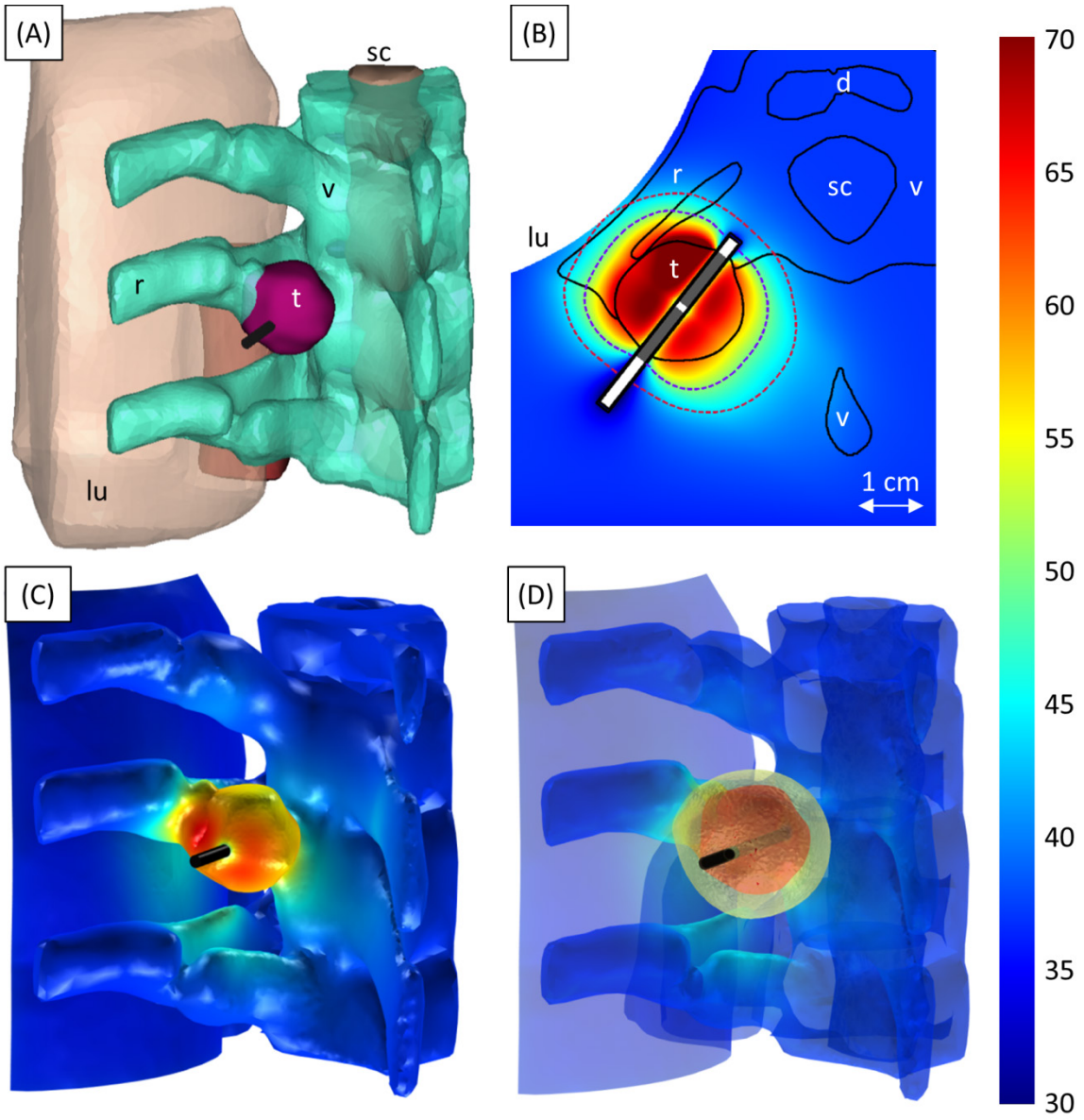

Figure 5.3 Modeled ablation of an osteolytic tumor invading the left transverse process of T5 (Case 2). (A) 3D anatomical surface meshes used to create the finite element mesh. (B) The 240 (dashed violet) and 6 (dashed crimson) EM43°C contours in an axial slice atop a temperature map (°C). The transducer positions are shown in gray. (C) 3D temperature map. (D) A yellow cloud indicates the 240 EM43°C contour surrounding the tumor (red). A temperature map is shown on the other tissues. The applicator is shown in black in (C) and (D).

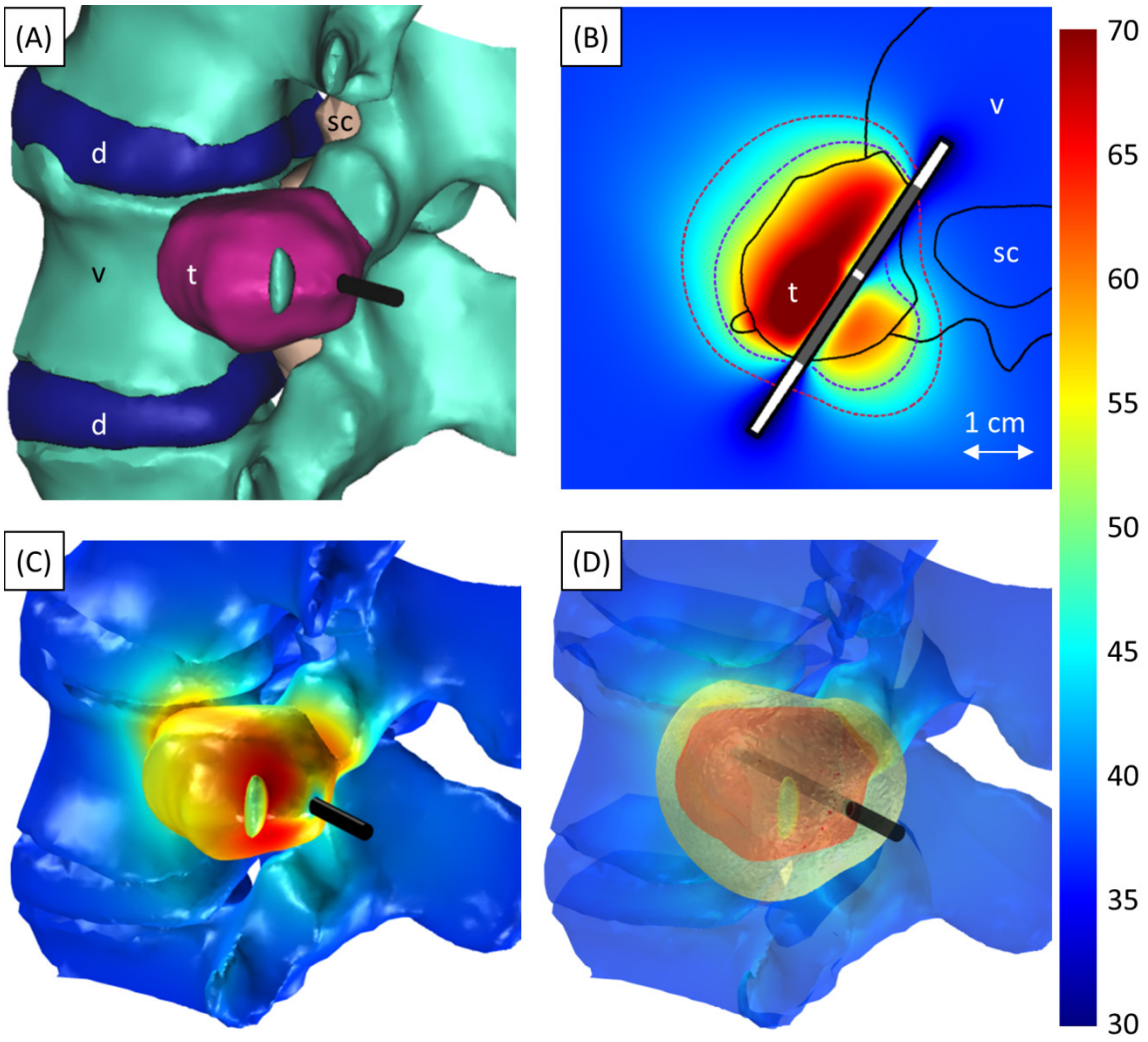

Figure 5.4 Modeled ablation of an osteolytic tumor invading the left transverse process of L3 (Case 3). (A) 3D anatomical surface meshes used to create the finite element mesh. (B) The 240 (dashed violet) and 6 (dashed crimson) EM43°C contours in an axial slice atop a temperature map (°C). The transducer positions are shown in gray. (C) 3D temperature map. (D) A yellow cloud indicates the 240 EM43°C contour surrounding the tumor (red). A temperature map is shown on the other tissues. The applicator is shown in black in (C) and (D).

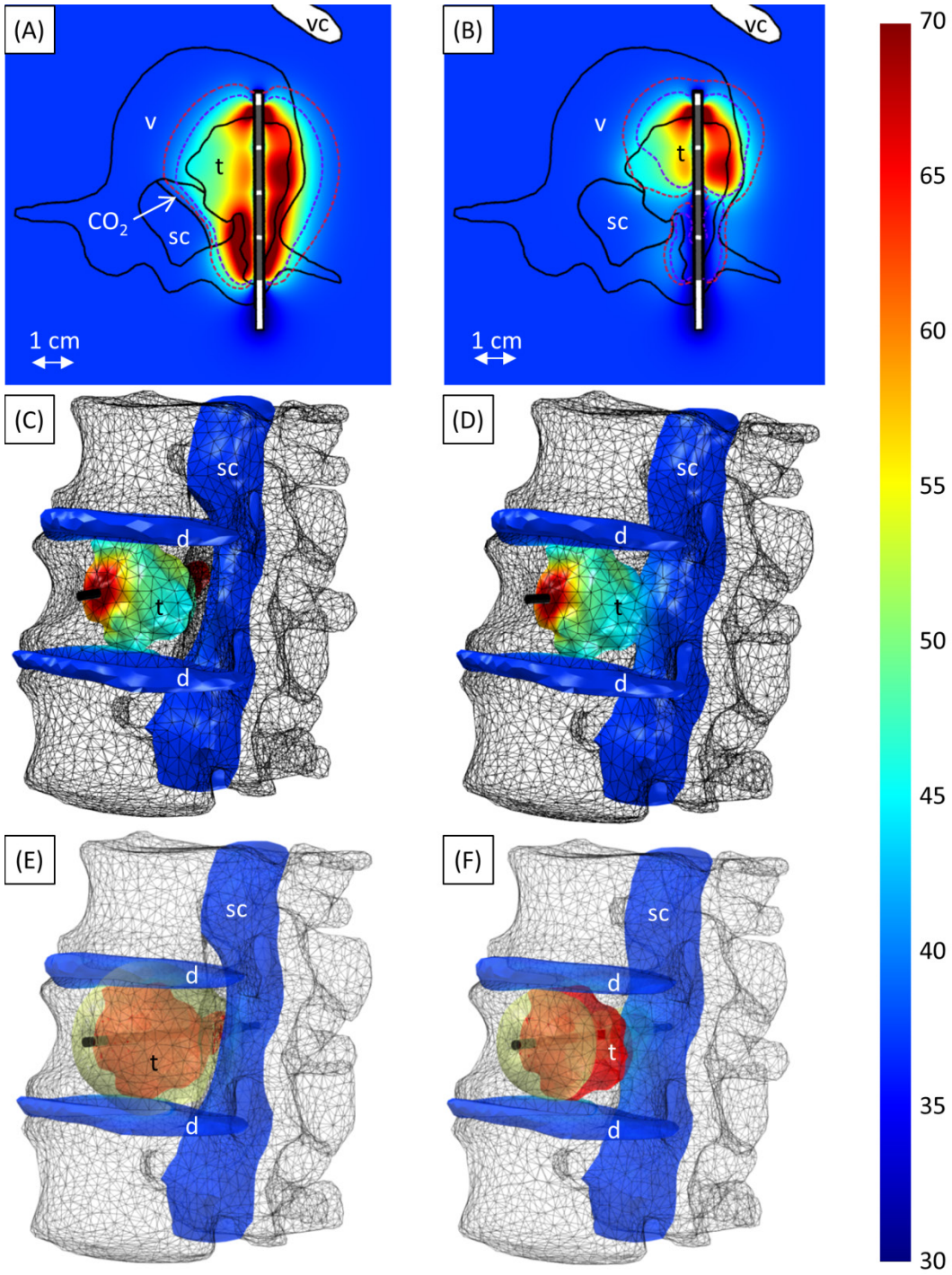

Figure 5.5 Ablation of a tumor invading the vertebral body and spinal canal at level L2. (A), (C), and (E) show ablation with carbon dioxide dissection (Case 4a). (B), (D), and (F) show ablation without carbon dioxide dissection (Case 4b). (A,B) The 240 (dashed violet) and 6 (dashed crimson) EM43°C contours in axial slices atop a temperature map (°C). The transducer positions are shown in gray. (C,D) 3D temperature map. (E,F) Yellow clouds indicate the 240 EM43°C contours surrounding the tumors (red). Temperature maps are shown on the other soft tissues. The applicator is shown in black and the bone surface is shown as a black mesh in (C-F).

The narrow 10-13 mm diameter tumors surrounded by bone that were simulated in Cases 5 and 6 (Figure 5.6 - Figure 5.7) were treated with lower acoustic intensities and ablation durations (6.2-7.6 W/cm^2, 180-230 s) than other larger tumors (8.0-17.8 W/cm^2, 300-930 s). In these small tumors, the temperatures peaked in the bone at the tumor boundaries, which heated quickly, rather than immediately adjacent to the applicators. Although the tissue adjacent to the water-cooled catheters did not reach lethal temperatures during the ablation, heat quickly conducted to these narrow regions after power and cooling flow were shut off, ablating the innermost portions of the tumor.

Applicators placed so that the spinal canal was not directly heated by ultrasound produced little heating in the spinal canal. When the applicator was placed perpendicular to the canal surface in Cases 1-2 with the transducers 7-14 mm away from the canal (Figure 5.1-Figure 5.2), the spinal canal was heated to only 38.6-42.1°C and 0.02-0.1 EM43°C. In Case 7, the applicator ran past the spinal canal through the pedicle, and the transducers were positioned so the canal would not be in the direct path of the acoustic energy (Figure 5.8). The spinal canal, insulated from the tumor by 13 mm of bone, was only heated to 39.4°C with a maximum thermal dose of 0.1 EM43°C. Although the 240 EM43°C contour extended 16.8 mm outward radially from the transducer surface, it only extended 2.8 mm behind the transducer array towards the spinal cord (Figure 5.8B). Interstitial ultrasound ablation produced a well-controlled heating pattern with deep radial penetration through soft tissues and the highly osteolytic lesion, which only extending a few millimeters past the length of the transducers.

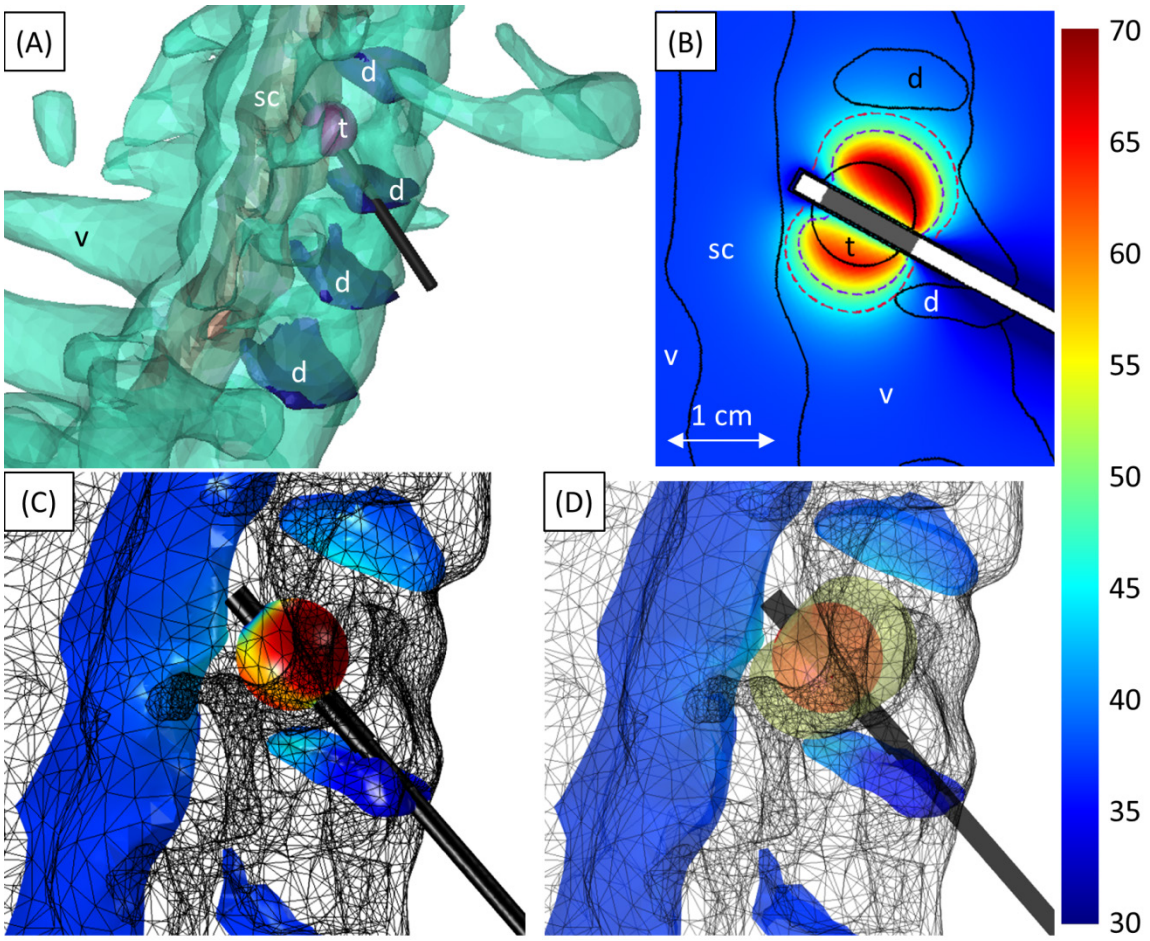

Figure 5.6 Modeled ablation of a small osteolytic tumor invading the vertebral body of C5 (Case 5). (A) 3D anatomical surface meshes used to create the finite element mesh. (B) The 240 (dashed violet) and 6 (dashed crimson) EM43°C contours in a vertical slice through the applicator atop a temperature map (°C). The transducer position is shown in gray. (C) 3D temperature map. (D) A yellow cloud indicates the 240 EM43°C contour surrounding the tumor (red). A temperature map is shown on the other soft tissues. The applicator (black cylinder) and bone surface (gray mesh) are also shown in (C) and (D).

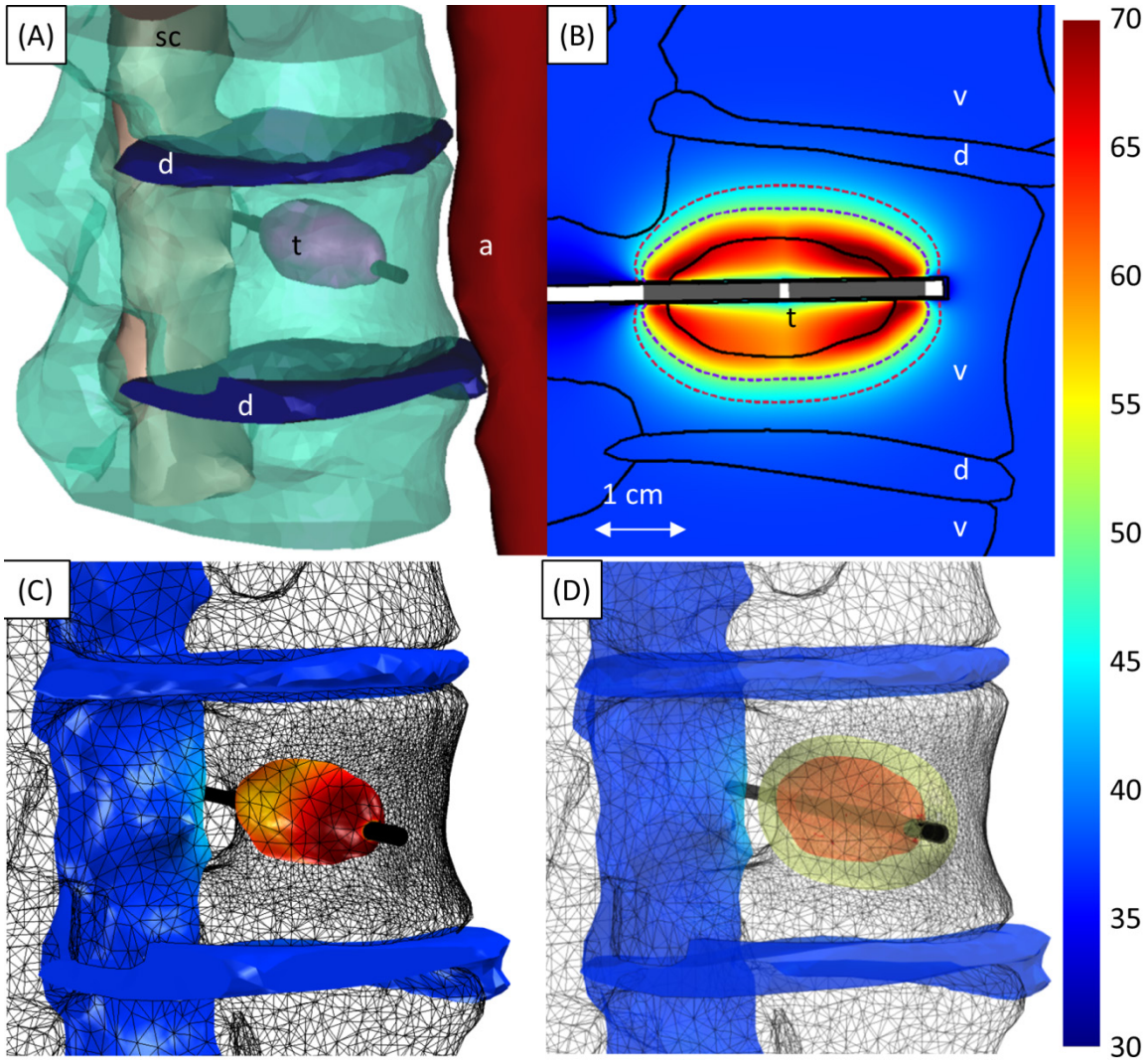

Figure 5.7 Modeled ablation of a narrow osteolytic tumor invading the vertebral body of L1 (Case 6). (A) 3D anatomical surface meshes used to create the finite element mesh. (B) The 240 (dashed violet) and 6 (dashed crimson) EM43°C contours in a vertical slice through the applicator atop a temperature map (°C). The transducer positions are shown in gray. (C) 3D temperature map. (D) A yellow cloud indicates the 240 EM43°C contour surrounding the tumor (red). A temperature map is shown on the other soft tissues. The applicator (black cylinder) and bone surface (gray mesh) are also shown in (C) and (D).

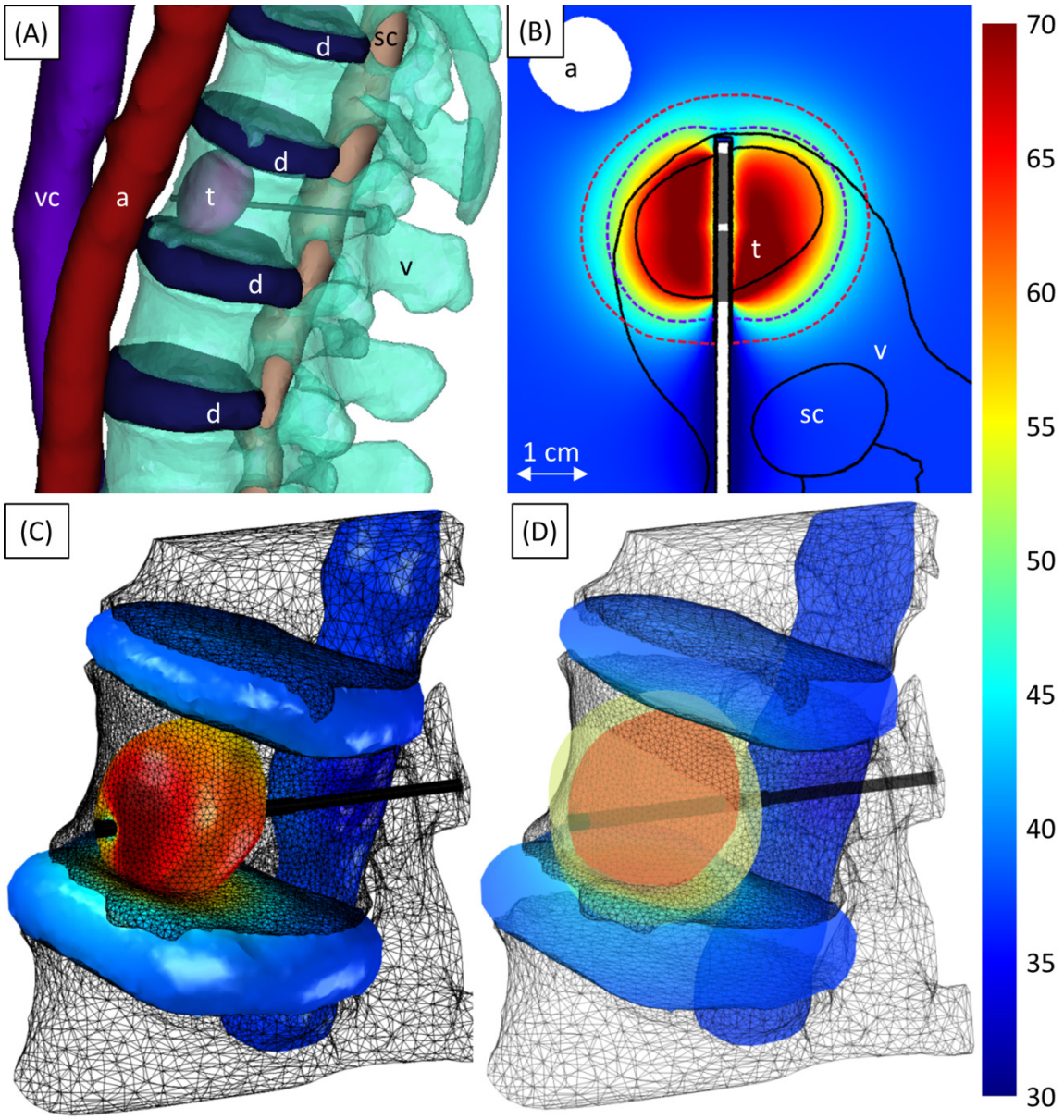

Figure 5.8 Ablation of an osteolytic tumor invading the anterior portion of the L1 vertebral body (Case 7). (A) 3D anatomical surface meshes used to create the finite element mesh. (B) Temperature (°C) at the end of treatment in an axial slice through the applicator. The 240 (dashed violet) and 6 (dashed crimson) EM43°C contours 10 minutes after treatment, as well as transducer positions (gray) are also shown. (C) The temperature on the spinal canal, intervertebral discs, and tumor at the end of treatment. (D) A yellow cloud indicates the 240 EM43°C contour surrounding the tumor (red). A temperature map at the end of treatment is shown on the other soft tissues. The applicator (black cylinder) and bone surface (black mesh) are also shown in (C) and (D).

In Case 4a, the spinal canal was protected by gaseous dissection (Figure 5.5A, C, E). A carbon dioxide bubble insulated and displaced the spinal cord from a tumor that invaded the

spinal canal. Simulations calculated that 99.9% of the tumor was ablated and that the spinal cord was protected, reaching a maximum temperature and thermal dose of 43.5°C and 3.1EM43°C. Without gas present (Case 4b) only 60% of the tumor could be ablated, and the canal reached 48.1°C and 12.5 EM43°C (Figure 5.5B, D, F).

Angularly sectored transducers were used in Cases 3, 5, and 8 to limit heating of the spinal cord. In Case 3 and in the last 50 s of Case 8, power to the transducer sectors pointing towards the spinal cord was kept off, and power was applied to only sectors pointing away from the spinal cord (Figure 5.4B and Figure 5.9E). In Case 5, 7.6 W/cm^2 was applied to the sector directed away from the spinal cord, while 6.4 W/cm^2 was applied to the sector facing towards the spinal cord (Figure 5.6), for a maximum temperature and thermal dose of 45.0°C and 6.9 EM43°C on the spinal canal.

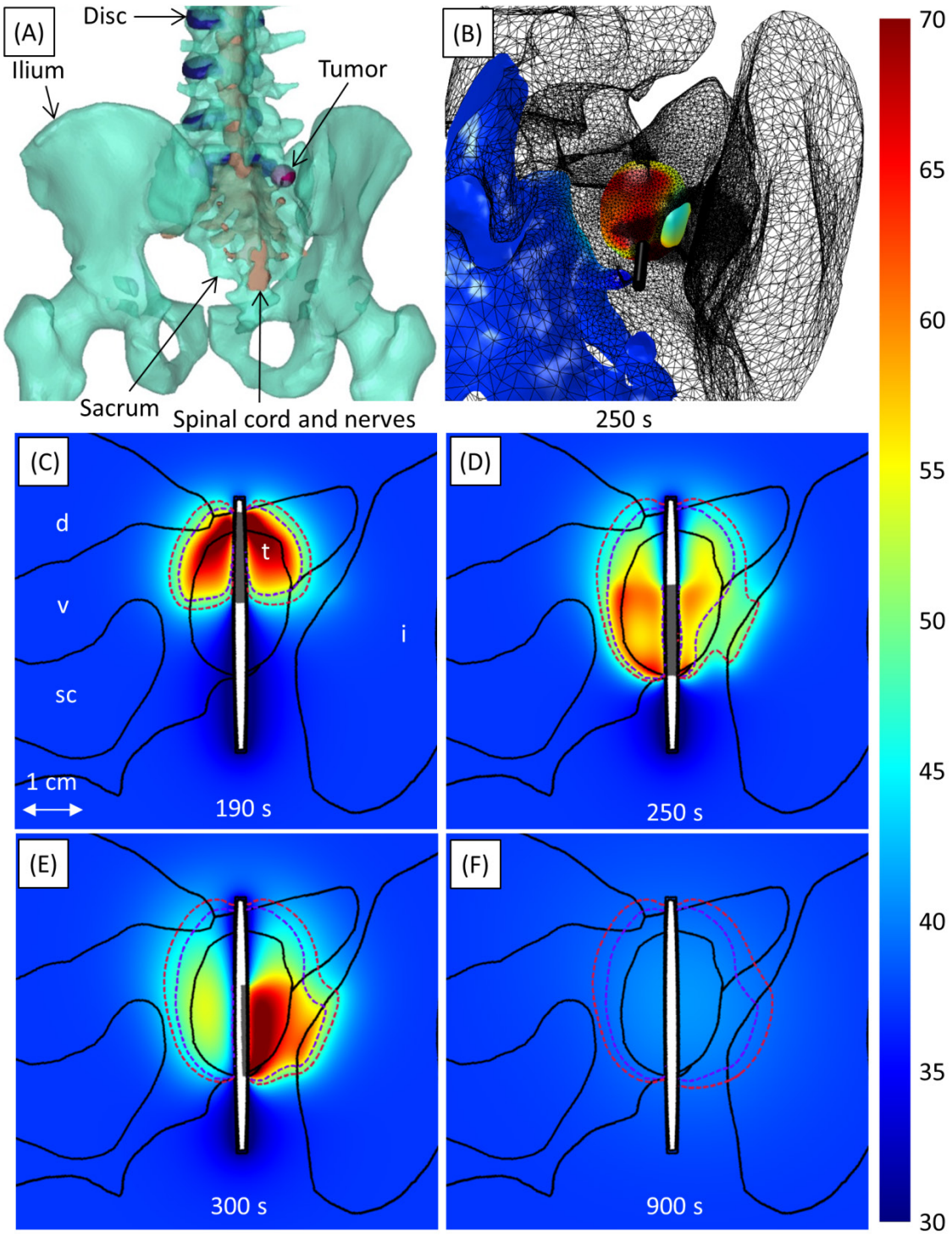

Figure 5.9 Ablation of a tumors invading S1 in Case 8. (A) 3D anatomical surface meshes used to create the finite element mesh. (B) The temperature (°C) on the spinal canal and tumor 250 s into the treatment. The applicator (black cylinder) and bone surface (black mesh) are also shown. (C-F) show temperature at a given time in an axial slice. The 240 (dashed violet) and 6 (dashed crimson) EM43°C contours, as well as the positions of active transducer segments (gray), at the given time are also shown.

In Case 8, to avoid damage to the right S1 nerve, which exits the posterior sacral foramen less than 4 mm from the posterior portion of the 24 mm long tumor, a single 15 mm long transducer with dual 180° sectors was translated and rotated within the tumor. The anterior portion of the tumor was ablated first (9.5 W/cm^2, 190 s), followed by the posterior portion (15.3 W/cm^2, 50 s), with 10 seconds in between during which power and flow were shut off (Figure 5.9C-D). The 30° dead zone between the active sectors was directed towards the nearby sacral canal and foramen to mildly reduce heating of the nerves, with one active sector pointing superior, and the other inferior. Greater temperature increases were calculated in the left posterior portion of the tumor, which was surrounded by bone and adjacent to the spinal nerves, than in the right posterior portion of the tumor, which was adjacent to soft tissue. To ablate the right portion of tumor without damaging the spinal nerves to the left, the applicator was rotated. 17.8 W/cm^2 was applied only to the sector pointing right for 50 s, while the sector pointing left was kept off (Figure 5.9E). These treatment parameters resulted in ablation of nearly the whole volume of the tumor (99.9%), while limiting the thermal dose to the spinal canal and nerves to 3.6 EM43°C.

In Case 9, ablation of a mixed osteolytic and osteoblastic tumor was simulated with 7 MHz and 3 MHz applicators (Figure 5.10), with powers determined by a feedback controller. The 7 MHz applicator, which used lower powers (7.5 W electric, as opposed to 11.8 W electric) to reach the same temperatures, took more than twice as long to ablate the full volume. (Since the high frequency transducer had a lower surface area, although the applied powers (W) were lower than at 3 MHz, the surface intensity (W/cm^2) reported in Table 5.4 was higher.) Thermal dose contours with a slightly wider radial extent were calculated in the 3 MHz case (13.3 mm, 240 EM43°C) than the 7 MHz case (12.4 mm, 240 EM43°C) (Figure 5.10D-E).

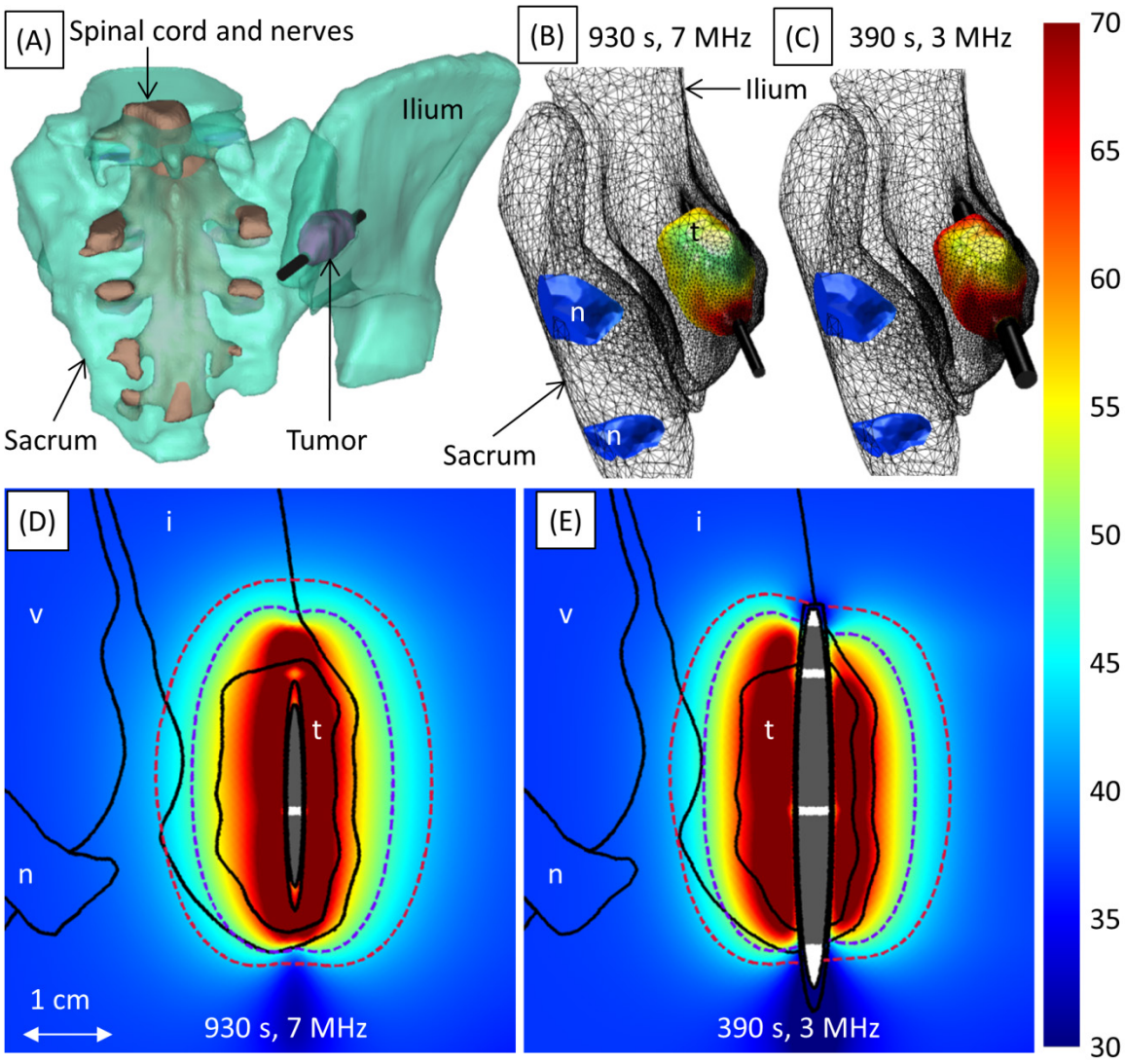

Figure 5.10 Ablation of a mixed osteolytic and osteoblastic tumor in the right iliac bone near the sacral nerves (Case 9). (B) and (D) show ablation with a 7 MHz applicator (Case 9a). (C) and (E) show ablation with a 3 MHz applicator (Case 9b). (A) 3D anatomical surface meshes used to create the finite element mesh. (B-C) The temperature (°C) on the spinal canal and tumor 250 s into the treatment. The applicator (black cylinder) and bone surface (black mesh) are also shown. (D-E) show temperature at the end of treatment in an axial slice. The 240 (dashed violet) and 6 (dashed crimson) EM43°C contours, as well as transducer positions (gray), are also shown.

5.5 Discussion

This simulation study was designed to investigate the feasibility and performance of interstitial ultrasound ablation of tumors in and near the spine. FEM models were utilized in patient-

specific studies to explore treatment delivery strategies and to develop guidelines for ablating tumors of various sizes in the vicinity of the spine. Thermal and acoustic insulation, preferential bone heating, and power control along the length and angle of interstitial ultrasound applicators can be of particular use for ablation in and near the spine, due to the need to protect highly sensitive tissues. The critical anatomy in the vicinity of the spine includes the spinal cord, spinal nerves, aorta, vena cava, esophagus, trachea, and lungs.

Patient-specific models demonstrated the feasibility of interstitial ultrasound ablation of tumors in and near the spine, with complete ablation of 5 tumors at least 4.3 mm from the spinal canal, and ablation of 94.6-100% of the volumes of 4 tumors within 4.5 mm of the spinal canal (Table 5.4). This patient-specific study indicates that tumors at least 5 mm from the sensitive neural elements can be fully treated with interstitial ultrasound ablation without the need for gaseous insulation. However, parametric studies determined that 4 mm of bone surrounding cylindrical tumors is sufficient to insulate nervous structures, with 3 mm of bone sufficient in tumors 16-20 mm in diameter or under 6 mm in diameter (Figure 4.4). Thicker bone insulation was required in some patient-specific models most likely because the tumors were irregularly shaped. When one portion of a tumor is wider than another, such as the tumor 4.5 mm from the spinal canal in Case 3 (Figure 5.4B), the higher powers necessary to ablate the wide portion may overheat parts of the spinal canal near a narrow portion. In such cases, additional nervous protection may be required in order to ablate the full tumor volume.

A variety of techniques were found to protect sensitive anatomy. Less or no power can be delivered to transducer sectors directed toward the spinal cord, nerve roots, or other sensitive tissues, as in Cases 3, 4, 5, and 8 (Figure 5.4 - Figure 5.6, Figure 5.9). The sector angles were selected so that highly heated areas, such as sonicated bone surfaces, were at least 3-4 mm from

tissues to be preserved. The number and lengths of the transducers were selected so that the transducer arrays extended beyond the full length of the tumors, and so that individual transducers sectors were aligned with any volumes to receive less energy (Cases 1-9). The applicator can be placed near critical structures, and all power can be directed away from them, as in Figure 5.4. Alternatively, a transducer can be translated and/or rotated to ablate a target volume while limiting heating of sensitive structures (Figure 5.9). Gaseous dissection can thermally and acoustically insulate vital neurological structures, which is particularly necessary if there is less than 4-5 mm of healthy bone to insulate them (Figure 5.5). MR temperature imaging and/or temperature probes can monitor treatment in real-time and provide feedback to power controllers [113, 218].

The directionality and minimally invasive nature of interstitial ultrasound ablation provides it with some benefits as compared to other ablative modalities. Other ablation modalities used in the spine lack directional control. To protect the spinal cord, they rely solely on cortical bone insulation, the cooling flow of blood and CSF, and/or carbon dioxide dissection [103, 104, 106, 113], which can be applied during interstitial ultrasound ablation. A single interstitial ultrasound applicator with variable power control to four 1 cm long transducers can treat the entire length of a 43 mm long tumor at once (Table 5.4, Figure 5.5). In contrast, RF electrodes with short (1 cm) active tips need to be used in many cases to prevent neurological damage [219]. Unlike HIFU, which requires an acoustic window to a large external transducer, interstitial ultrasound can treat tumors enclosed within bone (Figure 5.5 - Figure 5.10).

Interstitial ultrasound ablation can take advantage of techniques used with other ablation modalities. Applicator placement, cement injection to ensure mechanical stability, and gaseous dissection for neural protection can be performed following methodologies already in place for

RF and laser ablation procedures in the spine [93, 94, 103, 107, 113]. As with other ablative modalities [109, 220], an interstitial ultrasound applicator can be repositioned within the tumor and multiple applicators can be used simultaneously in order to ablate larger volumes.

Long ablation durations over 10 min, as in Case 9a (Figure 5.10D), are necessary for 7 MHz interstitial ultrasound ablation of permeative, mixed, or osteoblastic lesions, which, due to high bone content, are likely to have high ultrasound attenuation coefficients. Alternatively, ablation can be performed at 3 MHz with shorter ablation durations, as in Case 9b, as greater penetration into bone at low frequencies allows for the use of higher powers without the risk of water vaporization in tissue (Figure 5.10E). To accommodate the thicker transducers needed to produce longer wavelengths, 3 MHz applicators have larger diameters than 7 MHz applicators. The diameters of the 3 MHz applicators considered are similar to those used in vertebroplasty, such as the KyphX system which requires a 4.2 mm cannula (Medtronic, Inc., Minneapolis, MN).

5.6 Conclusion

Patient-specific studies have demonstrated the capability of interstitial ultrasound ablation to create thermal lesions conforming to the shapes of tumors in and near the spine while preserving critical anatomical structures nearby. Preferential acoustic absorption at bone surfaces results in additional heating at the boundaries of tumors adjacent to bone, enhancing and accelerating ablation. Sensitive anatomy can be maintained at safe temperatures though the control of power along the length and angle of the applicator, so that little or no energy is directed towards critical structures. Larger 3 MHz transducers may be used to treat tumors with attenuations higher than those of soft tissues. Interstitial ultrasound ablation appears feasible for the ablation of tumors at

least 4-5 mm from critical neural structures. Treatment can be applied using directional applicators and/or in conjunction with gaseous dissection to ablate all or part of the volumes of tumors 0-5 mm from the spinal canal and nerves.

Chapter 6

Conclusions and future work

6.1 Research summary

The goals of this work are to gain a thorough understanding of heat propagation through bone during interstitial ultrasound ablation, to develop and validate numerical models of interstitial ultrasound ablation involving bone, to evaluate the feasibility of interstitial ultrasound ablation of targets in and near the spine, and to determine potential treatment delivery strategies and guidelines for treatment in the vicinity of the spine. Experimental measurements of temperature, lesion sizes, and changes in MR properties during interstitial ultrasound ablation revealed trends in heat deposition in and near bone, such as the capacity of preferential bone heating to produce wider or higher temperature peaks. Numerical biothermal and acoustic models of acoustic bone heating were developed that reflected these trends and were validated experimentally. These models were applied to demonstrate the feasibility of interstitial ultrasound ablation of vertebral and paraspinal tumors and to create guidelines for treatment.

Biothermal and acoustic models of interstitial ultrasound ablation involving bone were developed and evaluated in Chapters 2 and 3, incorporating a series of approximations to estimate heat deposition in bone and soft tissue. Acoustic propagation and absorption in bone are more complicated than in homogenous soft tissues, because reflection, partial transmission, refraction, and shear mode conversion play more significant roles. The necessity of modeling these phenomena was evaluated, and approximations of heat deposition in bone were developed to simplify the models and reduce computation times. Acoustic energy transmitted into bone could be assumed to be absorbed directly on the bone surface without introducing any significant errors in temperature distributions, in cases when the bone is at least ~3 mm thick. Approximations that applied constant transmission coefficients and that did not consider reflection, refraction, or shear mode conversion produced temperature distributions that closely matched both more comprehensive models and experimental measurements.

In Chapter 3, experimental studies of interstitial ultrasound ablation involving bone demonstrated trends in temperature distributions during involving bone. The temperature in bone decreased rapidly behind the bone surface, regardless of whether the applicator was placed in soft tissue or bone. When the applicator was placed in soft tissue and directed towards bone, two temperature peaks or inflections were observed: one near the applicator, and a secondary peak at the bone surface. The height of the peak at the bone surface varied roughly linearly with distance from the bone surface. These peaks were about the same height when the applicator was within ~15-16 mm of the bone surface, and they overlapped to form a single higher or wider peak when the applicator was within ~20 mm of the bone surface. The presence of bone can serve to increase the volumes that can be treated with interstitial ultrasound and/or to reduce the necessary treatment times.

The appropriate treatment parameters for ablation of osteolytic tumors were directly related to the relative heights of the two temperature peaks located adjacent to the applicator and at bone surfaces, as shown in Chapter 4. The powers necessary to ablate small osteolytic tumors (≤16 mm D) scaled linearly with the distance between the applicator and the bone, and the required treatment times were relatively short, because temperatures peaked at the bone/tumor boundaries, which heated quickly. In larger tumors, temperatures peaked near the applicator, and constant powers as a function of tumor diameter were necessary to control the peak temperature to a fixed level. Consequently, much longer treatment times were necessary to treat larger tumors.

7 MHz interstitial ultrasound ablation is best suited for ablation of highly osteolytic bone tumors and soft tissue tumors. In tumors with significant bone content and high attenuations, temperatures peak near the applicator, and the rest of the volume is heated by conduction, limiting the volumes that can be treated in a given time frame without vaporization of water. Low frequency (~3 MHz) applicators can potentially provide better penetration into osteoblastic or mixed tumors.

The feasibility of interstitial ultrasound ablation in targets in and near the spine was demonstrated in the 3D patient-specific models presented in Chapter 5. Preferential bone heating combined with directional heat deposition patterns resulted in shorter treatment times and larger treatment volumes better localized to the tumor volume than could be attained in soft tissue alone. Simulations showed that targets insulated from the spinal canal by 4-5 mm of normal bone could be fully ablated without causing neurological damage. The majority of the volumes of tumors within 4-5 mm of the spinal canal could be ablated without nervous damage when the acoustic energy was directed away from the spinal canal and when gaseous dissection was

applied. To prevent damage to nearby sensitive structures, osteolytic tumors with diameters of 16 mm or less were best ablated quickly with high powers, rather than relatively slowly with low powers. In larger tumors, the balance of power and time had few significant effects on the nearby sensitive anatomy.

Interstitial ultrasound ablation in the setting of the spine has several advantages over other ablative modalities. Unlike with HIFU, an acoustic window to an external transducer is not necessary, allowing for access to highly osteolytic lesions encapsulated by bone and to targets shadowed by the irregularly shaped vertebrae. Interstitial ultrasound has directional control not attainable with electromagnetic ablative modalities, both along the length and circumference of the applicator. Furthermore, directional power control combined with preferential acoustic absorption of bone and with the thermally and acoustically insulative properties of bone results in thermal lesions conforming closely to the shapes of osteolytic targets (Figure 5.3 - Figure 5.9). Such precision is a particular necessity in and near the spine, where several highly sensitive anatomical structures are located.

A variety of needle-, MR-, and ultrasound-based techniques were applied in this study to monitor ultrasound ablation involving bone, both to evaluate the heating distributions produced by devices and to provide comparisons to theoretical calculations. In experiments, invasive temperature measurements required holes to be drilled in the precise location where temperature was to be measured, and temperature could only be measured at a few discrete points. In practice, discrete needle based sensors could be placed using suitable bone needles. Because temperatures drop very rapidly behind bone surfaces, misalignment of invasive temperature probe could result in significant errors in the recorded temperatures.

Ultrasound-based and PRF-based techniques for monitoring temperature generally provide little to no information inside bone. However, these methods could be used to monitor temperature in soft tissues heated either directly by incident ultrasound waves or heated through conduction from bones, as shown in Sections 3.4.3-3.4.4. Temperatures on adjacent bone surfaces can be inferred from soft tissue temperatures. Numerical models could potentially be applied to estimate temperatures throughout bone volumes based on temperatures measured in the adjacent soft tissues.

We have explored other MR-based methods which have shown potential for qualitatively monitoring temperature in cortical and/or cancellous bone, particularly the mapping of changes in T1. T1- and PRF-based methods could potentially be applied in conjunction to provide temperature information in both bone and soft tissue. In cases where precise measurements throughout a volume are not necessary, invasive temperature measurements can be employed as a less expensive, real-time alternative.

In Appendix B, temperature-dependent ultrasound contrast agents that underwent a phase shift upon heating were produced and studied. They contained perfluorocarbons with boiling points of 45 or 54°C and a stabilizing polymer shell. When heated rapidly to 44°C or higher, the microcapsules vaporized and increased in echogenicity. The echogenicity was low below 44°C, was linear with temperature from 44 to 55°C, and plateaued above 55°C. However, the microcapsules were not stable over time at room or physiological temperatures. If reformulated for greater stability over time, these contrast agents may have applications in monitoring hyperthermia, which is applied at lower temperatures (40-45°C).

6.2 Future directions

6.2.1 Experimental studies

Patient-specific numerical models have indicated that interstitial ultrasound ablation is feasible for treatment of vertebral and paraspinal tumors. Experimental studies in human cadaver spines should be performed to further evaluate the capabilities of interstitial ultrasound ablation in paraspinal and vertebral tumors, with temperature monitored using MRTI or with carefully placed invasive temperature sensors. If possible, vertebrae containing osteolytic tumors and vertebrae adjacent to paraspinal tumors should be obtained. In the case that osteolytic vertebral tumors are not available in sufficient quantities or at all, a bone tumor phantom should be designed and inserted into a cavity made in the vertebrae. To ensure that the phantom correctly reflects the acoustic and thermal properties of bone tumors, several samples of osteolytic tumors from the bones of large mammals (> ~10 kg) should be obtained if possible, and the material properties of these samples should be measured.

The flow of blood and cerebrospinal fluid is known to have a cooling effect during thermal ablation that can serve to protect the spinal canal and/or cause insufficient treatment of the target tissue. *In vivo* studies in a large animal model should be performed before the commencement of clinical trials.

The design of interstitial ultrasound applicators could be further optimized for treatment of lesions with high bone content and high acoustic absorption coefficients. Additional studies with otherwise identical planar applicators operating at a variety of frequencies (3, 5, and 7 MHz) should be performed with invasive temperature measurements and T1 mapping to further investigate the penetration of low frequency applicators into both cancellous and cortical bone. Acoustic beam plots and efficiency measurements should be performed on these applicators to

ensure that any differences between the devices in efficiency and beam shape are accounted for. If penetration is shown to be greater at lower frequencies, directional low-frequency applicators with sectored tubular transducers should be evaluated in *in vivo* or *ex vivo* bone tumor models.

6.2.2 Treatment planning

The numerical models developed in this study could potentially be developed into a fast treatment planning platform, though significant modifications would be required. One of the primary obstacles is that the models used in the feasibility studies in this work are slow to generate and to compute, on the order of a few days. Although time-intensive modeling can be useful for treatment planning, a faster process would be preferable. The models could easily be used to define applicator positions and insertion trajectories, as 3D anatomical visualization and applicator placement are early steps in the process and are not time-consuming. The finite element meshes could be generated significantly faster if only two sets of material properties were considered, one for bone and one for soft tissue, because it takes a substantial amount of time to segment the various organs and to merge them into one finite element mesh. A simulation study should be performed to determine whether this would introduce unacceptable inaccuracies in the resulting temperature distributions. Another technique to compensate for the slow modeling process would be to begin modeling far in advance of treatment. As opposed to generating treatment plans based on MR or CT scans taken the day of the treatment, it may be possible to generate models based on prior image sets, because the spine deforms less than soft tissues, and the surrounding anatomy is less likely to change from day to day. A system for registering the images on which the treatment plan is based to an image set taken immediately prior to the treatment, and for adjusting the treatment parameters as necessary, may be necessary.

An inverse treatment planning algorithm for determining the optimal number of transducers, transducer sector sizes, powers, and treatment durations for each patient case could be highly useful. The treatment parameters applied in the patient-specific models in this work were determined iteratively, with the initial parameters based on the tumor size, the distance from the tumor to the spinal canal, and the distance from the applicator to bone surfaces. As this process is likely to be too time intensive for treatment planning, an inverse planning algorithm could be more time efficient.

Treatment planning systems may determine the parameters necessary to raise the minimum temperature of a tumor to a target temperature while keeping the maximum temperature below the boiling point of water. In the spine, such a system would have the additional constraint of maintaining nearby sensitive anatomy below a temperature threshold. The presence of irregular bone surfaces significantly complicates matters, making it significantly less straightforward than in purely soft tissue to predict the location of the maximum temperature peaks or the shapes of the temperature contours. A treatment planning system applied in and near the vertebrae would have to take this into account.

Bibliography

[1] Wust P, Hildebrandt B, Sreenivasa G, Rau B, Gellermann J, Riess H et al. Hyperthermia in combined treatment of cancer. *The lancet oncology* 2002;3:487-97.

[2] Hildebrandt B, Wust P. The biologic rationale of hyperthermia. *Peritoneal Carcinomatosis: A multidisciplinary approach*. New York: Springer US; 2007. p. 171-84.

[3] Mala T. Cryoablation of liver tumours-a review of mechanisms, techniques and clinical outcome. *Minim Invasive Ther Allied Technol* 2006;15:9-17.

[4] Theodorescu D. Cancer cryotherapy: Evolution and biology. *Reviews in urology* 2004;6:S9.

[5] Roti Roti JL. Cellular responses to hyperthermia (40-46 C): Cell killing and molecular events. *Int J Hyperthermia* 2008;24:3-15.

[6] Habash RW, Bansal R, Krewski D, Alhafid HT. Thermal therapy, Part III: Ablation techniques. *Crit Rev Biomed Eng* 2007;35.

[7] Martel J, Bueno Á, Nieto-Morales ML, Ortiz EJ. Osteoid osteoma of the spine: CT-guided monopolar radiofrequency ablation. *Eur J Radiol* 2009;71:564-69.

[8] Kurup AN, Callstrom MR. Ablation of skeletal metastases: Current status. *J Vasc Interv Radiol* 2010;21:S242-S50.

[9] Hynynen K. MRIgHIFU: A tool for image-guided therapeutics. *J Magn Reson Imaging* 2011;34:482-93.

[10] Herman A, Avivi E, Brosh T, Schwartz I, Liberman B. Biomechanical properties of bone treated by magnetic resonance-guided focused ultrasound—An in vivo porcine model study. *Bone* 2013;57:92-97.

[11] Catane R, Beck A, Inbar Y, Rabin R, Shabshin N, Hengst S et al. MR-guided focused ultrasound surgery (MRgFUS) for the palliation of pain in patients with bone metastases—preliminary clinical experience. *Ann Oncol* 2007;18:163-67.

[12] Liberman B, Gianfelice D, Inbar Y, Beck A, Rabin T, Shabshin N et al. Pain palliation in patients with bone metastases using MR-guided focused ultrasound surgery: A multicenter study. *Ann Surg Oncol* 2009;16:140-46.

[13] Monteith S, Sheehan J, Medel R, Wintermark M, Eames M, Snell J et al. Potential intracranial applications of magnetic resonance–guided focused ultrasound surgery: A review. *J Neurosurg* 2013;118:215-21.

[14] Diederich CJ. Thermal ablation and high-temperature thermal therapy: Overview of technology and clinical implementation. *Int J Hyperthermia* 2005;21:745-53.

[15] van Rhoon GC. External electromagnetic methods and devices. In: Moros E, editor. *Physics of Thermal Therapy: Fundamentals and Clinical Applications*. New York, New York: CRC Press; 2012. p. 139-58.

[16] Chen L, Li F, Wu F, Moros EG. Clinical external ultrasonic treatment devices. In: Moros E, editor. *Physics of Thermal Therapy: Fundamentals and Clinical Applications*. New York, New York: CRC Press; 2012. p. 177-88.

[17] Diederich CJ. Endocavity and catheter-based ultrasound devices. In: Moros E, editor. *Physics of Thermal Therapy: Fundamentals and Clinical Applications*. New York, New York: CRC Press; 2012. p. 189-200.

[18] Sotsky TK, Ravikumar TS, editors. Cryotherapy in the treatment of liver metastases from colorectal cancer. Semin Oncol; 2002: 183-91: Elsevier.

[19] Simon CJ, Dupuy DE, Mayo-Smith WW. Microwave ablation: Principles and applications. *Radiographics* 2005;25:S69-S83.

[20] Ni Y, Mulier S, Miao Y, Michel L, Marchal G. A review of the general aspects of radiofrequency ablation. *Abdom Imaging* 2005;30:381-400.

[21] Padma S, Martinie JB, Iannitti DA. Liver tumor ablation: percutaneous and open approaches. *J Surg Oncol* 2009;100:619-34.

[22] Brace CL. Microwave ablation technology: What every user should know. *Curr Probl Diagn Radiol* 2009;38:61-67.

[23] Ahmed M, Brace CL, Lee FT, Goldberg SN. Principles of and advances in percutaneous ablation. *Radiology* 2011;258:351-69.

[24] Pearce JA. Thermal dose models: Irreversible alterations in tissues. In: Moros E, editor. *Physics of Thermal Therapy: Fundamentals and Clinical Applications*. New York, New York: CRC Press; 2012. p. 23-40.

[25] Thomsen S, Pearce JA. Thermal damage and rate processes in biologic tissues. *Optical-Thermal Response of Laser-Irradiated Tissue*. New York: Springer; 2011. p. 487-549.

[26] Goldberg SN, Kruskal JB, Gazelle GS, editors. Thermal ablation therapy for focal malignancy: A unified approach to underlying principles, techniques, and diagnostic imaging guidance. BiOS'99 International Biomedical Optics Symposium; 1999: 2-13: International Society for Optics and Photonics.

[27] Goldberg SN, Gazelle GS, Halpern EF, Rittman WJ, Mueller PR, Rosenthal DI. Radiofrequency tissue ablation: Importance of local temperature along the electrode tip exposure in determining lesion shape and size. *Acad Radiol* 1996;3:212-18.

[28] Nikfarjam M, Muralidharan V, Christophi C. Mechanisms of focal heat destruction of liver tumors. *J Surg Res* 2005;127:208-23.

[29] Habash RW, Bansal R, Krewski D, Alhafid HT. Thermal therapy, part 1: An introduction to thermal therapy. *Crit Rev Biomed Eng* 2006;34.

[30] Thanos L, Mylona S, Pomoni M, Kalioras V, Zoganas L, Batakis N. Primary lung cancer: Treatment with radio-frequency thermal ablation. *Eur Radiol* 2004;14:897-901.

[31] Rhim H, Dodd GD. Radiofrequency thermal ablation of liver tumors. *J Clin Ultrasound* 1999;27:221-29.

[32] Dewhirst MW, Viglianti BL, Lora-Michiels M, Hanson M, Hoopes PJ. Basic principles of thermal dosimetry and thermal thresholds for tissue damage from hyperthermia. *Int J Hyperthermia* 2003;19:267-94.

[33] Dewey WC. Arrhenius relationships from the molecule and cell to the clinic. *Int J Hyperthermia* 1994;10:457-83.

[34] Sapareto SA, Dewey WC. Thermal dose determination in cancer therapy. *Int J Radiat Oncol Biol Phys* 1984;10:787-800.

[35] Diederich CJ, Hynynen K. Ultrasound technology for hyperthermia. *Ultrasound Med Biol* 1999;25:871-87.

[36] Issels RD. Hyperthermia adds to chemotherapy. *Eur J Cancer* 2008;44:2546-54.

[37] Horsman MR, Overgaard J. Hyperthermia: A potent enhancer of radiotherapy. *Clin Oncol* 2007;19:418-26.

[38] Kampinga HH, Dikomey E. Hyperthermic radiosensitization: Mode of action and clinical relevance. *Int J Radiat Biol* 2001;77:399-408.

[39] Ganta S, Devalapally H, Shahiwala A, Amiji M. A review of stimuli-responsive nanocarriers for drug and gene delivery. *J Control Release* 2008;126:187-204.

[40] Ponce AM, Vujaskovic Z, Yuan F, Needham D, Dewhirst MW. Hyperthermia mediated liposomal drug delivery. *Int J Hyperthermia* 2006;22:205-13.

[41] Stein RJ, Kaouk JH. Renal cryotherapy: A detailed review including a 5-year follow-up. *BJU Int* 2007;99:1265-70.

[42] Hand JW. Physics of electromagnetic energy sources. In: Moros E, editor. *Physics of Thermal Therapy: Fundamentals and Clinical Applications*. New York, New York: CRC Press; 2012. p. 57-74.

[43] Decadt B, Siriwardena AK. Radiofrequency ablation of liver tumours: Systematic review. *The lancet oncology* 2004;5:550-60.

[44] Brace CL. Radiofrequency and microwave ablation of the liver, lung, kidney, and bone: What are the differences? *Curr Probl Diagn Radiol* 2009;38:135-43.

[45] Lubner MG, Brace CL, Hinshaw JL, Lee FT. Microwave tumor ablation: Mechanism of action, clinical results, and devices. *J Vasc Interv Radiol* 2010;21:S192-S203.

[46] Izzo F. Other thermal ablation techniques: Microwave and interstitial laser ablation of liver tumors. *Ann Surg Oncol* 2003;10:491-97.

[47] Vogl TJ, Naguib NN, Lehnert T, Nour-Eldin N-EA. Radiofrequency, microwave and laser ablation of pulmonary neoplasms: Clinical studies and technical considerations—review article. *Eur J Radiol* 2011;77:346-57.

[48] Beccaria K, Canney MS, Carpentier AC. Magnetic resonance-guided laser interstitial thermal therapy for brain tumors. *Tumors of the Central Nervous System, Volume 5*. New York: Springer; 2012. p. 173-85.

[49] Wu F. High intensity focused ultrasound (HIFU) ablation. *Tumor Ablation: Effects on Systemic and Local Anti-Tumor Immunity and on Other Tumor-Microenvironment Interactions*. 5. New York: Springer; 2013. p. 61-75.

[50] Pfeffer MR, Rabin T, Inbar Y, Hananel A, Catane R. Image-guided high-intensity focused ultrasound in the treatment of cancer. In: Dupuy D, Fong Y, McMullen W, editors. *Image-Guided Cancer Therapy – A Multidisciplinary Approach*. Berlin: Springer; 2013.

[51] Coussios C, Farny C, Ter Haar G, Roy R. Role of acoustic cavitation in the delivery and monitoring of cancer treatment by high-intensity focused ultrasound (HIFU). *Int J Hyperthermia* 2007;23:105-20.

[52] Ellis S, Rieke V, Kohi M, Westphalen AC. Clinical applications for magnetic resonance guided high intensity focused ultrasound (MRgHIFU): Present and future. *J Med Imaging Radiat Oncol* 2013;57:391-99.

[53] Wells P. Absorption and dispersion of ultrasound in biological tissue. *Ultrasound Med Biol* 1975;1:369-76.

[54] Hynynen K. Biophysics and technology of ultrasound hyperthermia. *Methods of external hyperthermic heating*. New York: Springer; 1990. p. 61-115.

[55] Bull V, ter Haar GR. The physics of ultrasound energy sources. In: Moros E, editor. *Physics of Thermal Therapy: Fundamentals and Clinical Applications*. New York, New York: CRC Press; 2012. p. 75-93.

[56] ter Haar G. Principles of high-intensity focused ultrasound. *Interventional Oncology*. New York: Springer; 2012. p. 51-63.

[57] Apfel RE, Holland CK. Gauging the likelihood of cavitation from short-pulse, low-duty cycle diagnostic ultrasound. *Ultrasound Med Biol* 1991;17:179-85.

[58] Hynynen K. The threshold for thermally significant cavitation in dog's thigh muscle *in vivo*. *Ultrasound Med Biol* 1991;17:157-69.

[59] Duck F. *Physical Properties of Tissue: A Comprehensive Reference Book.* London: Academic Press Limited, 1990.

[60] Fennessy FM, Tempany CM. An update on magnetic resonance guided focused ultrasound surgery (MRgFUS) of uterine fibroids. *Current Radiology Reports* 2013:1-11.

[61] Zhang L, Wang Z-B. High-intensity focused ultrasound tumor ablation: Review of ten years of clinical experience. *Front Med China* 2010;4:294-302.

[62] Choi J, Raghavan M. Diagnostic imaging and image-guided therapy of skeletal metastases. *Cancer Control* 2012;19:102-12.

[63] Vaezy S, Andrew M, Kaczkowski P, Crum L. Image-guided acoustic therapy. *Annu Rev Biomed Eng* 2001;3:375-90.

[64] Ross AB, Diederich CJ, Nau WH, Rieke V, Butts RK, Sommer G et al. Curvilinear transurethral ultrasound applicator for selective prostate thermal therapy. *Med Phys* 2005;32:1555.

[65] Diederich CJ, Hynynen K. Induction of hyperthermia using an intracavitary multielement ultrasonic applicator. *IEEE Trans Biomed Eng* 1989;36:432-38.

[66] Lafon C, Prat F, Chapelon J, Gorry F, Margonari J, Theillere Y et al. Cylindrical thermal coagulation necrosis using an interstitial applicator with a plane ultrasonic transducer: in vitro and in vivo experiments versus computer simulations. *Int J Hyperthermia* 2000;16:508-22.

[67] Diederich CJ. Ultrasound applicators with integrated catheter-cooling for interstitial hyperthermia: Theory and preliminary experiments. *Int J Hyperthermia* 1996;12:279-97.

[68] Nau WH, Diederich CJ, Burdette EC. Evaluation of multielement catheter-cooled interstitial ultrasound applicators for high-temperature thermal therapy. *Med Phys* 2001;28:1525-34.

[69] Chopra R, Luginbuhl C, Weymouth AJ, Foster FS, Bronskill MJ. Interstitial ultrasound heating applicator for MR-guided thermal therapy. *Phys Med Biol* 2001;46:3133.

[70] Nau WH, Diederich CJ, Stauffer PR. Directional power deposition from direct-coupled and catheter-cooled interstitial ultrasound applicators. *Int J Hyperthermia* 2000;16:129-44.

[71] Deardorff DL, Diederich CJ. Axial control of thermal coagulation using a multi-element interstitial ultrasound applicator with internal cooling. *IEEE Trans Ultrason, Ferroelectr, Freq Control* 2000;47:170-78.

[72] Deardorff DL, Diederich CJ, Nau WH. Control of interstitial thermal coagulation: Comparative evaluation of microwave and ultrasound applicators. *Med Phys* 2000;28:104-17.

[73] Kangasniemi M, Diederich CJ, Price RE, Stafford RJ, Schomer DF, Olsson LE et al. Multiplanar MR temperature-sensitive imaging of cerebral thermal treatment using interstitial ultrasound applicators in a canine model. *J Magn Reson Imaging* 2002;16:522-31.

[74] Nau WH, Diederich CJ, Ross AB, Butts K, Rieke V, Bouley DM et al. MRI-guided interstitial ultrasound thermal therapy of the prostate: A feasibility study in the canine model. *Med Phys* 2005;32:733-43.

[75] Lafon C, Melodelima D, Salomir R, Chapelon JY. Interstitial devices for minimally invasive thermal ablation by high-intensity ultrasound. *Int J Hyperthermia* 2007;23:153-63.

[76] Coleman R. Metastatic bone disease: Clinical features, pathophysiology and treatment strategies. *Cancer Treat Rev* 2001;27:165-76.

[77] Mundy GR. Metastasis to bone: Causes, consequences and therapeutic opportunities. *Nat Rev Cancer* 2002;2:584-93.

[78] SEER Cancer Statistics Review, 1975-2009 (Vintage 2009 populations). In: Howlander N, Noone AM, Krapcho M, Neyman N, Aminou R, Altekruse SF, et al., editors. Bethesda, MD: National Cancer Institute; 2012.

[79] Park KY, Shin DA, Shin HC, Yoon DH, Kim KN. Surgical management of paraspinal tumors. *Kor J Spine* 2007;4:134-39.

[80] Palussière J, Dousset V. Imaging of vertebral metastases. *Vertebral metastases*. France: Springer; 2002. p. 60-84.

[81] Longhi A, Erranib C, Paolisb MD, Mercurib M, Baccia G. Primary bone osteosarcoma in the pediatric age: State of the art. *Cancer Treat Rev* 2006;32:423–36.

[82] Nagarajan R, Neglia JP, Clohisy DR, Robison LL. Limb salvage and amputation in survivors of pediatric lower-extremity bone tumors: What are the long-term implications? *J Clin Oncol* 2002;20:4493-501.

[83] Sciubba DM, Petteys RJ, Dekutoski MB, Fisher CG, Fehlings MG, Ondra SL et al. Diagnosis and management of metastatic spine disease: A review. *J Neurosurg Spine* 2010;13:94-108.

[84] Rosenthal D, Callstrom MR. Critical review and state of the art in interventional oncology: Benign and metastatic disease involving bone. *Radiology* 2012;262:765-80.

[85] Klimo Jr. P, Schmidt MH. Surgical management of spinal metastases. *The Oncologist* 2004;9:188-96.

[86] Callstrom MR, Charboneau JW, Goetz MP, Rubin J, Atwell TD, Farrell MA et al. Image-guided ablation of painful metastatic bone tumors: A new and effective approach to a difficult problem. *Skeletal Radiol* 2006;35:1-15.

[87] Georgy BA. Metastatic spinal lesions: State-of-the-art treatment options and future trends. *Am J Neuroradiol* 2008;29:1605-11.

[88] Healey JH, Brown HK. Complications of bone metastases. *Cancer* 2000;88:2940-51.

[89] Cantwell CP, Obyrne J, Eustace S. Current trends in treatment of osteoid osteoma with an emphasis on radiofrequency ablation. *Eur Radiol* 2004;14:607-17.

[90] Schwab JH, Springfield DS, Raskin KA, Mankin HJ, Hornicek FJ. What's new in primary bone tumors. *J Bone Joint Surg Am* 2012;94:1913-19.

[91] Terezakis SA, Lovelock DM, Bilsky MH, Hunt MA, Zatcky J, Yamada Y. Image-guided intensity-modulated photon radiotherapy using multifractionated regimen to paraspinal chordomas and rare sarcomas. *International Journal of Radiation Oncology*Biology*Physics* 2007 12/1/;69:1502-08.

[92] Weber DC, Trofimov AV, Delaney TF, Bortfeld T. A treatment planning comparison of intensity modulated photon and proton therapy for paraspinal sarcomas. *Int J Radiat Oncol Biol Phys* 2004 4/1/;58:1596-606.

[93] van der Linden E, Kroft LJ, Dijkstra P. Treatment of vertebral tumor with posterior wall defect using image-guided radiofrequency ablation combined with vertebroplasty: Preliminary results in 12 patients. *J Vasc Interv Radiol* 2007;18:741-47.

[94] Katonis P, Pasku D, Alpantaki K, Bano A, Tzanakakis G, Karantanas A. Treatment of pathologic spinal fractures with combined radiofrequency ablation and balloon kyphoplasty. *World J Surg Oncol* 2009;7:90.

[95] Pinto CH, Taminiau AHM, Vanderschueren1 GM, Hogendoorn PCW, Bloem JL, Obermann WR. Technical considerations in CT-guided radiofrequency thermal ablation of osteoid osteoma: Tricks of the trade. *Am J Roentgenol* 2002;179:1633-42.

[96] Tins B, Cassar-Pullicino V, McCall I, Cool P, Williams D, Mangham D. Radiofrequency ablation of chondroblastoma using a multi-tined expandable electrode system: Initial results. *Eur Radiol* 2006;16:804-10.

[97] Schaefer O, Lohrmann C, Markmiller M, Uhrmeister P, Langer M. Combined treatment of a spinal metastasis with radiofrequency heat ablation and vertebroplasty. *Am J Roentgenol* 2003;180:1075-77.

[98] Nakatsuka A, Yamakado K, Maeda M, Yasuda M, Akeboshi M, Takaki H et al. Radiofrequency ablation combined with bone cement injection for the treatment of bone malignancies. *J Vasc Interv Radiol* 2004;15:707-12.

[99] Gianfelice D, Gupta C, Kucharczyk W, Bret P, Havill D, Clemons M. Palliative treatment of painful bone metastases with MR imaging–guided focused ultrasound. *Radiology* 2008;249:355-63.

[100] Gangi A, Dietemann J, Gasser B, Mortazavi R, Brunner P, Mourou M et al. Interstitial laser photocoagulation of osteoid osteomas with use of CT guidance. *Radiology* 1997;203:843-48.

[101] Callstrom MR, Atwell TD, Charboneau JW, Farrell MA, Goetz MP, Rubin J et al. Painful metastases involving bone: Percutaneous image-guided cryoablation—Prospective trial interim analysis. *Radiology* 2006;241:572-80.

[102] Anis N, Chawki N, Antoine K. Use of radio-frequency ablation for the palliative treatment of sacral chordoma. *Am J Neuroradiol* 2004;25:1589-91.

[103] Rybak LD, Gangi A, Buy X, Vieira RLR, Wittig J. Thermal ablation of spinal osteoid osteomas close to neural elements: Technical considerations. *Am J Roentgenol* 2010;195:W293-W98.

[104] Dupuy DE, Hong R, Oliver B, Goldberg SN. Radiofrequency ablation of spinal tumors: Temperature distribution in the spinal canal. *Am J Roentgenol* 2000;175:1263-66.

[105] Gangi A, Basile A, Buy X, Alizadeh H, Sauer B, Bierry G, editors. Radiofrequency and laser ablation of spinal lesions. Seminars in Ultrasound, CT, and MRI; 2005: 89-97: Elsevier.

[106] Vanderschueren GM, Obermann WR, Dijkstra SP, Taminiau AH, Bloem JL, van Erkel AR. Radiofrequency ablation of spinal osteoid osteoma: Clinical outcome. *Spine* 2009;34:901-03.

[107] Georgy B. Bone cement deposition patterns with plasma-mediated radio-frequency ablation and cement augmentation for advanced metastatic spine lesions. *Am J Neuroradiol* 2009;30:1197-202.

[108] Carrafiello G, Laganà D, Pellegrino C, Fontana F, Mangini M, Nicotera P et al. Percutaneous imaging-guided ablation therapies in the treatment of symptomatic bone metastases: Preliminary experience. *Radiol Med* 2009;114:608-25.

[109] Pusceddu C, Sotgia B, Fele RM, Melis L. Treatment of bone metastases with microwave thermal ablation. *J Vasc Interv Radiol* 2012;24:229–33.

[110] Tsoumakidou G, Garnon J, Ramamurthy N, Buy X, Gangi A. Interest of electrostimulation of peripheral motor nerves during percutaneous thermal ablation. *Cardiovasc Intervent Radiol* 2013:1-5.

[111] Wong DA, Fornasier VL, MacNab I. Spinal metastases: The obvious, the occult, and the impostors. *Spine* 1990;15:1-4.

[112] Haveman J, Sminia P, Wondergem J, Van Der Zee J, Hulshof M. Effects of hyperthermia on the central nervous system: What was learnt from animal studies? *Int J Hyperthermia* 2005;21:473-87.

[113] Buy X, Tok C-H, Szwarc D, Bierry G, Gangi A. Thermal protection during percutaneous thermal ablation procedures: Interest of carbon dioxide dissection and temperature monitoring. *Cardiovasc Intervent Radiol* 2009;32:529-34.

[114] Chan AK, Sigelmann RA, Guy AW. Calculations of therapeutic heat generated by ultrasound in fat-muscle-bone layers. *IEEE Trans Biomed Eng* 1974;BME-21:280-84.

[115] Hynynen K, DeYoung D. Temperature elevation at muscle-bone interface during scanned, focused ultrasound hyperthermia. *Int J Hyperthermia* 1988;4:267-79.

[116] Jolesz FA. MRI-guided focused ultrasound surgery. *Annu Rev Med* 2009;60:417-30.

[117] Bruners P, Pandeya GD, Levit E, Roesch E, Penzkofer T, Isfort P et al. CT-based temperature monitoring during hepatic RF ablation: Feasibility in an animal model. *Int J Hyperthermia* 2012;28:55-61.

[118] Saccomandi P, Schena E, Silvestri S. Techniques for temperature monitoring during laser-induced thermotherapy: An overview. *Int J Hyperthermia* 2013;29:609-19.

[119] Arthur RM. Temperature imaging using ultrasound. In: Moros E, editor. *Physics of Thermal Therapy: Fundamentals and Clinical Applications*. New York, New York: CRC Press; 2012. p. 219-39.

[120] Stafford RJ, Taylor BA. Practical clinical thermometry. In: Moros E, editor. *Physics of Thermal Therapy: Fundamentals and Clinical Applications*. New York, New York: CRC Press; 2012. p. 41-55.

[121] Dickinson RJ. Thermal conduction errors of manganin-constantan thermocouple arrays. *Phys Med Biol* 1985;30:445.

[122] Hynynen K, Martin C, Watmough D, Mallard J. Errors in temperature measurement by thermocouple probes during ultrasound induced hyperthermia. *Br J Radiol* 1983;56:969-70.

[123] Rieke V, Butts Pauly K. MR thermometry. *J Magn Reson Imaging* 2008;27:376-90.

[124] Robson MD, Gatehouse PD, Bydder M, Bydder GM. Magnetic resonance: An introduction to ultrashort TE (UTE) imaging. *J Comput Assist Tomogr* 2003;27:825-46.

[125] Vogler III J, Murphy W. Bone marrow imaging. *Radiology* 1988;168:679-93.

[126] Rieke V, Butts Pauly K. Echo combination to reduce proton resonance frequency (PRF) thermometry errors from fat. *J Magn Reson Imaging* 2008;27:673-77.

[127] Miller W, editor Toward T1-based thermometry in cortical bone using ultrashort echo-time MRI. 3rd International Symposium on Focused Ultrasound; 2012: 65-BN; Washington DC.

[128] Waspe AC, Looi T, Mougenot C, Amaral J, Temple M, Sivaloganathan S et al. Dynamic T2-mapping during magnetic resonance guided high intensity focused ultrasound ablation of bone marrow. *AIP Conference Proceedings* 2012;1503:222-26.

[129] Bruners P, Levit E, Penzkofer T, Isfort P, Ocklenburg C, Schmidt B et al. Multi-slice computed tomography: A tool for non-invasive temperature measurement? *Int J Hyperthermia* 2010;26:359-65.

[130] Damianou C, Sanghvi N, Fry F. Dependence of ultrasonic attenuation and absorption in dog soft tissues on temperature and thermal dose. *J Acoust Soc Am* 1997;102:628-34.

[131] Arthur R, Straube W, Trobaugh J, Moros E. Non-invasive estimation of hyperthermia temperatures with ultrasound. *Int J Hyperthermia* 2005;21:589-600.

[132] Rivens I, Shaw A, Civale J, Morris H. Treatment monitoring and thermometry for therapeutic focused ultrasound. *Int J Hyperthermia* 2007;23:121-39.

[133] Wells PN, Liang H-D. Medical ultrasound: Imaging of soft tissue strain and elasticity. *Journal of The Royal Society Interface* 2011;8:1521-49.

[134] Fahey BJ, Nelson RC, Hsu SJ, Bradway DP, Dumont DM, Trahey GE. In vivo guidance and assessment of liver radio-frequency ablation with acoustic radiation force elastography. *Ultrasound Med Biol* 2008;34:1590-603.

[135] Sridhar-Keralapura M, Chubb N, Scott S, Phipps N, Burdette C, Diederich C, editors. Ultrasound strain imaging towards verification and guidance of prostate thermal therapy with catheter-based ultrasound applicators. AIP Conference Proceedings; 2010: 337.

[136] Wu T, Felmlee JP, Greenleaf JF, Riederer SJ, Ehman RL. Assessment of thermal tissue ablation with MR elastography. *Magn Reson Med* 2001;45:80-87.

[137] Le Y, Glaser K, Rouviere O, Ehman R, Felmlee JP. Feasibility of simultaneous temperature and tissue stiffness detection by MRE. *Magn Reson Med* 2006;55:700-05.

[138] Li BN, Shen ZH, Chui CK, Numano T, Washio T, Kobayashi E, editors. Evaluation of radiofrequency ablation using magnetic resonance elastography. World Congress on Medical Physics and Biomedical Engineering May 26-31, 2012, Beijing, China; 2013: 2134-37: Springer.

[139] Liu J-B, Merton DA, Wansaicheong G, Forsberg F, Edmonds PR, Deng X-D et al. Contrast enhanced ultrasound for radio frequency ablation of canine prostates: Initial results. *The Journal of urology* 2006;176:1654-60.

[140] Kagadis GC, Katsanos K, Karnabatidis D, Loudos G, Nikiforidis GC, Hendee WR. Emerging technologies for image guidance and device navigation in interventional radiology. *Med Phys* 2012;39:5768.

[141] Prakash P. Theoretical modeling for hepatic microwave ablation. *The open biomedical engineering journal* 2010;4:27.

[142] Prakash P, Diederich CJ. Considerations for theoretical modelling of thermal ablation with catheter-based ultrasonic sources: Implications for treatment planning, monitoring and control. *Int J Hyperthermia* 2012;28:69-86.

[143] Yang D, Converse MC, Mahvi DM, Webster JG. Expanding the bioheat equation to include tissue internal water evaporation during heating. *Biomedical Engineering, IEEE Transactions on* 2007;54:1382-88.

[144] Wood BJ, Locklin JK, Viswanathan A, Kruecker J, Haemmerich D, Cebral J et al. Technologies for guidance of radiofrequency ablation in the multimodality interventional suite of the future. *J Vasc Interv Radiol* 2007;18:9-24.

[145] Goldberg SN, Hahn PF, Tanabe KK, Mueller PR, Schima W, Athanasoulis CA et al. Percutaneous radiofrequency tissue ablation: Does perfusion-mediated tissue cooling limit coagulation necrosis? *J Vasc Interv Radiol* 1998 1//;9:101-11.

[146] Deng Z-S, Liu J, Wang H-W. Disclosure of the significant thermal effects of large blood vessels during cryosurgery through infrared temperature mapping. *International Journal of Thermal Sciences* 2008 2008;47:530-45.

[147] Kou H-S, Shih T-C, Lin W-L. Effect of the directional blood flow on thermal dose distribution during thermal therapy: An application of a Green's function based on the porous model. *Phys Med Biol* 2003;48:1577.

[148] Pennes HH. Analysis of tissue and arterial blood temperatures in the resting human forearm. *J Appl Physiol* 1948;1:93-122.

[149] Charny CK. Mathematical models of bioheat transfer. *Advances in heat transfer* 1992;22:19-155.

[150] Chen MM, Holmes KR. Microvascular contributions in tissue heat transfer. *Ann N Y Acad Sci* 1980;335:137-50.

[151] Chato J. Fundamentals of bioheat transfer. *Thermal dosimetry and treatment planning*. New York: Springer; 1990. p. 1-56.

[152] Crezee J, Lagendijk J. Temperature uniformity during hyperthermia: The impact of large vessels. *Phys Med Biol* 1992;37:1321.

[153] Audigier C, Mansi T, Delingette H, Rapaka S, Mihalef V, Sharma P et al. Lattice-Boltzmann method for fast patient-specific simulation of liver tumor ablation from CT images. 2013.

[154] Rieder C, Kroeger T, Schumann C, Hahn HK. GPU-based real-time approximation of the ablation zone for radiofrequency ablation. *Visualization and Computer Graphics, IEEE Transactions on* 2011;17:1812-21.

[155] Bossy E, Padilla F, Peyrin F, Laugier P. Three-dimensional simulation of ultrasound propagation through trabecular bone structures measured by synchrotron microtomography. *Phys Med Biol* 2005;50:5545-56.

[156] Kaufman JJ, Luo G, Siffert RS. Ultrasound simulation in bone. *IEEE Trans Ultrason, Ferroelectr, Freq Control* 2008;55:1205-18.

[157] Fujii M, Sakamoto K, Toda Y, Negishi A, Kanai H. Study of the cause of the temperature rise at the muscle-bone interface during ultrasound hyperthermia. *IEEE Trans Biomed Eng* 1999;46:494-504.

[158] Behnia S, Jafari A, Ghalichi F, Bonabi A. Finite-element simulation of ultrasound brain surgery: Effects of frequency, focal pressure, and scanning path in bone-heating reduction. *Cent Eur J Phys* 2008;6:211-22.

[159] Burtnyk M, Chopra R, Bronskill M. Simulation study on the heating of the surrounding anatomy during transurethral ultrasound prostate therapy: A 3D theoretical analysis of patient safety. *Med Phys* 2010;37:2862-75.

[160] Wootton JH, Ross AB, Diederich CJ. Prostate thermal therapy with high intensity transurethral ultrasound: The impact of pelvic bone heating on treatment delivery. *Int J Hyperthermia* 2007;23:609-22.

[161] Moros EG, Straube WL, Myerson RJ, Fan X. The impact of ultrasonic parameters on chest wall hyperthermia. *Int J Hyperthermia* 2000;16:523-38.

[162] Li J-L, Liu X-Z, Zhang D, Gong X-F. Influence of ribs on the nonlinear sound field of therapeutic ultrasound. *Ultrasound Med Biol* 2007;33:1413-20.

[163] Sun J, Hynynen K. Focusing of therapeutic ultrasound through a human skull: A numerical study. *J Acoust Soc Am* 1998;104:1705-15.

[164] Gélat P, Haar Gt, Saffari N. Modelling of the acoustic field of a multi-element HIFU array scattered by human ribs. *Phys Med Biol* 2011;56:5553-81.

[165] Moros EG, Fan X, Straube WL. Ultrasound power deposition model for the chest wall. *Ultrasound Med Biol* 1999;25:1275-87.

[166] Lu B-Y, Yang R-S, Lin W-L, Cheng K-S, Wang C-Y, Kuo T-S. Theoretical study of convergent ultrasound hyperthermia for treating bone tumors. *Med Eng Phys* 2000;22:253-63.

[167] Staruch R, Chopra R, Hynynen K. Hyperthermia in bone generated with MR imaging-controlled focused ultrasound: Control strategies and drug delivery. *Radiology* 2012.

[168] Ryan TP, Patel SJ, Morris R, Hoopes PJ, Bergeron JA, Mahajan R, editors. Three-dimensional finite element simulations of vertebral body thermal treatment. Proc SPIE; 2005: 137-55.

[169] Bien T, Rose G, Skalej M, editors. FEM modeling of radio frequency ablation in the spinal column. Biomedical Engineering and Informatics (BMEI), 2010 3rd International Conference on; 2010: 1867-71: IEEE.

[170] Scott SJ, Prakash P, Salgaonkar V, Jones PD, Cam RN, Han M et al. Approaches for modeling interstitial ultrasound ablation of tumors within or adjacent to bone: Theoretical and experimental evaluations. *Int J Hyperthermia* 2013;29:629–42.

[171] Scott SJ, Prakash P, Salgaonkar V, Jones PD, Cam RN, Han M et al., editors. Interstitial ultrasound ablation of tumors within or adjacent to bone: Contributions of preferential heating at the bone surface. SPIE BiOS; 2013: 85840Z-1-40Z-12: International Society for Optics and Photonics.

[172] Scott SJ, Salgaonkar V, Prakash P, Burdette EC, Diederich CJ. Interstitial ultrasound ablation of vertebral and paraspinal tumors: Parametric and patient specific simulations. *In review*.

[173] Lin W-L, Liauh C-T, Chen Y-Y, Liu H-C, Shieh M-J. Theoretical study of temperature elevation at muscle/bone interface during ultrasound hyperthermia. *Med Phys* 2000;27:1131-40.

[174] Wu J, Du G. Temperature elevation generated by a focused Gaussian ultrasonic beam at a tissue-bone interface. *J Acoust Soc Am* 1990;87:2748-55.

[175] Werner J, Buse M. Temperature profiles with respect to inhomogeneity and geometry of the human body. *J Appl Physiol* 1988;65:1110-18.

[176] Williams LR, Leggett RW. Reference values for resting blood flow to organs of man. *Clin Phys Physiol Meas* 1989;10:187-217.

[177] Hakulinen MA, Day JS, Töyräs J, Timonen M, Kröger H, Weinans H et al. Prediction of density and mechanical properties of human trabecular bone in vitro by using ultrasound transmission and backscattering measurements at 0.2–6.7 MHz frequency range. *Phys Med Biol* 2005;50:1629-42.

[178] Calttenburg R, Cohen J, Conner S, Cook N. Thermal properties of cancellous bone. *J Biomed Mater Res* 1975;9:169-82.

[179] McCarthy I. The physiology of bone blood flow: A review. *J Bone Joint Surg Am* 2006;88:4-9.

[180] Wu J, Cubberley F. Measurement of velocity and attenuation of shear waves in bovine compact bone using ultrasonic spectroscopy. *Ultrasound Med Biol* 1997;23:129-34.

[181] Chen X, Diederich CJ, Wootton JH, Pouliot J, Hsu I-C. Optimisation-based thermal treatment planning for catheter-based ultrasound hyperthermia. *Int J Hyperthermia* 2010;26:39-55.

[182] Wootton JH, Prakash P, Hsu I-CJ, Diederich CJ. Implant strategies for endocervical and interstitial ultrasound hyperthermia adjunct to HDR brachytherapy for the treatment of cervical cancer. *Phys Med Biol* 2011;56:3967.

[183] Prakash P, Salgaonkar VA, Clif Burdette E, Diederich CJ. Multiple applicator hepatic ablation with interstitial ultrasound devices: Theoretical and experimental investigation. *Med Phys* 2012;39:7338-49.

[184] Nyborg WL. Heat generation by ultrasound in a relaxing medium. *The Journal of the Acoustical Society of America* 1981;70:310.

[185] Tyréus PD, Diederich CJ. Theoretical model of internally cooled interstitial ultrasound applicators for thermal therapy. *Phys Med Biol* 2002;47:1073-89.

[186] Cheeke JDN. *Fundamentals and Applications of Ultrasonic Waves*. Boca Raton, FL: CRC Press, 2012.

[187] Riekkinen O, Hakulinen M, Timonen M, Töyräs J, Jurvelin J. Influence of overlying soft tissues on trabecular bone acoustic measurement at various ultrasound frequencies. *Ultrasound Med Biol* 2006;32:1073-83.

[188] Vaupel P, Kallinowski F, Okunieff P. Blood flow, oxygen and nutrient supply, and metabolic microenvironment of human tumors: A review. *Cancer Res* 1989;49:6449-65.

[189] Gerweck LE. Hyperthermia in cancer therapy: The biological basis and unresolved questions. *Cancer Res* 1985;45:3408-14.

[190] King RL, Liu YL, Maruvada S, Herman BA, Wear KA, Harris GR. Development and characterization of a tissue-mimicking material for high intensity focused ultrasound. *IEEE Trans Ultrason, Ferroelectr, Freq Control* 2011;58:1397-405.

[191] Kinsey AM, Diederich CJ, Rieke V, Nau WH, Butts Pauly K, Bouley D et al. Transurethral ultrasound applicators with dynamic multi-sector control for prostate thermal therapy: In vivo evaluation under MR guidance. *Med Phys* 2008;35:2081-93.

[192] Roujol S, Ries M, Quesson B, Moonen C, Denis de Senneville B. Real-time MR-thermometry and dosimetry for interventional guidance on abdominal organs. *Magn Reson Med* 2010;63:1080-87.

[193] Buccella C, De Santis V, Feliziani M. Prediction of temperature increase in human eyes due to RF sources. *IEEE Trans Electromagn Compat* 2007;49:825-33.

[194] Wang J, Fujiwara O. FDTD computation of temperature rise in the human head for portable telephones. *IEEE Trans Microw Theory Techn* 1999;47:1528-34.

[195] Diederich C, Nau W, Ross A, Tyreus P, Butts K, Rieke V et al. Catheter-based ultrasound applicators for selective thermal ablation: Progress towards MRI-guided applications in prostate. *Int J Hyperthermia* 2004;20:739-56.

[196] Gandhi S, Daniel B, Butts K, editors. Temperature dependence of relaxation times in bovine adipose tissue. Proceedings of the 6th Annual Meeting of ISMRM, Sydney, Australia; 1998: Wiley Online Library.

[197] Peller M, Reinl HM, Weigel A, Meininger M, Issels RD, Reiser M. T1 relaxation time at 0.2 Tesla for monitoring regional hyperthermia: Feasibility study in muscle and adipose tissue. *Magn Reson Med* 2002;47:1194-201.

[198] Kubo T, Fujimori K, Cazier N, Saeki T, Matsukawa M. Properties of ultrasonic waves in bovine bone marrow. *Ultrasound Med Biol* 2011;37:1923-29.

[199] Bamber J, Hill C. Ultrasonic attenuation and propagation speed in mammalian tissues as a function of temperature. *Ultrasound Med Biol* 1979;5:149-57.

[200] Brace CL, Diaz TA, Hinshaw JL, Lee FT. Tissue contraction caused by radiofrequency and microwave ablation: A laboratory study in liver and lung. *J Vasc Interv Radiol* 2010;21:1280-86.

[201] Moros EG, Novak P, Straube WL, Kolluri P, Yablonskiy DA, Myerson RJ. Thermal contribution of compact bone to intervening tissue-like media exposed to planar ultrasound. *Phys Med Biol* 2004;49:869-86.

[202] Haws CW, Heistad DD. Effects of nimodipine on cerebral vasoconstrictor responses. *Am J Physiol Heart Circ Physiol* 1984;247:H170-H76.

[203] *CRC Handbook of Chemistry and Physics 2012-2013*. 93rd ed. Boca Raton, FL: CRC Press/Taylor and Francis, 2012.

[204] Zachos TA, Aiken SW, DiResta GR, Healey JH. Interstitial fluid pressure and blood flow in canine osteosarcoma and other tumors. *Clin Orthop Relat Res* 2001;385:230-36.

[205] Masala S, Roselli M, Manenti G, Mammucari M, Bartolucci DA, Simonetti G. Percutaneous cryoablation and vertebroplasty: A case report. *Cardiovasc Intervent Radiol* 2008;31:669-72.

[206] Töyräs J, Laasanen MS, Saarakkala S, Lammi MJ, Rieppo J, Kurkijärvi J et al. Speed of sound in normal and degenerated bovine articular cartilage. *Ultrasound Med Biol* 2003;29:447-54.

[207] Sierra G, Leung M, Le Guyader P, Savard P, editors. Thermal and electrical characterization of the intervertebral disc. Proceedings of the 25th Annual International Conference of the IEEE Engineering in Medicine and Biology Society; 2003: 3035-36: IEEE.

[208] Urban JPG, Smith S, Fairbank JCT. Nutrition of the intervertebral disc. *Spine* 2004;29:2700-09.

[209] McFadden ER, Pichurko BM, Bowman HF, Ingenito E, Burns S, Dowling N et al. Thermal mapping of the airways in humans. *J Appl Physiol* 1985;58:564-70.

[210] Poutanen T, Tikanoja T, Sairanen H, Jokinen E. Normal aortic dimensions and flow in 168 children and young adults. *Clinical physiology and functional imaging* 2003;23:224-29.

[211] Wexler L, Bergel DH, Gabe IT, MAKIN GS, MILLS CJ. Velocity of blood flow in normal human venae cavae. *Circ Res* 1968;23:349-59.

[212] Azhim A, Katai M, Akutagawa M, Hirao Y, Yoshizaki K, Obara S et al. Exercise improved age-associated changes in the carotid blood velocity waveforms. *Journal of Biomedical & Pharmaceutical Engineering* 2007;1:17-26.

[213] Haemmerich D, Wright AW, Mahvi DM, Lee FT, Webster JG. Hepatic bipolar radiofrequency ablation creates coagulation zones close to blood vessels: A finite element study. *Med Biol Eng Comput* 2003;41:317-23.

[214] Sutphen SA, Murakami JW. Radiofrequency ablation of a cervical osteoid osteoma: A trans-thyroid approach. *Pediatr Radiol* 2007;37:83-85.

[215] Tateishi U, Gamez C, Dawood S, Yeung HWD, Cristofanilli M, Macapinlac HA. Bone metastases in patients with metastatic breast cancer: Morphologic and metabolic monitoring of response to systemic therapy with integrated PET/CT1. *Radiology* 2008;247:189-96.

[216] Costelloe CM, Chuang HH, Madewell JE, Ueno NT. Cancer response criteria and bone metastases: RECIST 1.1, MDA and PERCIST. *J Cancer* 2010;1:80.

[217] Debnam JM, Guha-Thakurta N, Mahfouz YM, Garden AS, Benjamin RS, Sturgis EM et al. Radiation-associated head and neck sarcomas: Spectrum of imaging findings. *Oral Oncol* 2012;48:155-61.

[218] Ahrar K, Stafford RJ. Magnetic resonance imaging–guided laser ablation of bone tumors. *Techniques in Vascular and Interventional Radiology* 2011;14:177-82.

[219] Adachi A, Kaminou T, Ogawa T, Kawai T, Takaki Y, Sugiura K et al. Heat in spinal canal during radiofrequency ablation for vertebral lesions: Study in swine. *Radiology* 2008;247:374-80.

[220] Clarençon F, Jean B, Pham H-P, Cormier E, Bensimon G, Rose M et al. Value of percutaneous radiofrequency ablation with or without percutaneous vertebroplasty for pain relief and functional recovery in painful bone metastases. *Skeletal Radiol* 2013;42:25-36.

[221] Chen W, Zhu H, Zhang L, Li K, Su H, Jin C et al. Primary bone malignancy: Effective treatment with high-intensity focused ultrasound ablation. *Radiology* 2010;255:967-78.

[222] Nakatsuka A, Yamakado K, Takaki H, Uraki J, Makita M, Oshima F et al. Percutaneous radiofrequency ablation of painful spinal tumors adjacent to the spinal cord with real-time

monitoring of spinal canal temperature: A prospective study. *Cardiovasc Intervent Radiol* 2009;32:70-75.

[223] Leslie T, Kennedy J, Illing R, Ter Haar G, Wu F, Phillips R et al. High-intensity focused ultrasound ablation of liver tumours: Can radiological assessment predict the histological response? *Br J Radiol* 2008;81:564-71.

[224] Wood BJ, Kruecker J, Abi-Jaoudeh N, Locklin JK, Levy E, Xu S et al. Navigation systems for ablation. *J Vasc Interv Radiol* 2010;21:S257-S63.

[225] Guiot C, Pastore G, Napoleone M, Gabriele P, Trotta M, Cavalli R. Thermal response of contrast agent microbubbles: Preliminary results from physico-chemical and US-imaging characterization. *Ultrasonics* 2006;44:e127-e30.

[226] Díaz-López R, Tsapis N, Fattal E. Liquid perfluorocarbons as contrast agents for ultrasonography and 19F-MRI. *Pharm Res* 2010;27:1-16.

[227] Cosgrove D, Eckersley R. Contrast-enhanced ultrasound: Basic physics and technology overview. *Enhancing the Role of Ultrasound with Contrast Agents*. Milan: Springer; 2006. p. 3-14.

[228] Giesecke T, Hynynen K. Ultrasound-mediated cavitation thresholds of liquid perfluorocarbon droplets *in vitro*. *Ultrasound Med Biol* 2003;29:1359-65.

[229] Kripfgans OD, Fowlkes JB, Miller DL, Eldevik OP, Carson PL. Acoustic droplet vaporization for therapeutic and diagnostic applications. *Ultrasound Med Biol* 2000;26:1177-89.

[230] Rapoport NY, Efros AL, Christensen DA, Kennedy AM, Nam K-H. Microbubble generation in phase-shift nanoemulsions used as anticancer drug carriers. *Bubble Sci Eng Technol* 2009;1:31.

[231] Fabiilli ML, Haworth KJ, Fakhri NH, Kripfgans OD, Carson PL, Fowlkes JB. The role of inertial cavitation in acoustic droplet vaporization. *Ultrasonics, Ferroelectrics and Frequency Control, IEEE Transactions on* 2009;56:1006-17.

[232] Rapoport NY, Kennedy AM, Shea JE, Scaife CL, Nam K-H. Controlled and targeted tumor chemotherapy by ultrasound-activated nanoemulsions/microbubbles. *J Control Release* 2009;138:268-76.

[233] Bhowmick P, Coad J, Bhowmick S, Pryor J, Larson T, De La Rosette J et al. In vitro assessment of the efficacy of thermal therapy in human benign prostatic hyperplasia. *Int J Hyperthermia* 2004;20:421-39.

Appendix A

Calculation of heat deposition in patient-specific models of tissue

A.1 Introduction

Due to the high ultrasound absorption coefficient of bone, 7 MHz acoustic waves that enter bone are rapidly absorbed over the first few millimeters. To accurately model heat deposition in bone, the surface of the bone must be clearly identified, and the depth the wave has travelled from the bone surface must be precisely calculated. The attenuation and transmission coefficients over inhomogeneous tissues must also be determined. In patient-specific models with irregular geometries, this is not as straightforward as in cases with planar or cylindrical bone surfaces, in which heat deposition can be calculated analytically.

A.2 Discretization of heat deposition calculations

Heat deposition Q (W/m^3) in tissue from a well-collimated cylindrical source can be approximated using Equation 2.10:

$$Q = 2\mathcal{T}\alpha I_s \frac{r_t}{r} e^{-2\int_{r_t}^{r} \mu dr'} \quad 2.10$$

where $\mathcal{T}$ is the acoustic transmission coefficient (unitless), α is the ultrasound absorption coefficient (Np/m), I_s is the acoustic intensity on the transducer surface (W/m^2), r_t is the transducer radius (m), r is the radial distance from the transducer's central axis (m), and μ is the ultrasound attenuation coefficient (Np/m). The absorption coefficient is assumed to be equivalent to the attenuation coefficient, with scattered energy locally absorbed.

To calculate heat deposition in irregular patient-specific geometries, this equation can be discretized over a cylindrical grid (r, θ, z) defined in relation to the central axis of the applicator (z). The heat deposition at the ith radial coordinate, the jth coordinate in θ, and the kth coordinate in z, can be calculated as:

$$Q_{i,j,k} = 2\mathcal{T}_{i,j,k}\alpha_{i,j,k} I_s \frac{r_t}{r_{i,j,k}} e^{-2((\sum_{a=2}^{i} \mu_{a,j,k}\Delta r_{a,j,k}) + \mu_{catheter}(r_0 - r_c))} \quad A.1$$

where r, the radial distance from the center of the transducer axis, ranges from the radius of the catheter at $a = 1$ to the radial location of the given point at $a = i$. $\Delta r_{i,j,k}$ is defined as $\Delta r_{i,j,k} - \Delta r_{i-1,j,k}$. The exponential attenuation term is assumed to be equal to a factor of 1 at $i = 1$. Q is assumed to be 0 for all z-coordinates outside the span of the transducers. Once Q is calculated on a discrete grid, the value of Q at any point in the tissue can then be found through interpolation.

In homogenous soft tissues, Q can be calculated on a nearly uniform cylindrical grid around the applicator. The grid spacing in θ and z can be constant, with Δz of ~0.5 mm and $\Delta\theta$

of ~3-5°. Because Q is assumed to be symmetrical in θ and z, but widely varying in r, a finer grid spacing in the r dimension is used. In soft tissue, temperature peaks about 6 mm from the center of the catheter (Figure 3.8), so the radial spacing Δr needs to be small (~0.2-0.4 mm) near the catheter, and can be wider further away without any significant loss in accuracy, as determined through parametric convergence studies.

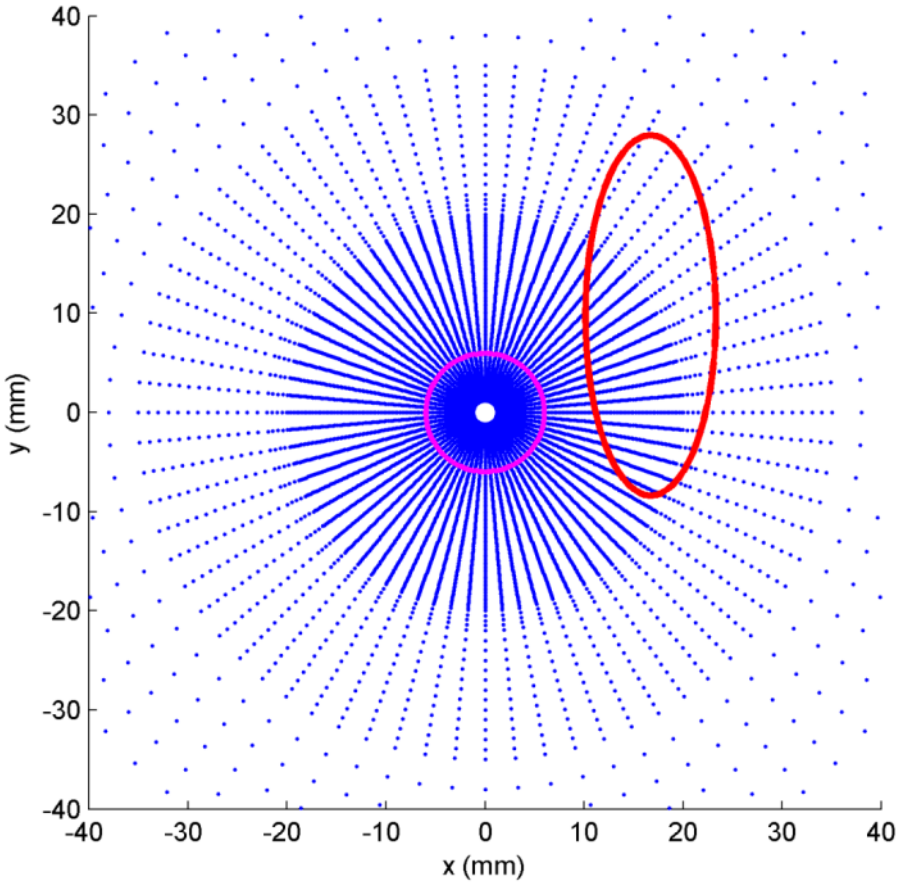

Figure A.1 A radial grid around an applicator placed at (0,0), over which heat deposition in homogenous tissue may be sampled. In soft tissue, temperature peaks about 6 mm (magenta circle) from the applicator's center. A high sampling rate is needed near this peak. However, a radial grid uniform in θ and z, unless it is very fine, can be insufficient for sampling the heating at bone surfaces. Consider the oval bone surface outlined in red, for example. The bone surface may be undersampled in r, as well as in θ and z between radial lines.

However, when bone is present, significant heating occurs along any bone surfaces within a few centimeters of the applicator. The heat deposition in bone drops off very quickly

behind the bone surface, so a very fine radial spacing behind the bone surface (less than 0.2 mm, preferably ~0.025 mm) is necessary to capture this. Fine grid spacing near the catheter is usually insufficient. The location of irregularly shaped and highly heated bone surfaces can vary in r, θ, and z, so the spacing of a cylindrical grid (Δr, $\Delta\theta$, Δz) would have to be very small (~0.025 mm) in large fields of view (~70 mm diameter) to be able to accurately describe heat deposition in irregular bones. Such a small grid would require more computer memory than is allocated to the system used in this work.

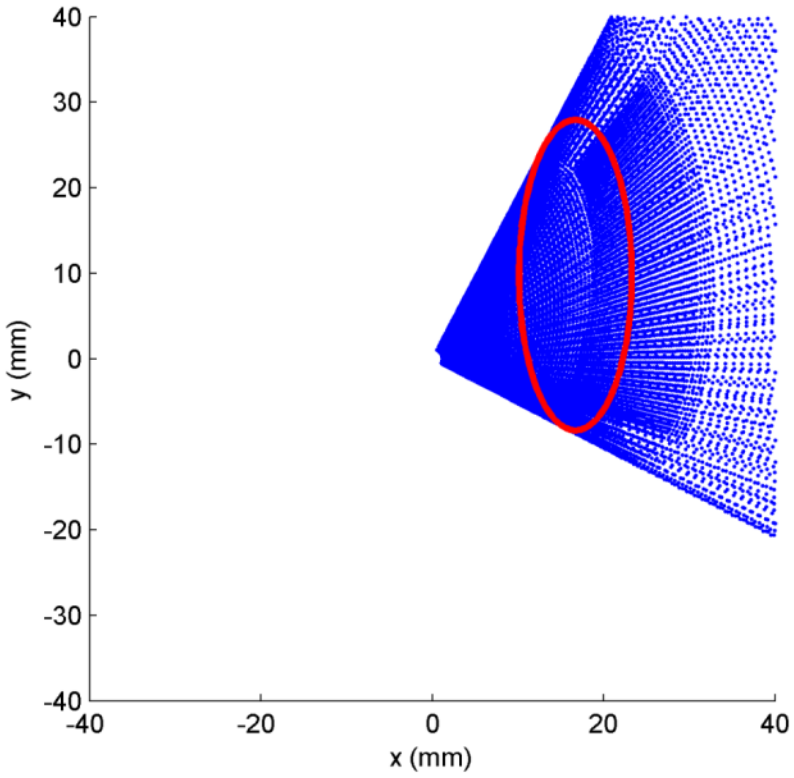

Figure A.2 Radial lines defined relative to triangular elements on the bone surface. Higher sampling rates are employed near heated bone surfaces where it is necessary.

Instead of calculating heat deposition on a uniform cylindrical grid, heat deposition in patient-specific anatomies was calculated on grids defined relative to tissue surfaces. Heat deposition in bone, tumor tissue, and other tissues were each calculated separately. For each tissue, the (r, θ, z) coordinates of each triangular element on the finite element meshes of the

tissue surfaces were imported from Comsol into MATLAB. For each triangular surface element with coordinates θ and z, attenuation and transmission were computed along a radial line from the catheter surface to through the triangular element, as acoustic energy was assumed to propagate radially outward from the cylindrical transducer surface. Each radial line was discretized into small segments. Since the location of bone and soft tissue surfaces were known, the segment sizes were made to be finer near bone surfaces than within soft tissues.

A.3 Heat deposition in tumor tissue

In the patient-specific models presented in Chapter 5, the applicator was inserted into the tumors to be treated. In some tumors, such as that shown in Case 1 (Figure 5.2), the acoustic beam reached all parts of the tumor without traversing tissues with disparate acoustic properties. In these cases, heat deposition in the tumor could be calculated analytically using Equation 2.23. In other cases, such as Case 4 (Figure 5.5), the beam had to traverse inhomogeneous tissues to reach some portions of the tumor. In these cases, attenuation and transmission coefficients considering inhomogeneous tissue types were calculated over a discretized radial grid, as described below.

Heat deposition in these tumors was calculated along radial lines from the catheter surface to the tumor surface. For each triangular element on the tumor surface with coordinates (r, θ, z), the radial line drawn to the catheter surface was constant in θ and z. The triangular elements were ~0.5 mm wide, resulting in finely spaced radial lines. Each line was divided into segments with a small Δr (0.2 - 0.5 mm). A finer spacing of Δr was used within 5 mm of the tumor surface (~0.025 - 0.1 mm).

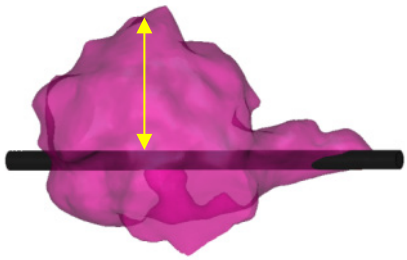

Figure A.3 For each triangle on the tumor surface (magenta), a radial line was drawn from the triangular element to the catheter surface (black).

The acoustic attenuation coefficient at all points on the radial lines, which had been defined for each organ in Comsol, was imported into MATLAB. Attenuation was then summated over space, as in Equation A.1.

To find the percentage of the energy that is transmitted to a given point, the acoustic impedance Z (kg/m^{2}s) was determined based on the density and speed of sound of the given material as defined within Comsol.

$$Z = \rho c \tag{A.2}$$

where ρ is density (kg/m^3), and c is the speed of sound (m/s). The transmission coefficient ($\mathcal{T}$) in the various tissues was then calculated as:

$$\mathcal{T}_{i,j,k} = \begin{cases} 1, & a = 1 \\ \prod_{a=2}^{i} \frac{4Z_{\mathrm{a},j,k}Z_{a-1,j,k}}{\left(Z_{\mathrm{a},j,k} + Z_{a-1,j,k}\right)^2}, & a \neq 1 \end{cases} \tag{A.3}$$

with Z at the catheter surface assumed to be the same as that of muscle. The heat deposition in the tumor at each point on the radial lines was then calculated using Equation A.1.

A.4 Heat deposition in bone and healthy soft tissue

Heat deposition in bone was calculated along radial lines extending from the catheter surface, through each triangular element on heated bone surfaces, and past the outer boundaries of the volume that was considered. z and θ were constant along each line. Each line was divided into small segments, with a point on the bone surface. Δr was set to be moderate (~0.3-0.8 mm) far in front of the bone surface, fine (~0.025 mm) within a few millimeters of either side of the bone surface, moderate (< 1 mm) less ~3 cm behind the bone surface, and wide far behind bone surface.

Heat deposition in the soft tissues modeled in Chapter 5 was generally calculated in a similar manner. However, the radial spacing Δr behind the soft tissue surface was wider (~0.2 mm) than that for bone, because the acoustic beam is not attenuated as rapidly in soft tissue.

In the *ex vivo* soft tissues imaged with MR in Chapter 3, the applicator was placed in the soft tissue above bone. Because of this placement, a near-uniform radial grid around the applicator, such as that shown in Figure A.1, was appropriate for modeling heat deposition in soft tissue. Heat deposition in bone, however, was modeled using radial grids defined in relation to the bone surface, as shown in Figure A.2.

Appendix B

Exploration of phase-shift ultrasound contrast agents for monitoring interstitial ultrasound ablation of tumors near bone

B.1 Introduction

Thermal ablation in the vicinity of the spine must be carefully monitored to ensure full treatment of the target and to prevent damage to nearby sensitive anatomy. Ablation of bone tumors is currently guided using MR temperature imaging (MRTI) in adjacent soft tissues [11], ultrasound in adjacent soft tissues (for HIFU) [221], or invasive temperature sensors placed adjacent to sensitive structures [222]. Invasive sensors only measure temperature at a few points, and they must be precisely inserted into delicate regions such as the spinal canal. MRTI is noninvasive and provides temperature measurements throughout a soft tissue volume, but is expensive, less sensitive than invasive measurements, and highly complex. Furthermore, MRTI requires that all heating apparatus be nonmagnetic. Ultrasound guidance of HIFU is based on changes in gray-

scale images that are assumed to be due to boiling and cavitation [223], which are avoided, and thus not applicable, with 7 MHz interstitial ultrasound. An ultrasound-based method of monitoring interstitial ultrasound ablation could be cheaper and simpler than MRTI, while maintaining the advantages of noninvasiveness and data throughout soft tissues. It could also be performed using the same probe used to monitor applicator placement, which can be guided using ultrasound, CT, fluoroscopic, or other imaging modalities [224].

Although several acoustic characteristics of biological tissues are temperature-dependent, such as the speed of sound and backscattering properties, variability of these properties among different tissues makes them difficult to apply to temperature monitoring [225]. Contrast-enhanced ultrasound (CEUS) can be used to identify where vasculature has been coagulated [139], cutting off blood flow, but this is not useful for moderate temperature increases, and cell death can occur without immediate coagulation of the vasculature [25].

Figure B.1 The volatile cores of the microcapsules investigated herein vaporize upon heating.

Ultrasound contrast agents that undergo a phase change upon reaching a temperature threshold, such as those developed by Huang et al., could potentially be used to monitor thermal therapy. Most commercial contrast agents consist of gaseous microbubbles (<7 μm), which are highly echogenic [226, 227]. These microbubbles are encapsulated within stabilizing shells composed of a polymer, phospholipid, or other material [226, 227]. The contrast agent developed by Huang et al. consists of 1.6 μm microcapsules containing 2H-, 3H-

perfluoropentane, a liquid perfluorocarbon (PFC), encapsulated in a polymer shell. The liquid core vaporizes when heated, forming gaseous microbubbles that are highly echogenic under ultrasound imaging.

These microcapsules are in the early stages of development. It is known that when they are heated to the boiling point of the encapsulated PFC (53.6°C), they physically grow and become bright under ultrasound. However, the exact temperature range over which this occurs is unknown.

The phase change temperature of liquid microdroplets is influenced by the stabilizing shell, which can significantly increase the vaporization temperature above that of the bulk fluid. Giesecke et al. found that 1.4-2 μm perflurocarbon droplets encased in albumin have vaporization temperatures 10-40°C or more higher than those of the bulk fluids [228]. Droplets containing the PFC perfluoropentane, which has a boiling point of 29°C at atmospheric pressure, and shells composed of albumin, lipids, or block copolymers (600 nm - 2 μm) are stable outside an acoustic field at physiological temperatures [229-231]. The Laplace pressure can result in higher vaporization temperatures of small particles stabilized by an outer shell so that they are stable in a physiological setting [230]:

$$\Delta P = P_{inner} - P_{outer} = \frac{2\sigma}{r} \tag{B.1}$$

where ΔP is the Laplace pressure, P_{inner} is the pressure inside the droplet, P_{outer} is the pressure outside the droplet, σ is the surface tension at the interface between the droplet and the bulk liquid, and r is the droplet's radius [232]. Hence, larger microcapsules and microcapsules containing PFCs with lower boiling points are expected to have lower vaporization temperatures [230].

The goal of this project is to determine the transition temperatures of two formulations of microcapsules, and to investigate their applicability in monitoring thermal ablation in soft tissue in the vicinity of the spine and other bones. Microcapsules with a temperature transition at 52°C could be applied to monitor the ablation zone. In the event that the Laplace pressure significantly raises the vaporization temperature of the microcapsules, formulations using a PFC with a boiling point below 52°C may be appropriate for monitoring ablation. In this study, microcapsules containing PFCs with boiling points of 44.8°C and 53.6°C were produced and their transition temperatures were measured. The stability of the microcapsules over time is also evaluated. If the Laplace pressure has little effect on the vaporization temperature, the particles with a 45°C transition threshold, which corresponds to the temperature at which the spinal canal can sustain damage [104], could be used to monitor sensitive anatomy and untargeted tissues.

B.2 Materials and Methods

B.2.1 Microcapsule production

Microcapsules containing a PFC with a boiling point of 53.6°C were produced based upon the methodology described by Huang et al. Microcapsules containing a PFC with a lower boiling point were also developed though modifications of these procedures. Poly(DL-lactic-co-glycolic acid) (PLGA) was used form the shell of the microcapsules, and either 1,1,2,2,3,3,4,4-octafluorobutane or 2H-, 3H-perfluoropentane (Synquest Labs, Inc., Alachua, FL) were used to form the volatile core of the microcapsules. 1,1,2,2,3,3,4,4-octafluorobutane and 2H-,3H-perfluoropentane are nontoxic perfluorocarbons with boiling points of 44.8°C and 53.6°C, respectively. 0.05 g of acid terminated PLGA was dissolved in 4 mL of methylene chloride. 2 mL of the selected PFC and 40 mL sodium cholate surfactant (1.5 w/v%) were added to the

solution. The mixture was emulsified for 2 minutes at 10,000 rpm to form microcapsules. It was then stirred for 3-4 hours to evaporate out the methylene chloride. Next, it was centrifuged for 10-12 min at 300-500 rpm to remove large particles from the suspension. Particles containing 1,1,2,2,3,3,4,4-octafluorobutane were centrifuged for 10 min at 500 rpm. The sizes of a diluted microcapsules suspension were measured using dynamic light scattering, performed by a Zetasizer 3000 or a Zetasizer Nano ZS, both by Malvern Instruments Ltd. (Malvern, Worcestershire, UK).

B.2.2 Transition temperature

To measure the transition temperature of the microcapsules containing a PFC with a boiling point of 53.6°C, they were pipetted into a 50 mL beaker of heated water and imaged with B-mode ultrasound. The beaker full of degassed water, the bottom of which was covered with acoustically absorbing rubber, was first placed in a heated water bath. The water level in the bath was kept below the rim of the beaker. The water in the beaker was slowly agitated by a stir bar. An ultrasound imaging probe was suspended above the beaker in a room-temperature water bath that acoustically coupled the ultrasound probe to the beaker of water and that kept the probe from overheating. A thin plastic film separated the cool water around the probe from the water in the beaker. 0.8 mL of the microcapsule suspension, initially at 12°C, was pipetted into the heated beaker of degassed water over a 3 second interval. The water was imaged before and after the addition of the microcapsules, and the temperature within the beaker was measured using a thermocouple at regular time intervals. The thermocouple was removed during imaging. 4-7 trials were done at each temperature. A control was performed in which 0.8 mL of tap water was pipetted into a beaker of water heated to 60°C, 45°C, or 25°C, with 2-4 trials at each temperature.

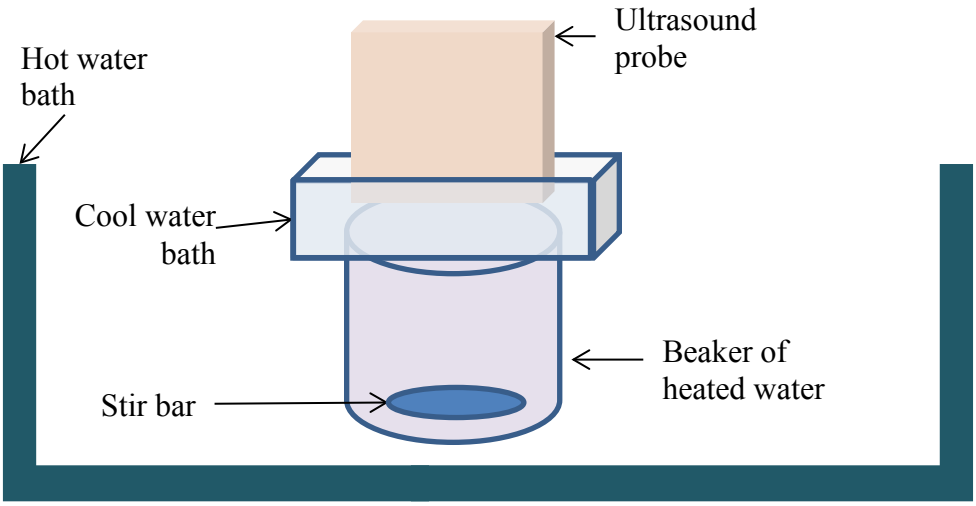

Figure B.2 Setup of experiments to measure transition temperature

Ultrasound images of the fluids were semi-automatically analyzed in MATLAB. The fluid containing microcapsules was identified by manually drawing a box over an image. The microcapsule signal was quantified as the mean intensity in this region of interest.

B.2.3 Microscopy

To visually observe the phase change of the microcapsules and to confirm the transition temperature under gradual heating, the microcapsules were heated under a microscope. A BC-100 bionomic controller and a HEC-400 heat exchanger (20/20 Technologies, Wilmington, NC) were used to heat a petri dish containing the microcapsules. Artic Silver 5, a high density polysynthetic silver thermal compound (RadioShack), was applied to ensure good thermal conduction between the heated stage and the bottom and sides of the petri dish. The microcapsules were gradually heated from room temperature to 60°C in 5°C increments, and any changes in size were visually observed.

B.2.4 Microcapsule stability

To determine the behavior of the microcapsules over long heating periods, they were mixed into an agar gel phantom and heated. To create the gels, 3 g of agar was added to 200 mL of boiling water. This solution was separated into two volumes, one to contain microcapsules with a 1,1,2,2,3,3,4,4-octafluorobutane core, and another to contain microcapsules with a 2H-,3H-perfluoropentane core. The solutions were stirred while they cooled. 1 mL of the microcapsule suspension was mixed into to each solution once it cooled to 36°C. The gel was then refrigerated overnight.

The phantoms were placed in a 10°C water bath, which was slowly heated in 5°C increments. Ultrasound images of the phantoms (<80 mL) were acquired after 20 minutes of thermal equilibration at each temperature point. Acoustic gel was used to couple the ultrasound probe to the phantoms. Images at each temperature were acquired in 10 locations.

Ultrasound images of the flow tube were semi-automatically analyzed in MATLAB. The portion of the images containing the phantom microcapsules was identified by manually drawing a box over each image. The microcapsule signal was quantified as the proportion of pixels in this region of interest over an intensity threshold that indicates presence of gas bubbles.

B.3 Results

B.3.1 Transition temperature

When rapidly heated, the microcapsules containing a PFC with a boiling point of 53.6°C had transition temperatures between 45 and 55°C. At and below 42°C, no increase in echogenicity was observed. Beginning at 44°C, mean intensity increased linearly with temperature. The mean intensity plateaued at ~55°C, and was constant above that temperature. No increases in

echogenicity were observed at any temperature in control experiments performed with tap water instead of a microcapsule suspension.

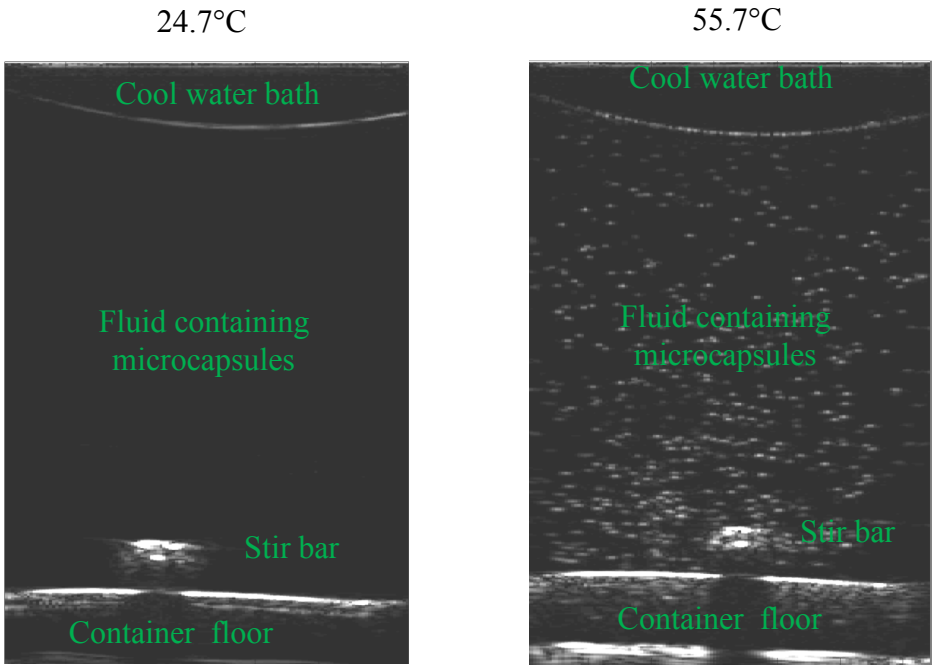

Figure B.3 B-mode images of particles in room temperature and heated water

When a suspension of microcapsules was pipetted into a beaker of heated water over a 3 second time frame, the ultrasound image intensity peaked 10-20 s after the mixing began, then rapidly decreased, plateauing 30-50 s after the mixing began. At temperatures over 50 degrees, the final image intensity after 60 s was higher than the initial intensity before the microcapsules were added.

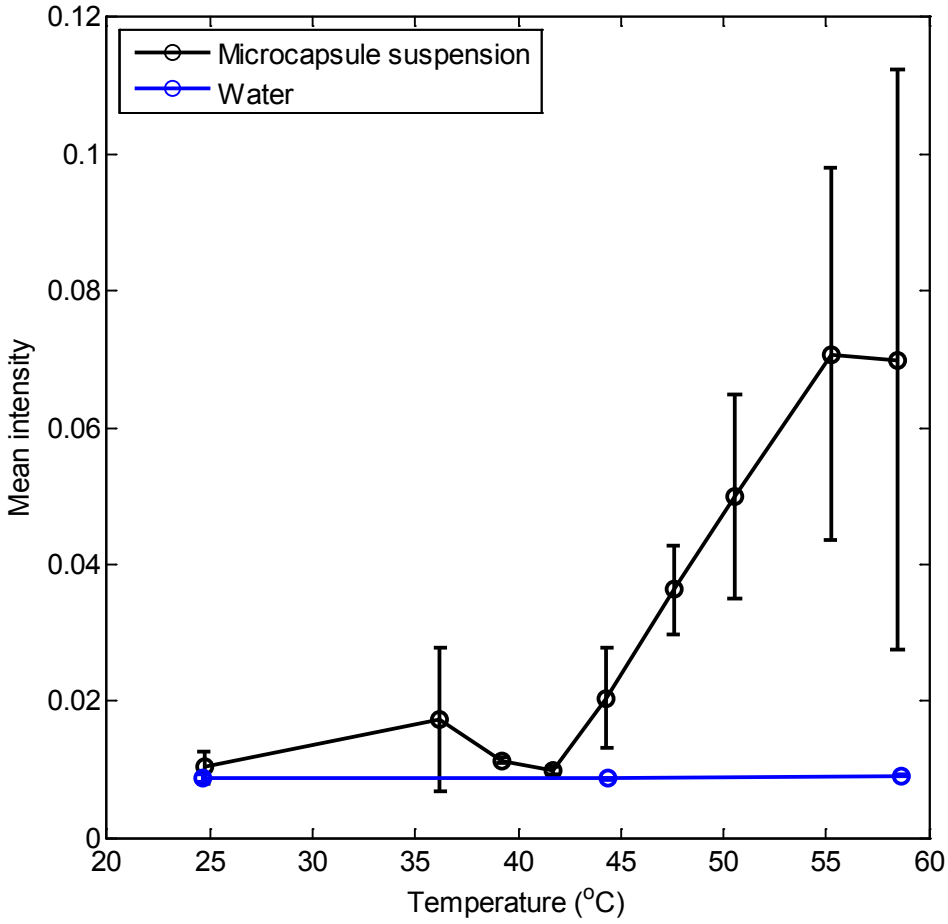

Figure B.4 Mean image intensity as a function of temperature. Error bars show standard deviation.

B.3.2 Transition temperature upon gradual temperature increases

When microcapsules were mixed into a phantom that was gradually heated over the course of several hours, transition temperatures much lower than the boiling points of the encapsulated perfluorocarbons were observed. Microcapsules containing a PFC that vaporizes at 45°C increased in echogenicity at 30°C. Microcapsules containing a perfluorocarbon that vaporizes at 54°C increased in echogenicity at 20°C. Phantoms containing a water control showed no change in echogenicity upon increases in temperature.

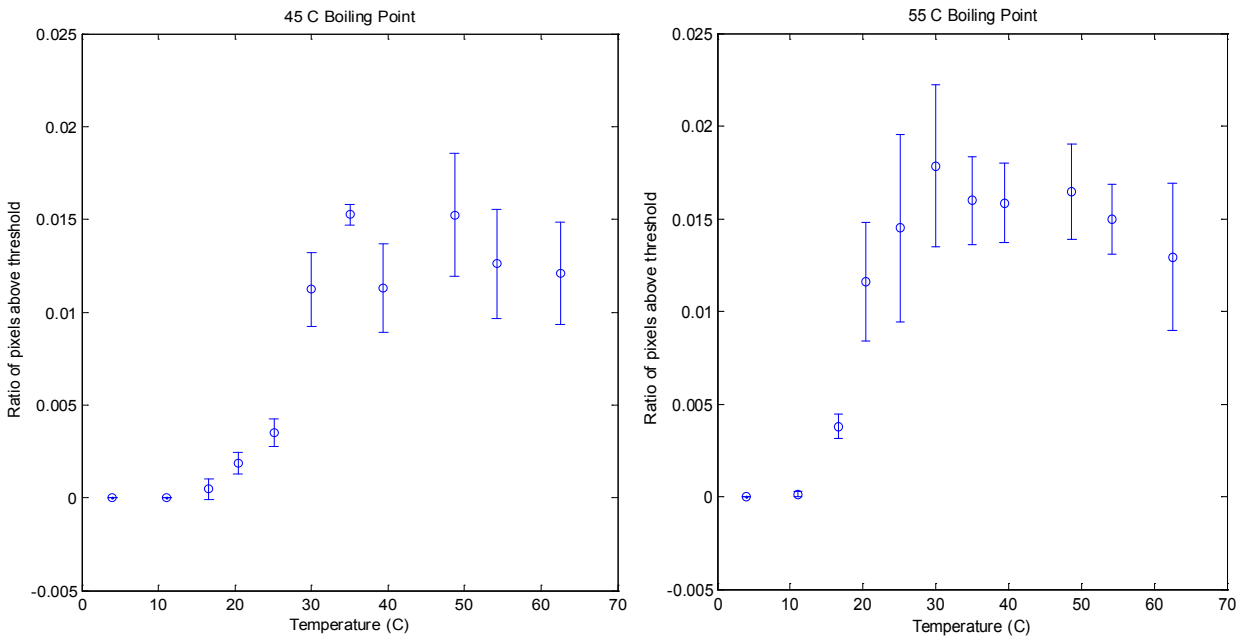

Figure B.5 Proportion of pixels in phantom with an intensity over a threshold. 10 images were taken at each temperature.

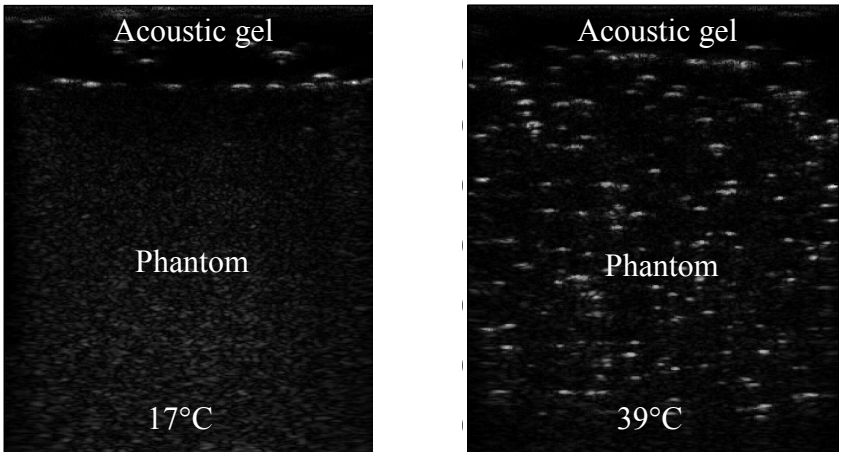

Figure B.6 Ultrasound images of a heated phantom containing microcapsules with a PFC core with a boiling point of 45°C.

Foam was observed in the microcapsule suspensions during the preparation of the phantoms, indicating that a portion of the microcapsules vaporized at room temperature. The microcapsules that were mixed into the phantoms were drawn from the bottom of the suspensions, away from the foam.

B.3.3 Microscopy

Upon heating from 25°C to 60°C, the microcapsules containing a perflurocarbon that boils at 45°C underwent significant changes in size at 27-30°C. The microcapsules did not behave in a uniform manner; some expanded earlier than others, and they did not expand to a uniform size.

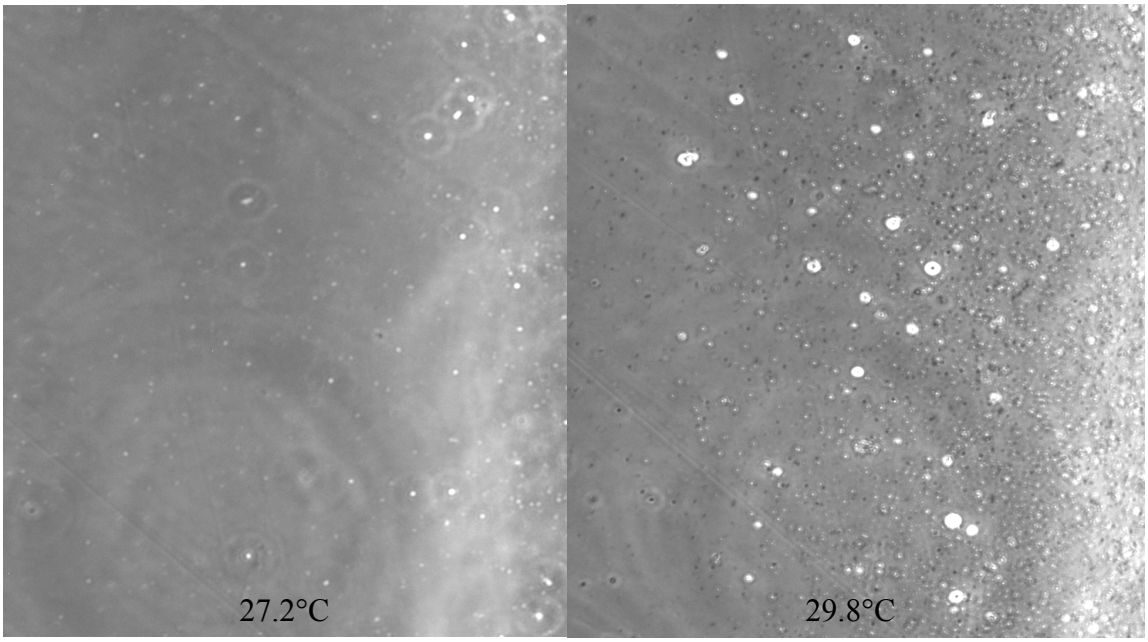

Figure B.7 Microcapsules containing a PFC with a boiling point of 45°C heated under microscope

Upon gradual heating to 60°C, only very slight changes in size were observed in microcapsules containing a perfluorocarbon with a boiling point of 54°C. The growth was much smaller than that expected upon vaporization.

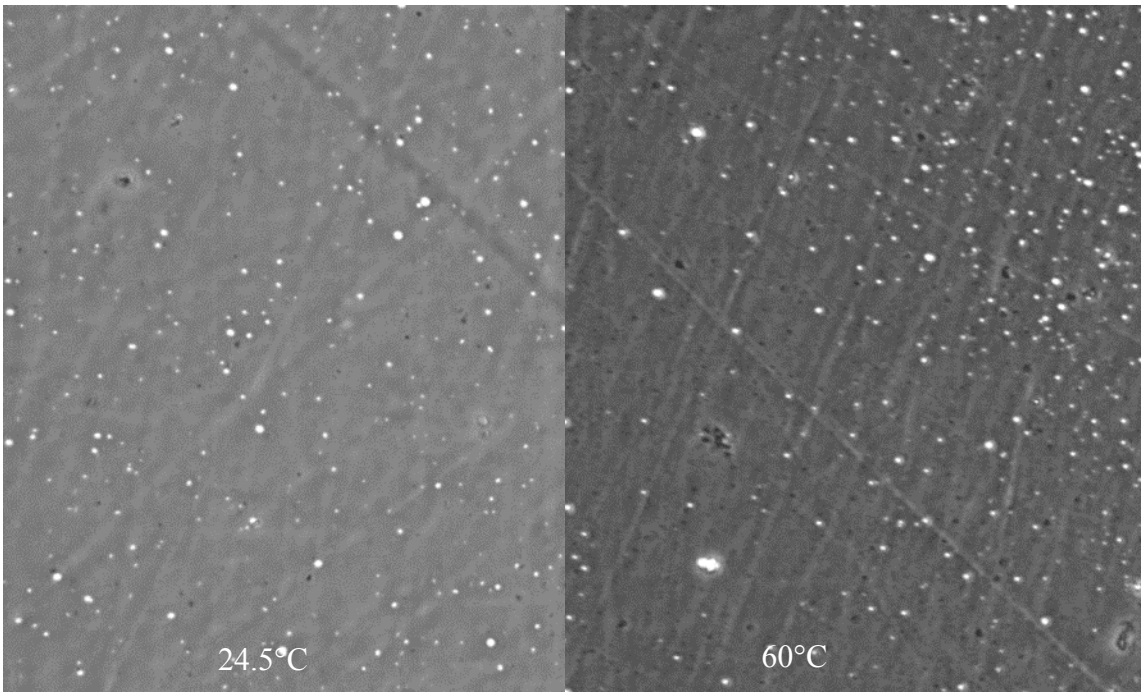

Figure B.8 Microcapsules containing a PFC with a boiling point of 54°C heated under microscope

B.4 Discussion and future aims

The temperature at which microcapsules containing a volatile liquid PFC undergo a phase change was measured. The microcapsules produced in this study have low echogenicity below room temperature, and high echogenicity above 55°C. If heated quickly, the echogenicity of the microcapsules is linear with temperature over 44 to 55°C. A sharp change in echogenicity at 45°C or 52°C would be preferable for monitoring thermal ablation near the spine. The microcapsule formulations considered should be modified for sharper transitions over no more than a few degrees, so that they may be used to monitor thermal ablation of tumors in the vicinity of the spine.

The microcapsules do not appear to be stable over time at either room or physiological temperatures. When slowly heated, a significant proportion of the microcapsules containing

PFCs with boiling points of 45 and 54°C underwent vaporization at 20-30°C, well below their intended transition temperatures. The microcapsules developed herein should be altered for stability at physiological temperatures in order to be used as contrast agents for monitoring thermal therapy. Microcapsules containing a PFC with a higher boiling point, such as 1H-perfluorohexane (boiling point = 70°C) may possibly have greater stability.

Once the microcapsules are stable at physiological temperatures, they could have applications in monitoring hyperthermia, which has target temperatures of 40-45°C. The appearance of the microcapsules at 44°C could indicate that target temperatures have been reached. Microcapsules with a 44-45°C threshold could also indicate the location of the hyperthermic rim around the coagulated target during ablation, a region in which a portion of the cells die [5, 233].

Increases in the vaporization temperature of the microcapsules over that of the bulk perfluorocarbon fluid due to the Laplace pressure were not observed. The microcapsules vaporized at or below the boiling points of the perfluorocarbons they contained. This was the case for microcapsules containing PFCs with boiling points of both 45 and 54°C.

The stability of the microcapsules when placed in high-intensity acoustic fields should be investigated. Acoustic droplet vaporization has the potential to lower the transition temperatures of the microcapsules. If used to monitor ultrasound ablation, the microcapsules should remain in the liquid state until the tissues reach the intended transition temperature. The peak rarefactional pressures in high-intensity ultrasound beams should not produce vaporization in the absence of the intended temperature increase. If the microcapsules do vaporize upon sonication, they could possibly be useful for determining the location of an acoustic beam. However, during ablation,

the microcapsules and microbubbles should be completely cleared from the tissues before sonication continues, to avoid reflection and scattering of the acoustic energy used for heating.

B.5 Conclusions

The microcapsules developed in this study transitioned from liquid to gas over an 11°C range and were not stable at room or physiological temperatures. They vaporized at or below the boiling points of the bulk perfluorocarbons of which they were composed, suggesting that the Laplace pressure within the microcapsules had little effect on their vaporization temperatures. As currently produced, these contrast agents are not applicable to monitoring ultrasound-based ablation of the spine, but they could possibly be reformulated with optimized production procedures for applications in hyperthermia or in thermal ablation.

B.6 Acknowledgements

I would like to thank Frank Szoka, Emily Perttu, the rest of Prof. Szoka's group, and Vasant Salgaonkar for their advice, guidance, and assistance in the development and production of phase-shift liposomes and microcapsules, and for the use of the Szoka group's facilities.

Publishing Agreement

It is the policy of the University to encourage the distribution of all theses, dissertations, and manuscripts. Copies of all UCSF theses, dissertations, and manuscripts will be routed to the library via the Graduate Division. The library will make all theses, dissertations, and manuscripts accessible to the public and will preserve these to the best of their abilities, in perpetuity.

Please sign the following statement:

I hereby grant permission to the Graduate Division of the University of California, San Francisco to release copies of my thesis, dissertation, or manuscript to the Campus Library to provide access and preservation, in whole or in part, in perpetuity.

Sara Scott
Author Signature

2-5-14
Date